Collinear laser spectroscopy of scandium and yttrium isotopes at IGISOL IV

Thesis submitted in accordance with the requirements of the University of Liverpool for the degree of Doctor of Philosophy

by

Liam James Vormawah

Oliver Lodge Laboratory

August 2017

Contents

List of Figures

List of Tables

Abstract

This thesis presents the results of two separate collinear laser spectroscopy investigations; one of proton-neutron pairing correlations in the odd-odd self-conjugate nucleus ^{42}Sc, and the other investigating the charge radii of neutron-rich Y isotopes and the sudden onset of nuclear deformation in the $Z \sim$40, $N \sim$60 region of the nuclear chart.

For the first time, the ^{42g,42m}Sc isomer shift, and corresponding change in mean-square charge radius, has been studied via collinear laser spectroscopy at IGISOL IV. The result for the change in mean-square charge radius supports the qualitative prediction given by the intuitive picture of proton-neutron pairing, in which the nuclear charge radius should be greater for an $I = 0$, $T = 1$ nuclear state than an $I \neq 0$, $T = 0$ state. This result is also, qualitatively speaking at least, in agreement with the results of previous proton-neutron pairing studies, namely studies of the charge radii of ^{38g,38m}K and ^{50g,50m}Mn. In addition to this, new values of the atomic factors for the mass and field shift, F and M, have allowed for a recalibration of the Sc charge radii measured previously on the same atomic transition as used here.

Spectroscopy has been performed on radioactive Y^{2+} ions for the first time. The motivation for this was to recalibrate previously measured charge radii for $^{86-90,92-102}$Y and isomeric states in $^{87-90,93,96,98}$Y, which were measured on the 363.3nm $5s^2\ ^1S_0 \rightarrow 4d5p\ ^1P_1$ transition occurring in the Y^+ ion. The complexity of this transition hindered the ability to reliably calculate the atomic mass and field shift factors, which are necessary for extraction of nuclear charge radii.

Acknowledgments

Firstly, I would like to thank my supervisor, Dr. Bradley Cheal, for all his help and guidance throughout my PhD, and for all the very thorough feedback without which neither this thesis or the related conference talks would have gone down as well as they did! Massive thanks also have to go to my fellow PhD colleagues and the academic staff at Liverpool for their help and support over the last few years – and, of course, for the good times outside of work! I would particularly like to thank Dr. Helen Vaughan for offering to read through the thesis with interest, as well as offering me much professional advice and support during the course of my studies.

Massive thanks also have to go to my collaborators at the University of Manchester and the IGISOL group at the University of Jyväskylä. I would especially like to thank Dr. Paul Campbell and Sam Kelly for their help and support with getting to grips with life in the lab (amongst other things!) and Dr. Annika Voss for her help not just in the lab but for agreeing to proofread certain chapters of this thesis – the feedback has all been acted upon! And certainly not forgetting the rest of the collaboration, staff and students alike – Iain, Tommi, Mikael, Alex, Sarina and Markus – not just for your assistance in the lab but also for the introduction to some of the fine places to eat, drink and be merry in downtown Jyväskylä!

Finally, I would like to thank those closest to me – in particular my Mum and Dad for being there not just throughout the PhD but for the duration of my studies. I certainly wouldn't have made it to this stage without your support!

Chapter 1

Introduction

Collinear laser spectroscopy allows for model-independent studies of nuclear sizes, shapes, spins and electromagnetic moments by way of fast, high-resolution hyperfine structure and isotope shift measurements. This technique is highly advantageous when applied to a source of radioactive ion beams. Its inherently high resolution enables detection of very small splittings and perturbations in the atomic energy levels arising from the nuclear structure. The limiting factor is the production and "on-line" transportation and study of the radioisotopes of interest, as their typically short lifetimes (and, to a lesser extent, the chemistry of the element) need to be taken into account. This introductory chapter summarises the history of this field of study, as well as introducing the work presented in this thesis and outlining the motivation for this work.

1.1 A brief history of the field

The fields of atomic physics and nuclear physics have a significantly interlinked history. Understanding of atomic structure developed over the course of the late 19^{th} and early 20^{th} century, and was crucial in the formulation of the framework of quantum mechanics. Spearheaded by the discoveries of radioactivity by Henri Becquerel in 1896 and the electron by J.J. Thomson the following year, a major turning point in our understanding of atomic structure came with Rutherford's landmark 1911 scattering experiment in which the atomic nucleus was discovered – the field of nuclear physics was born. Then came Niels Bohr's model of the atom two years later – the first atomic model to build upon Max Planck's theory of energy quantisation – thus accounting

for the discrete energy levels in which electrons can exist in an atom. Although the Bohr model has been superseded by other, more advanced models, the quantum theory underpinning it still holds well to this day. Transitions between energy levels were found to explain the atomic spectral lines which had first been observed in the 1890's by Albert A. Michelson [1].

These energy levels were soon found to have their own internal structure to them. Pieter Zeeman and Johannes Stark observed splitting of energy levels in magnetic and electric fields, respectively, whilst hyperfine structure had been known since its first observation by Michelson in the late 19^{th} century. The explanation for the existence of hyperfine structure came from Wolfgang Pauli in the 1920's – after Rutherford and Bohr had laid the foundations for the understanding of the nuclear atom – as being due to the interactions between the nucleus and the electrons orbiting it.

It was known from the outset that the nucleus had a finite size and mass. However, understanding of other nuclear properties was often found to be much less straightforward – particularly with regards to shape, magnetism and interactions between nucleons. A major turning point in our understanding of such properties came about with the development of the nuclear shell model, in which protons and neutrons occupy shells in analogy to electrons in atoms. It was soon found that, again in analogy with electrons in atoms, certain magic numbers of protons and neutrons were found to exist in nuclei [2]; a nucleon shell containing such a number of proton or neutrons is said to be closed (full), and such nuclei are disproportionately more stable against decay and deformation than nuclei with neighbouring proton or neutron numbers.

The splitting of the spectral lines was found to be due to the magnetism of the nucleus – described quantitatively by the nuclear magnetic dipole moment, itself related to the intrinsic angular momentum (spin) of the nucleus. More specifically, the atomic spectral lines are split due to the interaction between the nuclear magnetic moment and the magnetic field produced by the surrounding electrons. Further shifting, or perturbation, of individual hyperfine components occurs due to the distribution of charge throughout the nuclear volume, the effective shape of which is given by the electric quadrupole moment.

Michelson studied hyperfine splittings using his interferential refractometer which soon became known as the *Michelson interferometer* [3]. Since Michelson's investigation, techniques used for measuring hyperfine splittings of atomic spectral lines have undergone significant developments. The first of such developments was the advent of the Fabry-Perot etalon, which is used as part of the laser setup in this work. Early post-Michelson hyperfine structure investigations were performed using either a Fabry-Perot etalon or a diffraction grating to analyse the spectrum from a hollow cathode lamp [4].

Of course these early, rather primitive methods of hyperfine structure analysis, had their drawbacks. One such issue was their poor resolution, occurring due to thermal broadening of the spectral lines. These early hyperfine measurement techniques were also limited to stable or long-lived isotopes, which had to be transported by hand.

However, the 1960's saw these problems overcome with the invention of the laser and the subsequent advent of laser spectroscopic techniques. Further improvements arose in the early 1970's with the invention of the continuous-wave (CW) dye laser, allowing vastly improved resolution by means of tuning to virtually any transition frequency lying within the visible light range. Furthermore, the introduction of radioactive ion beam facilities allowed further expansion of the range of isotopes available for such studies, as production, transportation and spectroscopy of radioactive ions could now be done all within a fraction of a second, allowing for very short (sub-millisecond) half-lives.

The collinear laser spectroscopy technique is a more recent development that has been shown to reduce Doppler broadening within the ion beam, further improving the resolution of laser spectroscopic measurements. This technique, which forms the basis of the experimental methodology used in this work, will be explained in greater detail later in this thesis.

1.2 This work

Laser spectroscopic studies have been performed on radioactive isotopes of Sc and Y, produced via light-ion fusion-evaporation and proton-induced fission reactions respectively. Both investigations were made by means of online experiments performed at the IGISOL IV laboratory, located at the University of Jyväskylä, Finland, by a collaboration between the Universities of Liverpool, Manchester and Jyväskylä.

Information on the hyperfine structures and isotope shifts for the Sc and Y isotopes is presented in Chapters 5 and 6, respectively. The work on Sc focused specifically on the ground and isomeric states in the self-conjugate ($N = Z$) nucleus ^{42}Sc, investigating proton-neutron pairing correlations via a direct measurement of the ^{42g,42m}Sc isomer shift. This follows on from a previous study, analogous to this investigation, in which the ^{38g,38m}K isomer shift was measured. Being either side of the $N, Z = 20$ shell closures, these two odd-odd self-conjugate nuclei offer a powerful test of the spherical shell model, as they can be modelled as being an inert core of ^{40}Ca coupled to either a valence proton hole and neutron hole (^{38}K), or a valence proton and neutron (^{42}Sc). In either case, the measured isomer shift should point to a greater nuclear charge radius for a state with $I = 0$ than for such with $I \geq 0$, due to the effects of orbital blocking. Preliminary shell model calculations have been performed for the ^{42g,42m}Sc isomer shift for comparison with the experimental value.

The work on Y is the first attempt at optical spectroscopy of doubly charged radioactive Y ions. This work aims to recalibrate previously measured charge radii of neutron-rich Y isotopes and isomers [5] which lacked a reliable calibration due to the complexity of the atomic transition studied (leading to difficulty in reliable calculation of the atomic factors for the mass and field shifts). A simpler transition could not be found in the singly charged Y ion but one such example was found in the doubly charged ion. However, the fraction of reaction products emerging from the IGISOL in a doubly charged state only accounts for one tenth of the total yield, thus placing constraints on which isotopes were suitable for measurement (i.e. those near the peak of production were by far the best candidates).

Key theoretical considerations for the work presented is given in Chapter 2 and an overview of the experimental technique in Chapter 3. Chapter 4 describes the experimental setup at the IGISOL IV laboratory in detail. Chapters 5 and 6 report the results and current status of the respective Sc and Y studies, and Chapter 7 summarises the work presented and outlines the future outlook for both investigations.

Chapter 2

Theory

From the law of conservation of energy, for an electron orbiting the nucleus in an atom to gain or lose energy, energy must either be absorbed by or emitted from the atom. If there were a continuum of possible orbits, electromagnetic radiation would be continuously emitted from the atom and the electron would spiral inwards, eventually colliding with the nucleus. It is well known, of course, that this is not what happens within an atom! Instead, when an electron makes a transition between from one energy level to another, energy is absorbed or emitted in the form of a packet of electromagnetic radiation, or **photon**. The energy of this photon is equal to the energy difference between the two levels involved in the transition. This is what gives rise to the atomic spectral lines – the unique "signature" or "fingerprint" of a particular element (or isotope thereof).

Electrons are the lightest of the three main constituents of the atom (much lighter than the proton and neutron), and are sources of electromagnetic fields responsible for some inter-atomic interactions due to their negative charge. Electrons are also fermions, and therefore obey **Fermi-Dirac statistics** and the **Pauli exclusion principle**; no two electrons can occupy the same quantum state. There are two distinct components to an electron's total angular momentum – these are the **orbital** angular momentum, l, and the **spin**, s ($= \frac{1}{2}$). Electrons in atoms arrange themselves into discrete energy levels or "electron shells", according to the *principal quantum number*, n. Each shell is then further divided into "subshells" according to their *orbital quantum number*, l, in order to satisfy the Pauli exclusion principle. The first subshell, s ($s$harp) corresponds to $l = 0$,

l	Subshell	Maximum number of electrons
0	s	2
1	p	6
2	d	10
3	f	14
4	g	18
5	h	22
6	j	26

Table 2.1: In an atom, each electron shell is split into subshells according to orbital quantum number l. The first four are named s (**s**harp), p (**p**rincipal), d (**d**iffuse), f (**f**undamental), with subsequent subshells then going in alphabetical order (omitting the letter i).

the next, p ($p$rincipal) corresponds to $l = 1$, d ($d$iffuse) to $l = 2$, f ($f$undamental) to $l = 3$ etc., with subsequent ($l = 4, 5, 6, ...$) then labelled in alphabetical order omitting the letter "i". Table 2.1 shows which subshell corresponds to which value of l, and how many electrons each can hold – each subshell can hold $2(2l + 1)$ electrons, due to the orbital magnetic quantum number m_l and spin magnetic quantum number m_s ($= \pm\frac{1}{2}$). From m_s, it can be seen that electrons in an energy level can form pairs – one electron in a pair will have $m_s = \frac{1}{2}$, whilst the other will have $m_s = -\frac{1}{2}$, again so as to satisfy the Pauli exclusion principle.

2.1 Hyperfine structure and nuclear moments

The spin and orbital angular momenta of an electron have associated magnetic moments, μ_l, given by [6]

$$\vec{\mu}_l = -g_l \frac{e}{2m_0} \vec{l}, \tag{2.1}$$

and μ_s, given by [6]

$$\vec{\mu}_s = -g_s \frac{e}{2m_0} \vec{s}, \tag{2.2}$$

where g_l and g_s are the respective orbital and spin gyromagnetic ratios, also referred to as (Landé) g-factors. These are simply the ratios of μ_l and μ_s to l and s respectively.

It is, specifically, these magnetic moments and how they interact with each other which give rise to the **spin-orbit interaction**. The spin and orbital angular momenta couple together, giving an electron its *total angular momentum*, j. This occurs since the magnetic moment of the electron interacts with the magnetic field that it creates as a charged particle.

As a result of the coupling of spin and orbital angular momenta, the degeneracy of the level is lifted by means of the level being split in two; this is known as **fine structure**. There are two mechanisms by which spin and orbital angular momenta can couple to give the total electronic angular momentum, J. These are known as jj-coupling and LS-coupling. In the jj-coupling scheme, the dominant component is the interaction between each electron's spin with its orbital angular momentum; thus, for the i^{th} electron,

$$\vec{j_i} = \vec{l_i} + \vec{s_i}; j_i = |l_i - s_i|, |l_i - s_i| + 1, ..., l_i + s_i - 1, ..., l_i + s_i, \tag{2.3}$$

and for an atom (or ion) with N electrons, J is given by

$$\vec{J} = \sum_{i=1}^{N} \vec{j_i}; \quad |\vec{J}| = \sqrt{J(J+1)}\hbar. \tag{2.4}$$

In the LS-coupling scheme – as its name suggests – J is obtained from the coupling of the **total** spin and orbital angular momenta of the system, with the spin-orbit interaction now merely a perturbation; thus, for an atom (or ion) with N electrons,

$$\vec{L} = \sum_{i=1}^{N} \vec{l_i}; \quad |\vec{L}| = \sqrt{L(L+1)}\hbar, \tag{2.5}$$

$$\vec{S} = \sum_{i=1}^{N} \vec{s_i}; \quad |\vec{S}| = \sqrt{S(S+1)}\hbar. \tag{2.6}$$

and J is now therefore

$$\vec{J} = \vec{L} + \vec{S}; J = |L - S|, |L - S| + 1, ..., L + S - 1, ..., L + S. \tag{2.7}$$

The energy shift in fine structure is given by

$$E_{S-O} = \beta_{LS}\langle \vec{S} \cdot \vec{L} \rangle. \tag{2.8}$$

In order to find this energy, we need to evaluate the expectation value of the operator $\vec{L}\cdot\vec{S} = \frac{1}{2}(\vec{J}\cdot\vec{J} - \vec{L}\cdot\vec{L} - \vec{S}\cdot\vec{S})$ for each term ${}^{2S+1}L$; in each term there are $(2S+1)(2L+1)$ states, all combinations of which will have the same electrostatic energy – i.e. the *degeneracy* is lifted for each level. This allows us to select suitable eigenstates in order to simplify the calculation of the magnetic spin-orbit interaction. Using the states $|LSJM_J\rangle$ (linear combinations of $|LM_LSM_S\rangle$), we obtain

$$E_{S-O} = \frac{\beta_{LS}}{2}(J(J+1) - L(L+1) - S(S+1)). \tag{2.9}$$

This gives the following energy difference between adjacent J-states:

$$\Delta E_{FS} = E_J - E_{J-1} = \beta_{LS} J. \tag{2.10}$$

Up to now, it has been assumed that the nucleus has no effect on the structure of the atomic energy levels except for its overall charge, whereas in actual fact the the magnetism of the nucleus and the distribution of the nuclear charge are jointly responsible for a small – but readily observed – contribution to the structure of the energy levels in an atom.

The effect of the nucleus on the overall atomic structure manifests itself in the splitting and perturbation of the fine structure J-states, giving rise to *hyperfine structure*. These phenomena occur due to the nuclear electromagnetic multipole moments. The splitting occurs due to the **magnetic dipole moment** of the nucleus, with the further perturbation of the split levels arising from the **electric quadrupole moment**.

2.1.1 Magnetic dipole moment

The dominant factor involved in hyperfine splitting is the interaction between the nuclear magnetic dipole moment $\vec{\mu}_I$ and the magnetic field produced by the electrons $\vec{B}_e$, with interaction energy given by

$$E = \vec{\mu}_I \cdot \vec{B}_e. \tag{2.11}$$

In analogy to the electronic magnetic moments, the nuclear magnetic dipole moment can be written in terms of the nuclear Landé g-factor, g_N as

$$\vec{\mu}_I = g_N \mu_N \vec{I}, \tag{2.12}$$

where $\mu_N = \frac{e\hbar}{2m_p}$ is the nuclear magneton.

The nuclear and electronic angular momenta couple to give the total hyperfine angular momentum, F – analogous to the coupling of the spin and orbital angular momenta of the electron:

$$\vec{F} = \vec{I} + \vec{J}; F = |I - J|, |I - J| + 1, ..., I + J - 1, I + J. \tag{2.13}$$

Such transitions must also obey the selection rules

$$\Delta F = 0, \pm 1, \tag{2.14}$$

$$F = 0 \nrightarrow F = 0. \tag{2.15}$$

Thus, for each consecutive atomic transition, upper and lower F-states can either be the same, or differ by 1, but cannot be the same if $F = 0$.

The coupling of I and J gives the following formulation of the hyperfine Hamiltonian,

$$H_{hfs} = A\vec{I} \cdot \vec{J}, \tag{2.16}$$

where the scalar product of the nuclear and electronic spins can be written as

$$\vec{I} \cdot \vec{J} = \frac{A}{2}(F(F+1) - I(I+1) - J(J+1)). \tag{2.17}$$

The energy shift due to the dipole interaction is given by

$$\Delta E = \alpha A. \tag{2.18}$$

The parameter A in equation (2.18) is the **hyperfine dipole parameter**, whose definition is given by

$$A = \frac{\mu_I B_e(0)}{IJ}, \tag{2.19}$$

where $B_e(0)$ is the magnetic field produced by the electrons at the site of the nucleus. The variable α is a function of the angular momentum, defined as

$$\alpha = \frac{K}{2}. \tag{2.20}$$

where K is a new quantum number, given by

$$K = F(F+1) - I(I+1) - J(J+1). \tag{2.21}$$

From equation (2.19), it can be inferred that the nuclear magnetic moments can be calibrated using a reference isotope whose moments have previously been determined, yielding [7]

$$\frac{\mu}{\mu_{\text{ref}}} = \frac{IA}{I_{\text{ref}} A_{\text{ref}}}. \tag{2.22}$$

Empirical estimates of the nuclear magnetic moment, known as **Schmidt estimates**, can be calculated for comparison with experimentally determined values [8], and for odd-odd nuclei such estimates can be calculated using

$$\mu(I) = \frac{I}{2}\left[\frac{\mu_\pi}{j_\pi} + \frac{\mu_\nu}{j_\nu} + \left(\frac{\mu_\pi}{j_\pi} - \frac{\mu_\nu}{j_\nu}\right)\frac{j_\pi(j_\pi+1) - j_\nu(j_\nu+1)}{I(I+1)}\right], \tag{2.23}$$

where j_π and j_ν are the respective total angular momenta of the unpaired proton and neutron, and μ_π and μ_ν their respective magnetic moments.

2.1.2 Electric quadrupole moment

The nuclear electric quadrupole moment, Q, describes the effective ellipsoidal shape of the distribution of charge throughout the nuclear volume. A non-zero quadrupole moment is indicative of a charge distribution which is not spherically symmetric. Figure 2.1 shows a typical quadrupole arrangement of charges. This arrangement will not experience a net force or torque when placed in a uniform external field, but will

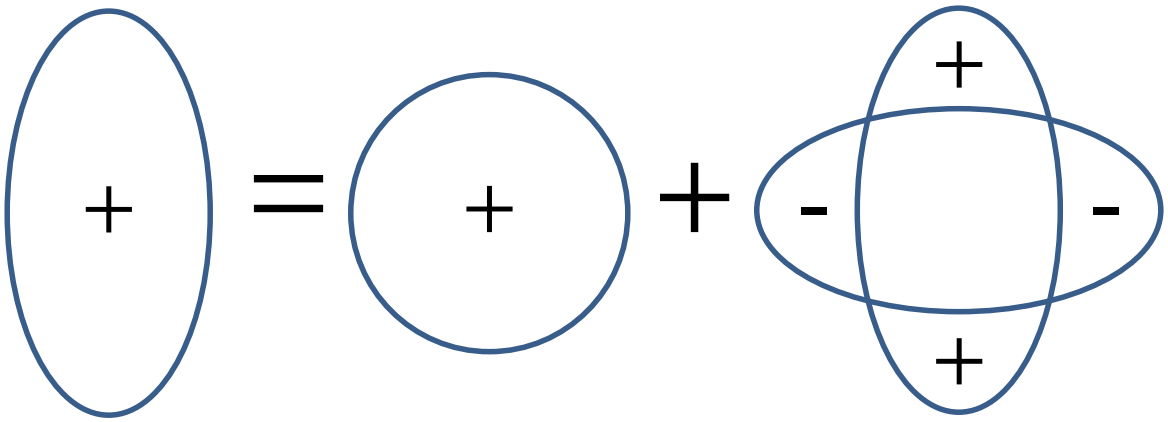

Figure 2.1: Schematic showing how a prolate nuclear shape (as an example) is obtained from the deviation from sphericity of the charge distribution.

experience a force if the field is non-uniform. A quadrupole moment for such an arrangement of charges is classically defined as [9]

$$Q_0 = \int \rho(3z^2 - r^2)\mathrm{d}V, \tag{2.24}$$

where ρ is the charge density within a volume element $\mathrm{d}V$, r the radius and z the distance along the symmetry axis for the volume, V, in which the charges are contained.

By convention, the quadrupole moment is positive if the nucleus has a prolate (rugby ball) shape – i.e. the charge distribution is elongated along the symmetry axis – and negative for if it has an oblate (disc) shape – i.e. if the charge distribution is flattened along the symmetry axis. How the nuclear shape changes with quadrupole deformation parameter $\langle\beta_2\rangle$ is illustrated in Figure 2.2.

As stated previously, Q is responsible for the perturbation of the hyperfine F-states resulting from the magnetic dipole interaction. In analogy to the magnetic dipole contribution to the splitting, this perturbation is given by

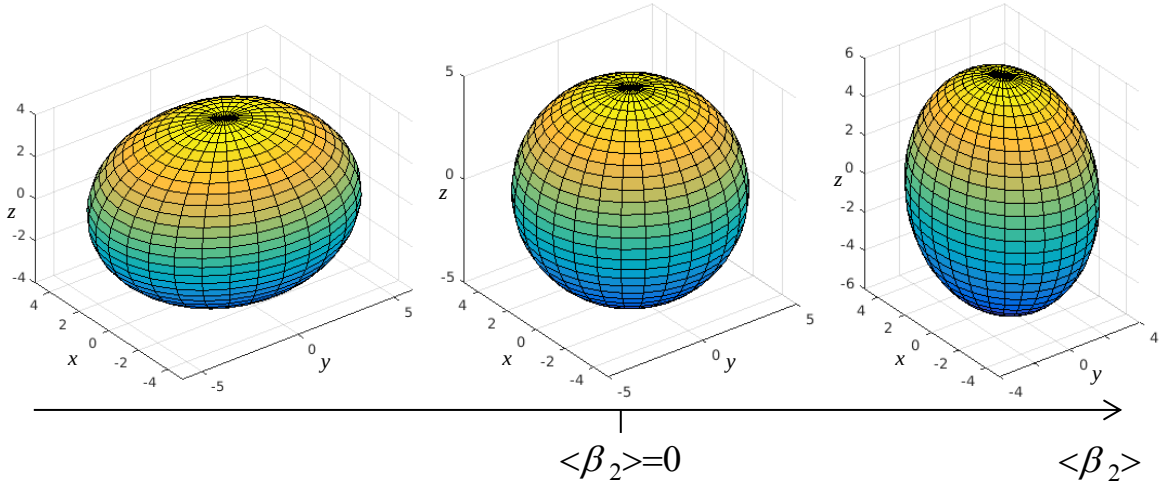

Figure 2.2: The effective shapes taken by charge distributions of nuclei with intrinsic electric quadrupole moments $Q_0 < 0$ (left), $Q_0 = 0$ (centre) and $Q_0 > 0$ (right).

$$\Delta E = \beta B, \tag{2.25}$$

where β is a function of the angular momentum (analogous to α in the dipole component of the total splitting), defined as

$$\beta = \frac{3K(K+1) - 4I(I+1)J(J+1)}{8I(2I-1)J(2J-1)}, \tag{2.26}$$

and B is the hyperfine quadrupole parameter, and is defined as

$$B = eQ_{\mathrm{s}}\left\langle \frac{\partial^2 V_e}{\partial z^2} \right\rangle, \tag{2.27}$$

where $\left\langle \frac{\partial^2 V_e}{\partial z^2} \right\rangle$ is the expectation value of the electric field gradient produced by the electrons, and Q_{s} is the *spectroscopic* (measured) electric quadrupole moment. As is the case for the magnetic dipole moment, the electric quadrupole moment of an isotope (or isomer) can be calibrated using a reference isotope whose quadrupole moment is known, yielding equation (2.28) [7]

$$\frac{B}{B_{\mathrm{ref}}} = \frac{Q_{\mathrm{s}}}{Q_{\mathrm{s(ref)}}}. \tag{2.28}$$

It should be noted that Q_{s} is not the same as the intrinsic (actual) quadrupole moment, Q_0. Whilst Q_{s} is measured with respect to the laboratory axis, Q_0 is calculated

with respect to the axis of nuclear symmetry. However, Q_0 can be obtained from Q_s by means of the strong-coupling projection formula

$$Q_\mathrm{s} = Q_0 \frac{3\Omega^2 - I(I+1)}{(I+1)(2I+3)}, \tag{2.29}$$

where Ω is the projection of I along the axis of symmetry.

There are limitations on which nuclear states Q_s can be measured. Optical measurements are only sensitive to the quadrupole interaction if $I \geq 1$ and $J \geq 1$. For any nuclear state which does not satisfy this condition, there are no hyperfine B parameters to deal with and therefore the hyperfine formula is simplified to solely the dipole term. Furthermore, no splitting of the level occurs if $I = 0$ or $J = 0$.

2.1.3 Total hyperfine structure

It can be seen from the above that the total hyperfine energy shift is given by

$$\frac{\Delta E}{\hbar} = \frac{K}{2}A + \frac{3K(K+1) - 4I(I+1)J(J+1)}{8I(2I-1)J(2J-1)}B. \tag{2.30}$$

To account for the splitting of the hyperfine peaks in an optical spectrum (showing a transition between two states), the peak position in terms of frequency, γ, is given by the formula

$$\gamma = \nu + \alpha_\mathrm{u}A_\mathrm{u} - \alpha_\mathrm{l}A_\mathrm{l} + \beta_\mathrm{u}B_\mathrm{u} - \beta_\mathrm{l}B_\mathrm{l}, \tag{2.31}$$

where ν is the *centroid* of the hyperfine structure, $A_\mathrm{l}, A_\mathrm{u}$ are the respective hyperfine dipole parameters for the lower and upper J-states, $B_\mathrm{l}, B_\mathrm{u}$ the respective quadrupole parameters for the same two J-states and $\alpha_\mathrm{l}, \alpha_\mathrm{u}, \beta_\mathrm{l}, \beta_\mathrm{u}$ the corresponding functions of the angular momenta for the same two states (as defined earlier). All parameters can be obtained by means of a χ^2-minimisation process (to be discussed in more detail later).

It is not the absolute position of the hyperfine peaks which is important, but the positions of the peaks relative to the centroid of the structure. The spectra for all isotopes are translated by the same arbitrary value corresponding to the approximate

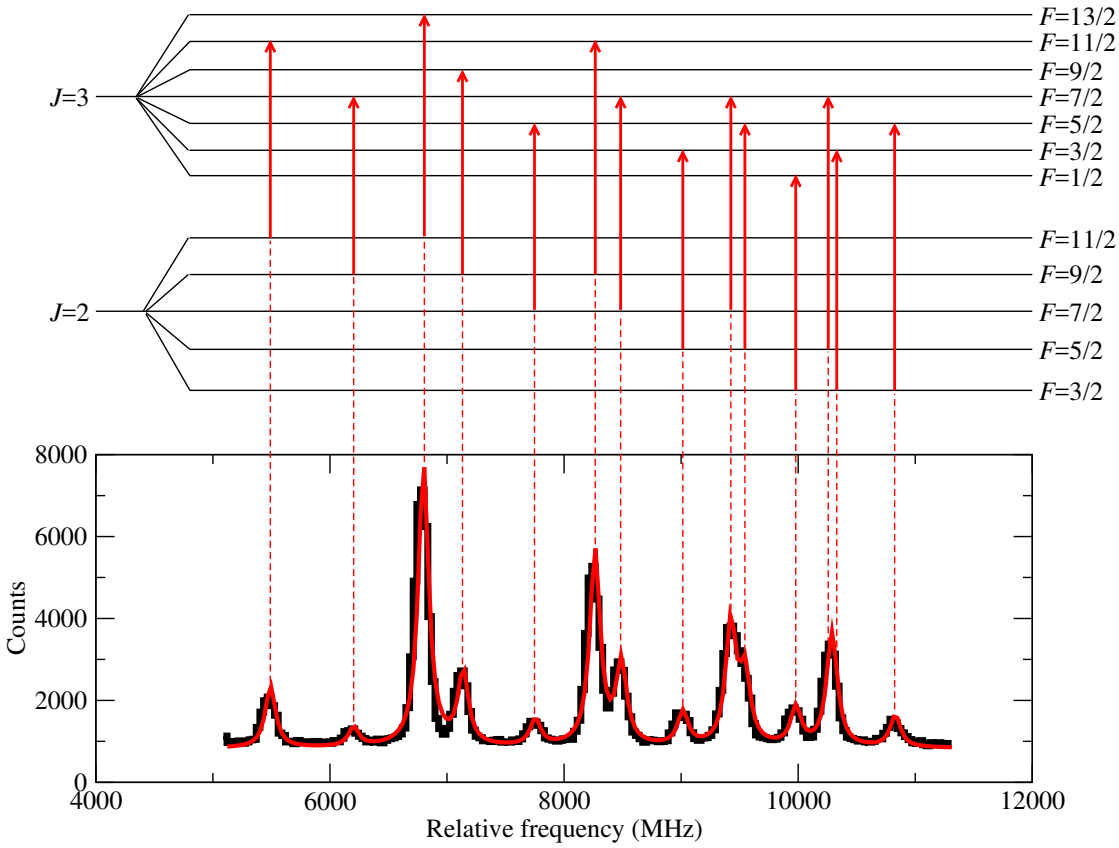

Figure 2.3: Optical spectrum of the ^{45}Sc ground state ($I = \frac{7}{2}$) and corresponding level scheme, showing how each peak corresponds to a transition between hyperfine components of the lower and upper J-states involved in a selected atomic transition.

absolute transition frequency – this allows frequency axes to be quoted in convenient units of MHz. Figure 2.3 illustrates how each peak in an optical spectrum corresponds to a transition between hyperfine components of the lower and upper J-states.

2.1.4 Alternative methods of measuring nuclear moments

Other methods (aside from hyperfine structure analysis) can be used in order to find nuclear moments for the aforementioned reference isotopes which one would use to calibrate the moments for radioactive species studied using optical spectroscopic methods. Generally, however, such methods have been found either to be limited to stable or long-lived isotopes, or to be model-dependent – unlike optical spectroscopy. Determin-

ing the nuclear moments of the isotopes studied as part of this work would therefore have been problematic using the methods explained in the following sections.

Magnetic moments by molecular beam resonance

Rabi *et al.* [10] demonstrated that for any system with a non-zero angular momentum and magnetic moment, in a region of external magnetic field the angular momentum will precess with a frequency equal to the Larmor frequency. Thus, for a nucleus with spin I and magnetic dipole moment μ_I in a region of magnetic field B, the precession frequency is given by

$$\nu_{\text{precession}} = \frac{\mu_I B}{Ih}. \tag{2.32}$$

Using this method, it is possible to determine both the magnitude and sign of μ_I, as the direction of precession is dependent upon whether μ_I is parallel or antiparallel to I.

Although largely superseded by more sophisticated methods of measuring the nuclear magnetic moment (most notably the optical techniques employed as part of this work), the work of Rabi *et al.* paved the way for the development of **nuclear magnetic resonance**. NMR has since become widely established as a field of research, with two main uses in medical imaging (MRI scans) [11] and materials analysis (NMR spectroscopy) [12].

Decay spectroscopy

Information on the nuclear shape (electric quadrupole moment) can be obtained from decay (alpha, beta or gamma) spectroscopic data [13]. The nature of deformation (rotational, vibrational etc.) has a significant influence on the type of decay a radionuclide will undergo, and the characteristic energy spectrum which will be generated for it. Information from decay spectra can be used to assign transitions and levels (based on configurations from nuclear models), and therefore develop level schemes, for a wide range of nuclides.

Decay spectroscopy has also been successfully combined with collinear laser spectroscopy in more recent studies. In such studies employing both techniques simulta-

neously, energy spectra of either the isotopes of interest or, in many instances, their decay products, are obtained in addition to the hyperfine spectra. This is advantageous in such cases as characterising excited states in nuclei and confirming nuclear spins. This includes a study performed at IGISOL by Moore *et al.* [14], investigating the properties of the 8^- isomer in ^{130}Ba, in which a germanium detector was mounted just after the cooler, and both forms of spectroscopy (decay and laser) were performed in-flight. A more advanced version of the combined laser/decay spectroscopy technique has been employed in the investigation of neutron-deficient francium performed at ISOLDE-CERN by Lynch *et al.* [15], in which Fr ions, once tuned onto resonance, were deflected from the CRIS (**C**ollinear **R**esonance **I**onisation **S**pectroscopy) beamline [16] to a dedicated decay spectroscopy station [17].

Coulomb excitation

The Coulomb excitation (or Coulex for short) [18] method offers a particularly precise probe of the electric quadrupole moment. Excitation takes place by means of a stable ion beam – of energy much less than the Coulomb barrier – impinging upon a (usually) stable target [19]. The target nucleus goes from the ground state, $|1\rangle$, to an excited state, $|2\rangle$, via the Coulomb interaction. The nuclear interaction is negligible, and the excitation therefore taken to be purely electromagnetic – provided the safe energy criterion of nuclear surfaces (projectile and target) being more than 5fm apart is met. The nucleus subsequently decays, emitting either a gamma ray or an internal conversion electron in the process. Excitation probabilities, and therefore gamma ray intensities, are related to the electric quadrupole (E2) transition matrix elements $\langle 2||M(E2)||1\rangle$; thus, the $B(E2)$ values can be deduced from $\langle 2||M(E2)||1\rangle^2 \approx B(E2; |2\rangle \rightarrow |1\rangle)$, and the intrinsic quadrupole moment from $\langle 2||M(E2)||2\rangle \approx Q_0$.

2.2 Isotope shift and charge radii

The isotope shift arises from the change in frequency of an atomic transition, or that of the centroid of the hyperfine structure, between isotopes of an element; such changes occur due to differences in mass, shape and size between isotopes [20]. Isotope shifts are a useful tool for extracting the changes in nuclear mean-square charge radius. Figure 2.4 illustrates the how an isotope shift is extracted from hyperfine spectra. There are

two main components to an isotope shift; these are are the *mass shift*, $\delta\nu_{\mathrm{MS}}^{AA'}$, and the field shift, $\delta\nu_{\mathrm{FS}}^{AA'}$. Thus, the total isotope shift can be written, to a good approximation, as

$$\delta\nu^{AA'} = \delta\nu_{\mathrm{MS}}^{AA'} + \delta\nu_{FS}^{AA'}. \tag{2.33}$$

There are two further components to an isotope shift; *level isotope shift* – the difference in energy of the same electron orbital between two isotopes – and the *transition isotope shift* – the difference in level shifts for the upper and lower electron orbitals [21]. However, due to the inability to directly observe the level shift in experiments, neither of these are of experimental interest.

It is the field shift from which the change in nuclear mean-square charge radius, $\delta\langle\ r^2\ \rangle^{A,A'}$, is extracted. The change in nuclear mean-square charge radius is a nuclear parameter sensitive to both nuclear size and shape. In other words, in addition to information relating to nuclear size, a measurement of $\delta\langle\ r^2\ \rangle^{A,A'}$ will also yield information on nuclear deformation complementary to the electric quadrupole moment. The relationship between the change in mean-square charge radius between two isotopes A and A', and the corresponding isotope shift, can be shown more clearly by rewriting equation (2.33) as

$$\delta\nu^{A,A'} = M\frac{A'-A}{AA'} + F\delta\langle r^2\rangle^{AA'}, \tag{2.34}$$

where $M\frac{A'-A}{AA'}$ is the mass shift, and $F\delta\langle r^2\rangle^{AA'}$ is the field shift. In equation (2.34), the variables M and F are the respective atomic factors for the mass shift and field shift. Thus it can be seen from equation (2.34) that these atomic factors need to be correctly determined if any meaningful values are to be obtained for nuclear charge radii.

2.2.1 Mass shift

The mass shift arises due to the nucleus having a finite mass, and accounts for the recoil motion of the nucleus. Two isotopes will have different recoil energies due to their differing masses; the resulting change in the kinetic energy of the atom causes shifts in the electronic energy levels. The internal kinetic energy of the atom can be written as [22]

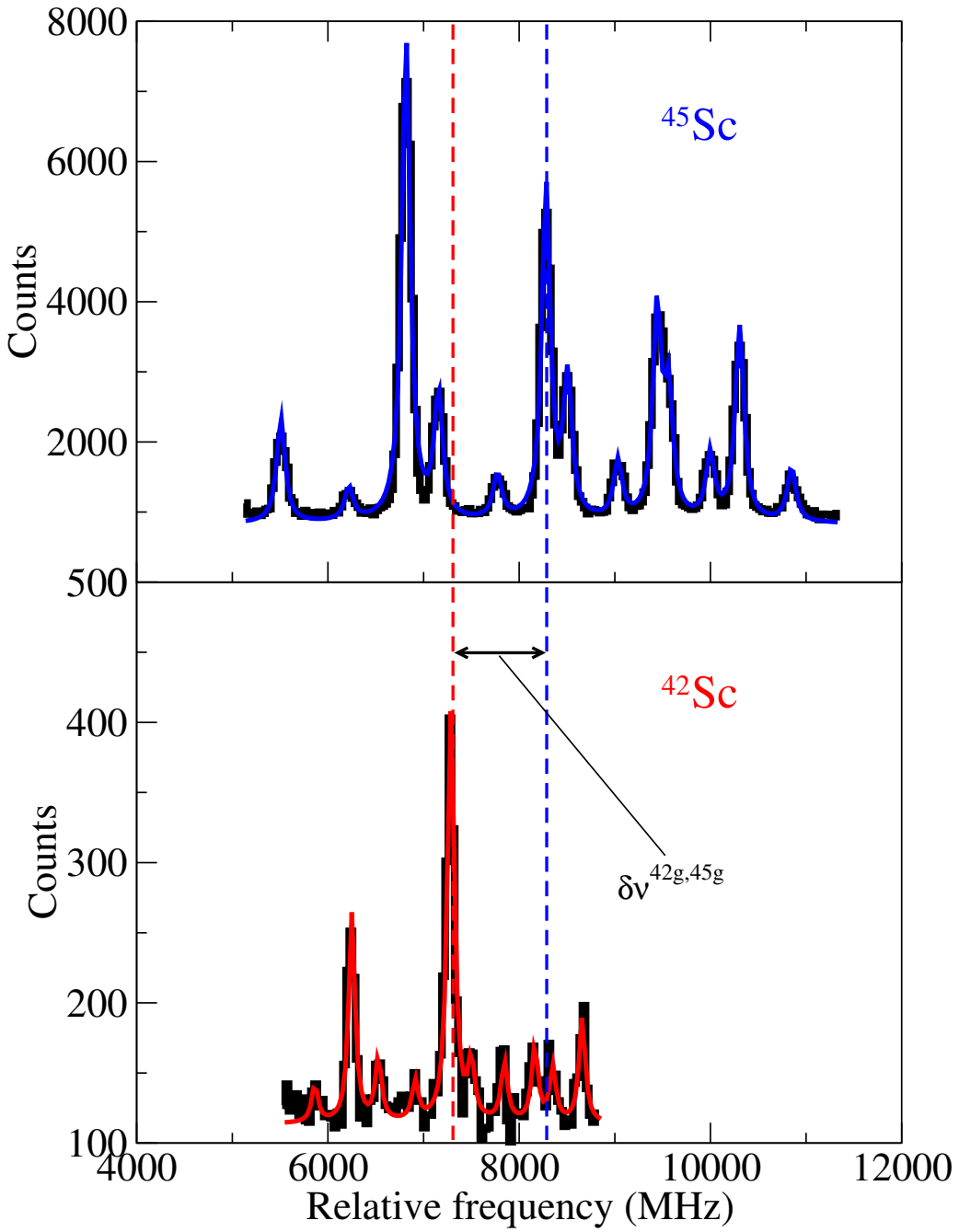

Figure 2.4: Optical spectra of scandium isotopes ^{42}Sc and ^{45}Sc, showing clearly the centroid of each structure (given by the colour-coded dashed lines) and the ^{45g,42g}Sc isotope shift.

$$T = \frac{\vec{p}_N^{\,2}}{2m_N} + \sum_i \frac{\vec{p}_i^{\,2}}{2m_e}, \tag{2.35}$$

where m_N and m_e are the respective masses of the nucleus and the electron, $\vec{p}_N$ is the momentum of the nucleus, and $\vec{p}_i$ is the momentum of the i^{th} electron. As the atom is taken to be stationary, applying conservation of momentum yields

$$\vec{p}_N = -\sum_i \vec{p}_i. \tag{2.36}$$

Substituting equation (2.36) into equation (2.35) gives the following formulation of the kinetic energy Hamiltonian *for a given energy level* [4]

$$T = \frac{m_N + m_e}{2m_N m_e} \sum_i \vec{p}_i^{\,2} + \frac{1}{m_N} \sum_{i>j} \vec{p}_i \cdot \vec{p}_j. \tag{2.37}$$

As can be seen from equations (2.35) and (2.37), this formulation of the Hamiltonian leads to there being two distinct contributions to the mass shift; the *normal mass shift* arises from the first term, and the *specific mass shift* arises from the second. The shift in electronic energy levels is inversely proportional to the nuclear mass – thus, the transition frequency is proportional to $\frac{1}{m_N}$, and the difference in frequency due to the total mass shift of the same transition for two different nuclear masses, m_N and $m_N{}'$, is therefore proportional to $\frac{m_N' - m_N}{m_N m_N'}$. It can be deduced from this that, for an isotope shift involving two isotopes A and A', both normal and specific mass shift terms share a common mass dependence given by the factor $\frac{A'-A}{AA'}$ [4].

The normal mass shift, $\delta\nu_{\text{NMS}}^{AA'}$, given by the first term in equation (2.37), is the mass shift for a system consisting of the nucleus plus one electron. This system has a *reduced mass*, μ [23], given by equation (2.38)

$$\mu = \frac{m_e m_N}{m_N + m_e}. \tag{2.38}$$

The presence of the electron gives the system a centre of mass somewhere within the nuclear region but away from the centre of the nucleus, as shown schematically in Figure 2.5, and the direction of the electron momentum does not need to be taken into account in this case.

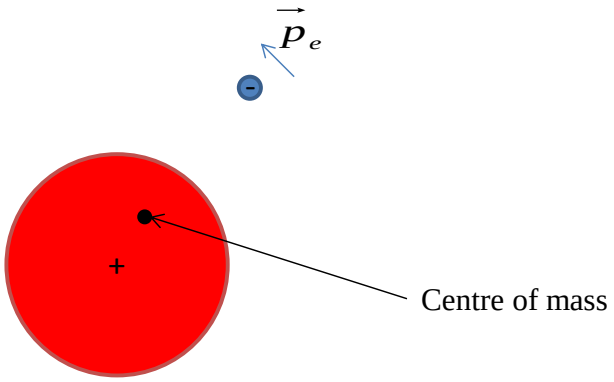

Figure 2.5: Schematic showing the position of the centre of mass for an atom comprising the nucleus plus one electron. Not to scale.

The normal mass shift can be written as

$$\delta\nu_{\mathrm{NMS}}^{AA'} = N\frac{A' - A}{AA'}, \tag{2.39}$$

where A and A' are the *accurate atomic masses* of the isotopes in question, and the atomic factor N is equal to $\frac{m_e\nu_0}{m_n}$, where m_n is the nucleon mass and ν_0 is the equivalent transition frequency for an atom of the same element with an infinitely heavy nucleus.

The specific mass shift, $\delta\nu_{\mathrm{SMS}}^{AA'}$, can be considered a correction to the normal mass shift for cases where there are two or more electrons present, where spatial correlations between electrons need to be taken into account [23], as these have an influence on the centre of mass of the whole system. For a system with two electrons, the specific mass shift depends on the spatial correlation of the electrons, and intuitively will be positive if the electrons are travelling on the same side of the nucleus, and negative if they are travelling on opposite sides of it. It goes without saying that this has an effect on the centre of mass of the system. Figure 2.6 illustrates the different scenarios for two electrons; in the case of two electrons with momenta in the same direction, the centre of mass is shifted towards the electrons, whilst for the case of electrons with momenta in opposite directions, the centre of mass is shifted towards the centre of the nucleus.

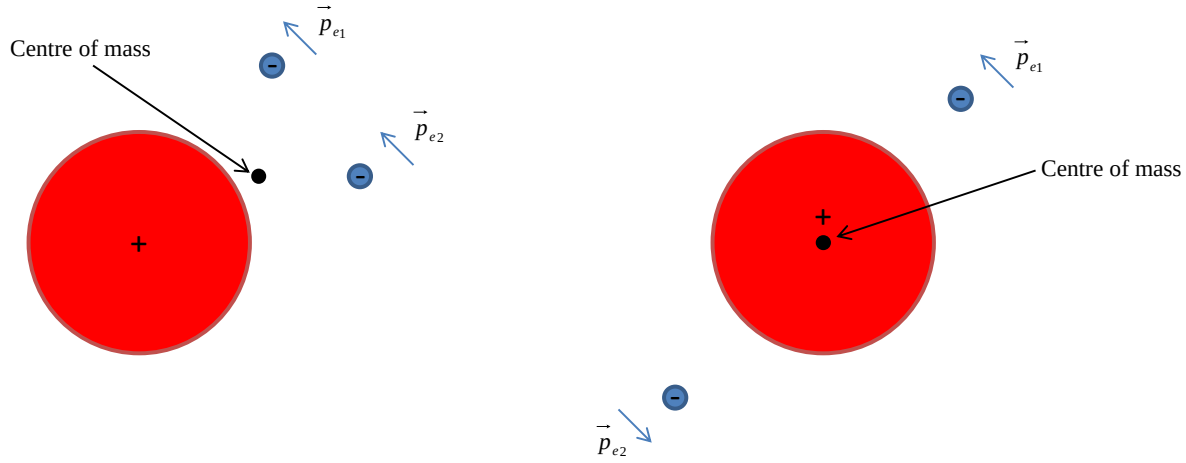

Figure 2.6: Schematic illustrating how the relative motion of the electrons (to each other) affects the position of the centre of mass of the atom, leading to the specific mass shift. Not to scale.

The specific mass shift can be written as

$$\delta\nu_{\mathrm{SMS}}^{AA'} = S\frac{A' - A}{AA'}, \tag{2.40}$$

where S is an atomic factor whose complex computation involves intricate knowledge of electron wavefunctions. There are however, empirical calculations for the specific mass shift in terms of the normal mass shift [4, 24]; one for $ns \rightarrow np$ transitions

$$\delta\nu_{\mathrm{SMS}}^{AA'} = (0.3 \pm 0.9)\delta\nu_{\mathrm{NMS}}^{AA'}, \tag{2.41}$$

and another applying in the case of $ns^2 \rightarrow nsnp$ transitions

$$\delta\nu_{\mathrm{SMS}}^{AA'} = (0.0 \pm 0.5)\delta\nu_{\mathrm{NMS}}^{AA'}. \tag{2.42}$$

Substituting 2.39 and 2.40 into the mass shift term in 2.33 gives

$$\delta\nu_{\mathrm{MS}}^{AA'} = (N + S)\frac{A' - A}{AA'}, \tag{2.43}$$

meaning $\delta\nu^{AA'}$ can now be expressed as

$$\delta\nu_{\mathrm{MS}}^{AA'} = M\frac{A'-A}{AA'}, \tag{2.44}$$

where $M = N + S$ is the atomic factor for the total mass shift.

It should be noted that the mass shift does not actually offer any nuclear information of interest. However, as it is the *total* isotope shift that is obtained from optical spectra, $\delta\nu_{\mathrm{MS}}^{AA'}$ still needs to be accounted for in order to extract the charge radius measurements from the field shift.

2.2.2 Field shift

The field shift occurs due to the effect of the finite nuclear size on the electrostatic potential experienced by the electrons. For an infinitesimally small point nucleus, this would be a pure Coulomb potential. However, a real nucleus has a finite size and a charge distribution and such quantities will therefore vary for different isotopes. For electrons whose orbits do not overlap with the nuclear volume, the difference between isotopes has no effect, as the nucleus appears point-like to such electrons. However, for electrons in the inner subshells (particularly the s and p subshells), which have a non-zero probability of appearing *within* the nuclear volume, the difference in isotopes will have an influence on the potential these electrons experience. This will in turn alter the electronic energy levels; level energies increase as the radial distribution of nuclear charge increases [25]. So, the potential for a point nucleus, $V_0(r)$ would be given by

$$V_0(r) = -\frac{Ze^2}{4\pi\epsilon_0 r}, \tag{2.45}$$

whilst that for a sphere of uniform charge density and radius r_0 is given by

$$V(r) = \frac{Ze^2}{4\pi\epsilon_0 r_0}\left(-\frac{3}{2} + \frac{1}{2}\frac{r^2}{r_0^2}\right), \tag{2.46}$$

for $r < r_0$.

Plotting the curves of 2.45 and 2.46 as a function of radial distance r both for a point nucleus and for finite nuclei of different sizes shows how the potential tails off at

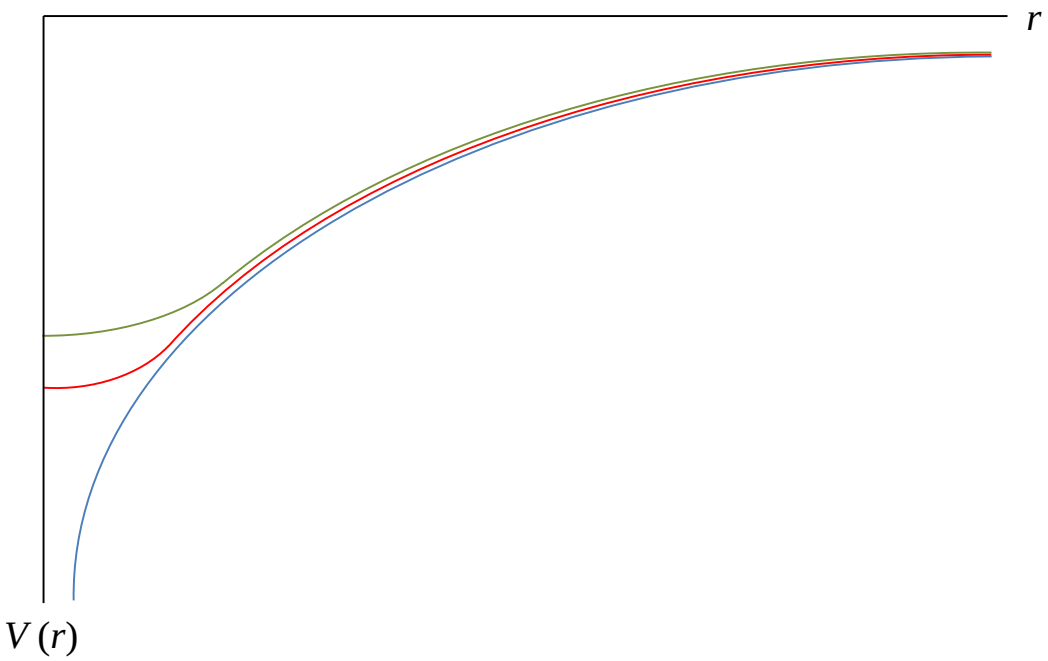

Figure 2.7: Plot of potential $V(r)$ felt by an atomic electron due to the nucleus, against distance r for a point nucleus (blue curve) and for two real nuclei of differing size. It can just be seen how the larger the nucleus, the faster the potential deviates from the Coulomb potential at short electron-nucleon distances. It should be noted that the curves have been offset slightly for clarity.

a greater rate the larger the nuclear size, as illustrated in Figure 2.7.

It is *purely* the field shift from which the charge radii are extracted; as mentioned previously, however, it is the *total* isotope shift which is obtained from spectroscopic measurements – these need to be separated into their mass and field components in order for charge radius calculations to be performed.

2.2.3 Isomer shift

Even within the same isotope, nuclear size and shape will vary between states. This leads to a specialised case of the isotope shift, known as the isomer shift, from which the change in mean-square charge radii between different states in the same nucleus can be extracted. Spearheaded by the theoretical calculations for ^{115g,115m}In by Weiner [26], and first observed experimentally in the study of ^{197g,196m}Hg by Melissinos and

Davis [27], the isomer shift has since become a powerful test of the nuclear shell model due to its more direct dependence on the nuclear information than that of the isotope shift – a key factor in the motivation for the ^{42g,42m}Sc study.

It is common practice to assume that the mass shift is negligible for an isomer shift, since both nuclear states involved are in the same isotope and therefore any mass difference is small and can be attributed to the excitation energy of the isomeric state. However, the effect of incorporating the excitation energy into the mass of the isomer was investigated for the ^{42g,42m}Sc isomer shift; this will be explained in greater detail in Chapter 5.

2.2.4 Mean-square charge radius

The mean-square charge radius of an atomic nucleus, $\langle r^2 \rangle$, is a fundamental quantity which gives a measure of charge distribution throughout the nuclear volume in such a way that is not only complementary to the electric quadrupole moment, but also sensitive to nuclear size as well as shape. There are three distinct components to the charge radius of a non-spherical nucleus. The first of these is the *volume component*, which arises due to the increase in nuclear volume across an isotope chain. According to the liquid-drop model (to be explained more in due course), nuclear volume increases with $A^{1/3}$; hence, assuming the liquid-drop model holds, $\langle r^2 \rangle$ would be expected to increase with increasing $A^{2/3}$ [4].

The second component arises from the nuclear shape, with $\langle r^2 \rangle$ being different for spherical and deformed nuclei of the same volume. This is given by

$$\langle r^2 \rangle = \langle r^2 \rangle_{\text{sph}} \left(1 + \frac{5}{4\pi} \sum_i \langle \beta_i^2 \rangle \right) + 3\sigma^2, \tag{2.47}$$

where $\langle r^2 \rangle_{\text{sph}}$ is the mean-square charge radius of the corresponding spherical nucleus (i.e. a spherical nucleus of the same volume), and $\langle \beta_i^2 \rangle$ is the **mean-squared deformation parameter** for a multipole of order i – i.e. quadrupole deformation occurs when $i = 2$, octupole deformation occurs when $i = 3$ etc. To a good approximation, this can be simplified to [28]

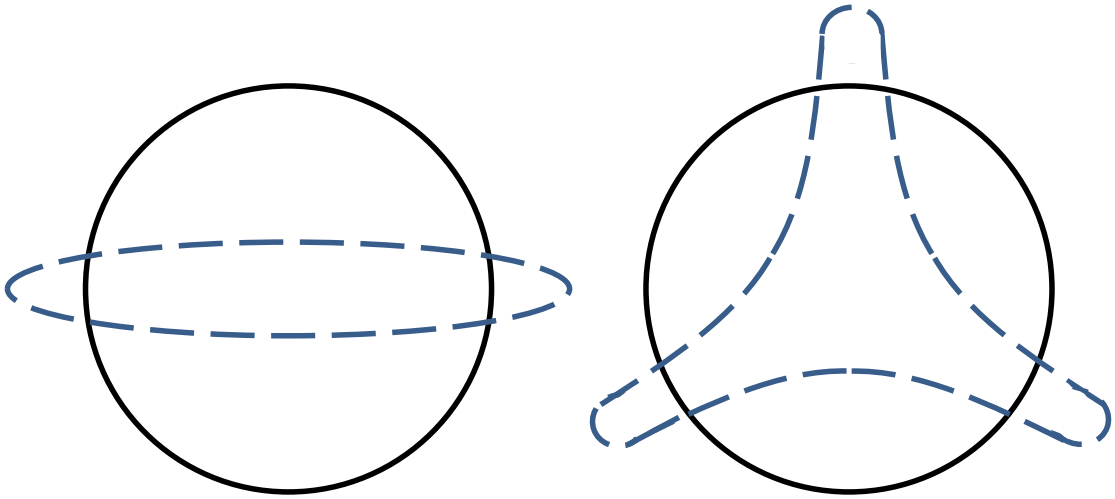

Figure 2.8: Schematic showing quadrupole (left) and octupole (right) vibrations (dashed blue lines) of a spherical nucleus (solid black line).

$$\langle r^2 \rangle \approx \langle r^2 \rangle_{\text{sph}} \left(1 + \frac{5}{4\pi} \langle \beta_2^2 \rangle \right) + 3\sigma^2, \tag{2.48}$$

where σ is the nuclear surface diffuseness parameter, which is assumed to be constant. This, in turn, means the change in mean-square charge radius between two isotopes A and A' (to 2^{nd} order) can be expressed as [5, 28]

$$\delta\langle r^2 \rangle^{A,A'} = \delta\langle r^2 \rangle_{\text{sph}}^{A,A'} + \langle r^2 \rangle_{\text{sph}} \frac{5}{4\pi} \delta\langle \beta_2^2 \rangle^{A,A'}. \tag{2.49}$$

The third and final component to $\delta\langle r^2 \rangle$ occurs due to the nuclear deformation. Whether the deformation is static or varies with time due to zero-point fluctuations also has an effect on the magnitude of $\langle r^2 \rangle$, as this can give rise to large values of the mean-square quadrupole deformation parameter, $\langle \beta_2^2 \rangle$ (large quadrupole vibrations) even if $\langle \beta_2 \rangle^2$ is zero [25, 4], as illustrated in Figure 2.8.

For nuclei exhibiting axial symmetry, the static quadrupole deformation parameter $\langle \beta_2 \rangle$ can be extracted from the intrinsic quadrupole moment via equation (2.50)

$$Q_0 = \frac{5Z\langle r^2\rangle_{\rm sph}}{\sqrt{5\pi}}\langle\beta_2\rangle(1+0.36\langle\beta_2\rangle). \tag{2.50}$$

Equation (2.50) gives a measure of the static deformation. The isotope shift (and corresponding change in mean-square charge radius extracted from it) arises from the total deformation (i.e. the sum of the static and dynamic components). Therefore, a measure of the dynamic deformation can be obtained by comparing the mean-squared deformation parameter with the square of the mean; i.e. the greater the difference between $\langle\beta_2^2\rangle$ and $\langle\beta_2\rangle^2$, the greater the dynamic component to the total deformation. This can be expressed mathematically as

$$\langle\beta_2^2\rangle = \langle\beta_2\rangle^2 + (\langle\beta_2^2\rangle - \langle\beta_2\rangle^2), \tag{2.51}$$

where the quantity $\langle\beta_2^2\rangle - \langle\beta_2\rangle^2$ gives the dynamic deformation.

Nuclei with $\langle\beta_2^2\rangle > \langle\beta_2\rangle^2$ (i.e. having a significant dynamic component to the deformation) are said to be *soft*, as opposed to *rigid* nuclei (i.e. those having static deformation), for which $\langle\beta_2^2\rangle \approx \langle\beta_2\rangle^2$. Experimental values of nuclear charge radii can therefore be compared against rigid-body estimates – values of $\delta\langle\ r^2\ \rangle^{A,A'}$ are calculated using the deformation obtained from the measured $Q_{\rm s}$ value and compared with experimentally determined values – in order to yield a measure of the β-softness, and to study how it varies across an isotope chain.

2.2.5 King plot and calibration of atomic factors

The M and F factors are dependent upon the atomic transition (between J-states) under study but independent of the isotopes, and they are calculated specifically for the transition. However, M and F are difficult to calculate (calculating M is particularly tricky). Such difficulties are usually minimised by producing a King plot.

A King plot allows the F and M factors to be calibrated for the optical transition selected for study. In order to do this, we require existing values $\delta\langle\ r^2\ \rangle$ or measurements of isotope shifts on a transition for which the F and M factors are either already known or are easier to calculate.

The King plot is constructed by plotting the modified isotope shift for a previously studied transition against that for the transition under study for the same pair of isotopes. The isotope shifts for two transitions can be expressed as

$$\delta\nu_i^{A,A'} = M_i\frac{A'-A}{AA'} + F_i\delta\langle r^2\rangle^{AA'} \tag{2.52}$$

for transition i, and

$$\delta\nu_j^{A,A'} = M_j\frac{A'-A}{AA'} + F_j\delta\langle r^2\rangle^{AA'} \tag{2.53}$$

for transition j, where M_i, M_j, F_i and F_j are the mass and field factors for the respective transitions i and j.

The *modified* isotope shifts are obtained by multiplying equations (2.52) and (2.53) by a mass scaling factor such that

$$\delta\nu_{mod}^{AA'} = \frac{AA'}{A'-A}\delta\nu^{AA'}. \tag{2.54}$$

Thus, for transition i the modified isotope shift is given by

$$\delta\nu_i^{AA'}{}_{mod} = \frac{AA'}{A'-A}F_i\delta\langle r^2\rangle + M_i^{AA'}, \tag{2.55}$$

and that for transition j by

$$\delta\nu_j^{AA'}{}_{mod} = \frac{AA'}{A'-A}F_j\delta\langle r^2\rangle + M_j^{AA'}. \tag{2.56}$$

From equations (2.55) and (2.56), it can be seen that plotting one modified isotope shift against the other will eliminate $\delta\langle\ r^2\rangle$. Such a plot is a straight from which a gradient equal to

$$m = \frac{F_i}{F_j}, \tag{2.57}$$

and intercept equal to

$$c = M_i - M_j\frac{F_i}{F_j}, \tag{2.58}$$

can be deduced. This technique therefore allows the M and F factors of the transition of interest (chosen for reasons of e.g. spectroscopic efficiency) to be related to those of

another transition; the latter transition may have been selected to ease the theoretical calculation of M and F, and measuring only three isotopes (thus obtaining two isotope pairs) is sufficient for a calibration. From this plot, the $\delta\langle\ r^2\ \rangle$ values for a measured isotope chain can then be determined. Alternatively, values of $\delta\langle\ r^2\ \rangle$ may already be available; if this is the case, values of $\delta\langle\ r^2\ \rangle$ may be treated as isotope shift values with $M = 0$ and $F = 1$, and used to form the King plot.

2.2.6 Multi-configuration Dirac-Fock calculations of atomic factors

In many cases, a suitable reference transition may not be available for a King plot to be constructed. In such cases, M and F need to be calculated for the transition of interest using the multi-configuration Dirac-Fock (MCDF) method based on the many-body Schrödinger equation [29]

$$\left(\sum_{i=1}^{N} \frac{p_i}{2m} - \sum_{i=1}^{N} \frac{Z}{r_i} + \sum_{i<j}^{N} \frac{1}{r_{ij}} \right) |\Psi\rangle = E_0|\Psi\rangle. \tag{2.59}$$

In equation (2.59), the nucleus is assumed to be an infinitely heavy point charge with negligible kinetic energy. As discussed previously, the isotope shift arises largely from the finite size of the nucleus, meaning that its kinetic energy cannot be neglected.

The MCDF method is highly advantageous in that it allows atoms with many open shells to be treated in a similar manner to closed-shell atoms [30]. An atomic energy level in the MCDF method is built up from configuration state functions (CSF), which can be expressed as a linear combination of Slater determinants [31, 30],

$$\phi_\alpha(PJM) = \sum_{r=1}^{n_c} c_r(\alpha)|\gamma_r PJM\rangle, \tag{2.60}$$

all of which exhibit the same symmetry. Here, n_c is the number of CSFs present, and $c_r(\alpha)$ represents the level in this basis. From equations (2.37) and (2.60), the normal and specific mass shifts can expressed in the MCDF method as [21]

$$E_{\mathrm{NMS}} = \langle\gamma_r PJM|\frac{m_N + m_e}{2m_N m_e} \sum_i \vec{p}_i^{\,2}|\gamma_r PJM\rangle, \tag{2.61}$$

$$E_{\mathrm{SMS}} = \langle \gamma_r PJM | \frac{1}{M} \sum_{i>j} \vec{p}_i \cdot \vec{p}_j | \gamma_r PJM \rangle. \tag{2.62}$$

A spherical nucleus is assumed in order to obtain a single field shift factor, F, for a whole isotope chain. In order to do this, one assumes a Fermi nucleus; i.e. one for which the Fermi distribution can be assumed to hold for the charge density [21, 30]

$$\rho(r) = \frac{\rho_0}{1 + e^{(r-c)/\sigma}}, \tag{2.63}$$

where c is the radius at half-charge density, and σ is the surface diffuseness (same as defined before), which is related to the nuclear skin depth, t, by

$$\sigma = \frac{t}{4 \ln 3}. \tag{2.64}$$

For more complex transitions involving many electrons, difficulties in correctly calculating the F and M factors arise from correlation contributions not accounted for – an example of the classic quantum many-body problem. Whilst the MCDF method takes this into account by incorporating electron "replacements" from bound states to virtual "active" states, the rapid increase in the size of the wavefunction requires truncation of the active space. For this reason, this approach has mainly been tested for isotope shifts of lighter elements and isotopes with simpler valence shell structures [30].

2.2.7 Alternative methods of measuring charge radii

It is possible to utilise non-optical methods in order to extract nuclear charge radii; however, these share a common disadvantage of being applicable only to stable or long-lived isotopes. In certain cases, however, these methods can be combined either with each other, or with optical measurements using a transition (or combination of transitions) that may not be the most spectroscopically efficient of the transitions available, but are simpler – therefore allowing for a more reliable calculation of F and M for a given isotope chain.

Electron scattering

Charge radii can be extracted by means of high-energy elastic electron scattering experiments. An electron will scatter off the nucleus, transferring an amount of momentum, q to it. The nuclear charge distribution is obtained from the plane-wave Born approximation, where the Form factor $F(q)$ is given for a spherically symmetric charge distribution by [32]

$$\rho(r) = \frac{1}{2\pi^2} \int F(q) \frac{\sin(qr)}{qr} q^2 \mathrm{d}q, \tag{2.65}$$

i.e. $\rho(r)$ is the Fourier transform of $F(q)$. Electron scattering is advantageous over optical techniques in the case of very light nuclei, owing to their extremely small field shifts. For this reason, electron scattering has been utilised to find the charge radii of the neutron [33] and alpha particle [34]. However, a major limitation of electron scattering experiments arises from the allowed range of q values that the form factor can be studied over [32]; for many heavier isotopes, the values of q that the form factor would need to be studied over renders this method impractical.

X-ray spectroscopy

Although classed as a non-optical method, the X-ray spectroscopic technique is in many ways analogous to the optical methods used for short-lived radioisotopes, and is in many cases implemented in conjunction with optical measurements. X-ray measurements of isotope shifts only involve closed-shell or single-particle configurations [4], thus eliminating much difficulty with regards to calculating the atomic factors; however, the technique is disadvantageous in terms of precision (hence the need to often combine data from X-ray and optical measurements).

Muonic atom x-ray spectroscopy

As the muon is heavier than the electron, a muon in an atom will lie closer to the nucleus than an "equivalent" electron. The system can be treated as an ion with a single electron, allowing theoretical calculations of the muonic energy levels for a point nucleus and comparison with those observed experimentally; the difference between these can be used to extract charge radius measurements.

2.3 Testing nuclear models with collinear laser spectroscopy

How nuclear moments and charge radii vary across an isotope chain provides, in many cases, a stringent test of the validity of various nuclear models. Agreement of experimental and theoretical values for nuclear moments and charge radii vary widely from model to model. It has been found that, generally speaking, the best theoretical estimates of such nuclear properties have been given by the liquid-drop model and the shell model.

2.3.1 The droplet model

Trends in the softness of nuclear deformation can be inferred by comparing laser spectroscopic measurements of the nuclear charge radii with theoretical estimates calculated assuming only static deformation. These have been found to be in reasonable agreement with values calculated using the droplet model, whose estimates of nuclear binding energy are given by the Bethe-Weizäcker semi-empirical mass formula (SEMF) [35]

$$E_b(Z,A) = a_V A - a_S A^{2/3} - a_C \frac{Z^2}{A^{1/3}} - a_A \frac{(Z-\frac{A}{2})}{A} \pm \delta(Z,A), \tag{2.66}$$

where $a_V A$ is the volume term, $a_S A^{2/3}$ is the surface term, $a_C \frac{Z^2}{A^{1/3}}$ is the Coulomb term, $a_A \frac{(N-Z)^2}{A}$ the asymmetry term and $\delta(Z,A)$ is the pairing term.

The different nuclear mass formulae have led to the following formulation of the charge radius [36]

$$r = R_0 A^{1/3}, \tag{2.67}$$

where R_0 and $\langle r^2 \rangle$ have experimentally been verified to be related by [36]

$$R_0 = \sqrt{\frac{5}{3}} \langle r^2 \rangle^{1/2}. \tag{2.68}$$

Whilst successfully reproducing macroscopic effects – such as the general increase in nuclear radius across an isotope chain – the liquid drop model fails to reproduce

microscopic phenomena, such as the kinks in charge radii observed at shell closures. It is this model that is used in equation (2.49) in order to try to separate deformation and volume effects.

2.3.2 The spherical shell model

Nucleons in nuclei can be thought of as existing in discrete energy levels, analogous to those of electrons in atoms. Like electrons, protons and neutrons are fermions and therefore obey the Pauli exclusion principle. The motion of each individual nucleon is described as being constrained by a potential arising from contributions from all nucleons present. This potential is best described as being a coupling of the Woods-Saxon and spin-orbit potentials. The Woods-Saxon potential can be expressed as [37]

$$V(r) = -\frac{V_0}{1 + e^{\frac{r-R_0}{\sigma}}}, \tag{2.69}$$

where all symbols are as defined earlier.

At certain numbers of either protons (Z) or neutrons (N), known as magic numbers, nuclei behave very differently to those with neighbouring N or Z numbers. Occurring at such Z or N numbers are what are known as shell closures; each shell is described by the quantum numbers $[n, l, j]$ – as previously defined. So far, the experimentally verified magic numbers of protons or neutrons are 2, 8, 20, 28, 50, 82 and 126. The first three are simply double the first three numbers from Pascal's triangle; subsequent magic numbers are double the Pascal's triangle numbers plus corrections for the nuclear spin-orbit interaction. Therefore, we can predict more using [38]

$$MN_m = (m^2 - m)k + \frac{1}{3}(m^3 + 5m), \tag{2.70}$$

where m is any positive integer, and $k = 1$ if $m = 1, 2, 3$ and is zero otherwise.

There is much experimental evidence supporting the shell model. Isotopes with magic Z or N numbers are found to be more stable than those with neighbouring Z or N, and are therefore more abundant and have a greater binding energy. Such nuclei are also spherical – i.e. their electric quadrupole moment is zero. Magic nuclei also have a lower absorption cross section and first excited states at higher energies than those

with neighbouring Z or N. It is the nuclear spin-orbit coupling that leads to the splitting of e.g. the $1p$ shell into $1p_{1/2}$ and $1p_{3/2}$ subshells, which is illustrated in Figure 2.9.

Charge radii can also be used in order to verify the shell model; looking at charge radii across an isotope chain an upward kink is usually seen at a shell closure. However, one phenomenon which the shell model fails to explain is the odd-even staggering (OES) of charge radii across an isotope chain, which is thought to be accounted for by the effects of nucleon pairing (to be discussed in greater detail later).

Laser spectroscopic measurements of nuclear moments and charge radii can also be used as a test of the model space and the associated effective interactions being used. Such experimental measurements can be compared with shell model calculations in order to search for missing physics (arising from significant discrepancies between experimental measurements and shell model calculations) or verify predicted features and/or trends along an isotope chain.

2.3.3 The deformed (Nilsson) shell model

For the case of non-magic nuclei, the case of the electric quadrupole moment not necessarily being zero – and the effect this has on the nuclear shape – needs to be taken into account, as the spherical potential used in the shell model is no longer a good potential. A major consequence of this is that states in a non-spherical nucleus cannot be identified using the spectroscopic notation (s, p, d, f etc.) with which we have so far become accustomed to [39]. Thus, modifications need to be made to the shell model to account for the deformation.

The spherical shell model can be considered a special case of the Nilsson model – named after Sven Gösta Nilsson, who first calculated the energies of the states in a deformed nucleus in the 1950's [4] – in which the energy levels are given by the quantum numbers $\Omega^{\pi}[N, n_z, \Lambda]$ [4]. In this formalism, Ω defines the projection of the total angular momentum $j = l + s$ onto the axis of symmetry (this describes the splitting of each spherical shell model level into $2j + 1$ Nilsson levels, with the magnitude of the splitting increasing as the magnitude of the nuclear deformation increases), π is the

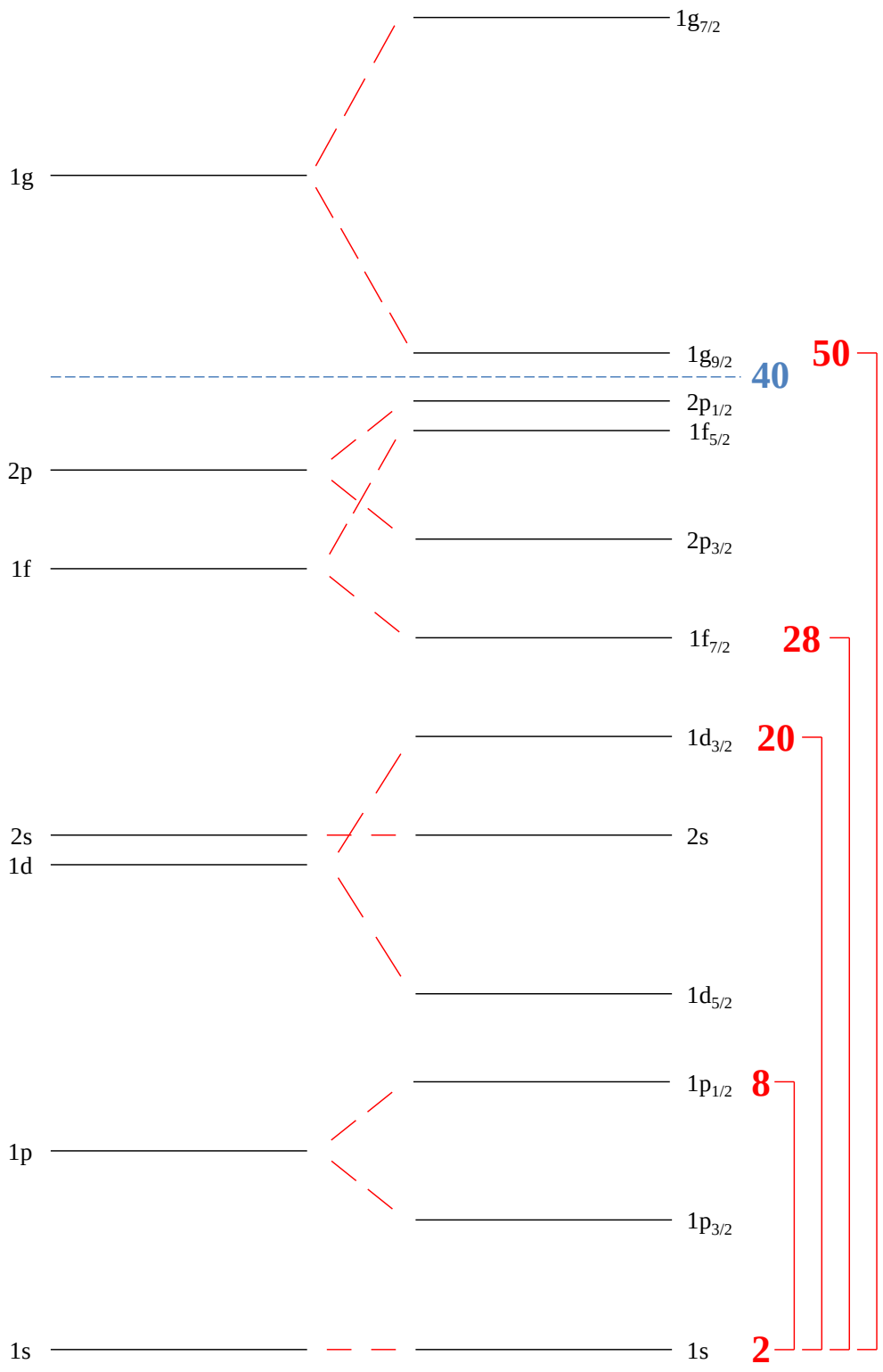

Figure 2.9: Shell model energy level diagram, showing the nuclear magic numbers up to 50. The dashed blue line indicates 40 as being a semi-magic number.

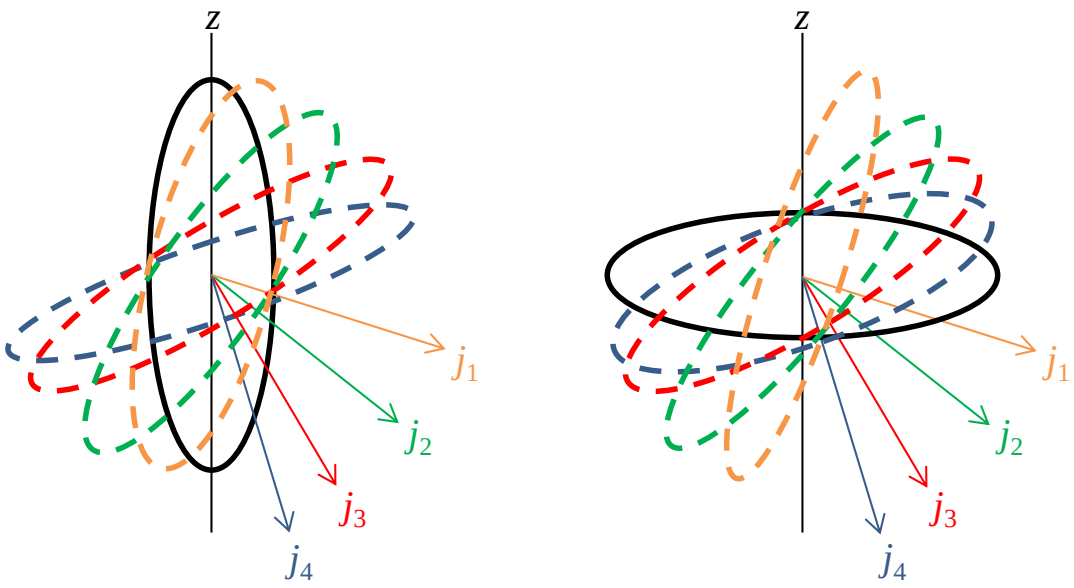

Figure 2.10: The possible nucleon orbits for a spin-7/2 nucleus with prolate (left) and oblate (right) deformations [39].

parity of the state, N is the principal quantum number, n_z is the component of N along the axis of symmetry, and $\Lambda = l_z$ is the projection of the orbital angular momentum l onto the axis of symmetry. Figures 2.11 and 2.12 shows the orbitals for both protons and neutrons, together with the combinations of $\Omega^{\pi}[N, n_z, \Lambda]$ for each Nilsson orbital, and how they differ from those of the spherical shell model.

One thing worthy of note is the discrepancy between single-particle orbitals calculated using the aforementioned Nilsson potential and the Woods-Saxon potential; specifically the differing shape parametrisations these models give [40]. However, by equating the $\beta-$ (Woods-Saxon) and $\epsilon-$ (Nilsson) shape parametrisations, a transformation can be made between the two by calculating a series of multipole moments rather than the absolute value of the potential for either the Nilsson or Woods-Saxon cases [40].

Validation of both the spherical shell and Nilsson models can be achieved simulta-

neously by studying the nuclear moments and charge radii and comparing experimental measurements with theoretical calculations. With regards to this work, the results for the charge radii of ^{42g,42m}Sc, are an example of this.

2.3.4 The Bohr-Mottelson collective model

The spherical shell model and Nilsson model may work well for single-particle estimates, but what of the case of multiple valence particles? Aage Bohr and Ben R. Mottelson explained this with their collective model, which treats the nucleus as a drop of liquid able to vibrate and rotate [42].

The collective model was successful in explaining the discrepancies between single-particle estimates of electric quadrupole moments and corresponding experimental values [39]. However, comparisons of experimental charge radii against theoretical rigid-body calculations and observing the trend in β-softness across isotope chains has shown up some shortcomings. The collective model gives the following formula for $\delta\langle\ r^2\ \rangle$ [42]

$$\delta\langle r^2\rangle = \frac{4}{5}R_0^2 A^{-1/3} + \frac{3}{4\pi}R_0^2 A^{2/3}\delta\langle\beta^2\rangle, \tag{2.71}$$

Soon enough, however, values given by equation (2.71) were found to be inconsistent with the experimental charge radii, since shell effects are not accounted for explicitly, only through the deformation parameter.

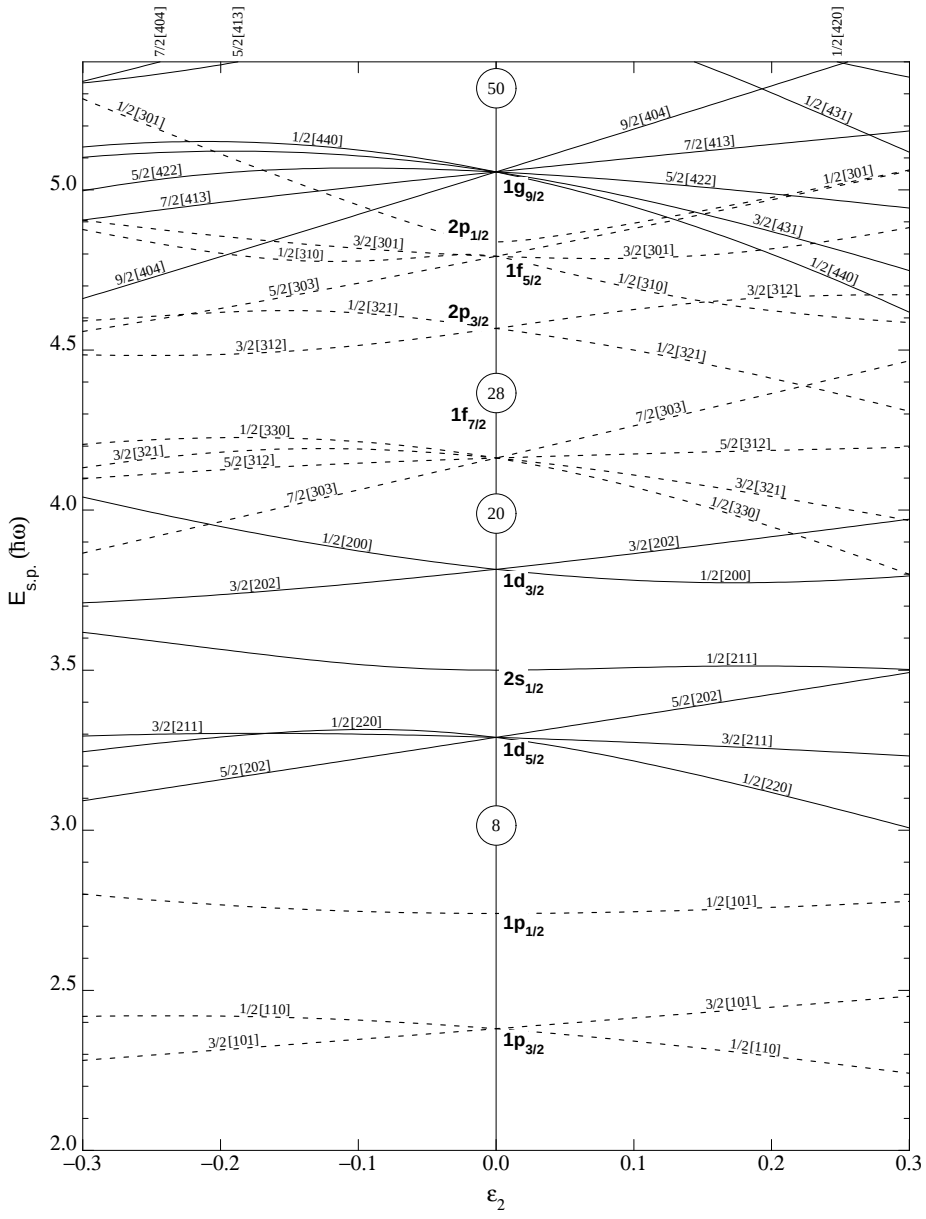

Figure 4. Nilsson diagram for protons or neutrons, Z or N ≤ 50 (ε_4 = 0).

Figure 2.11: Nilsson diagram for both protons and neutrons, for $N, Z \leq 50$ [41].

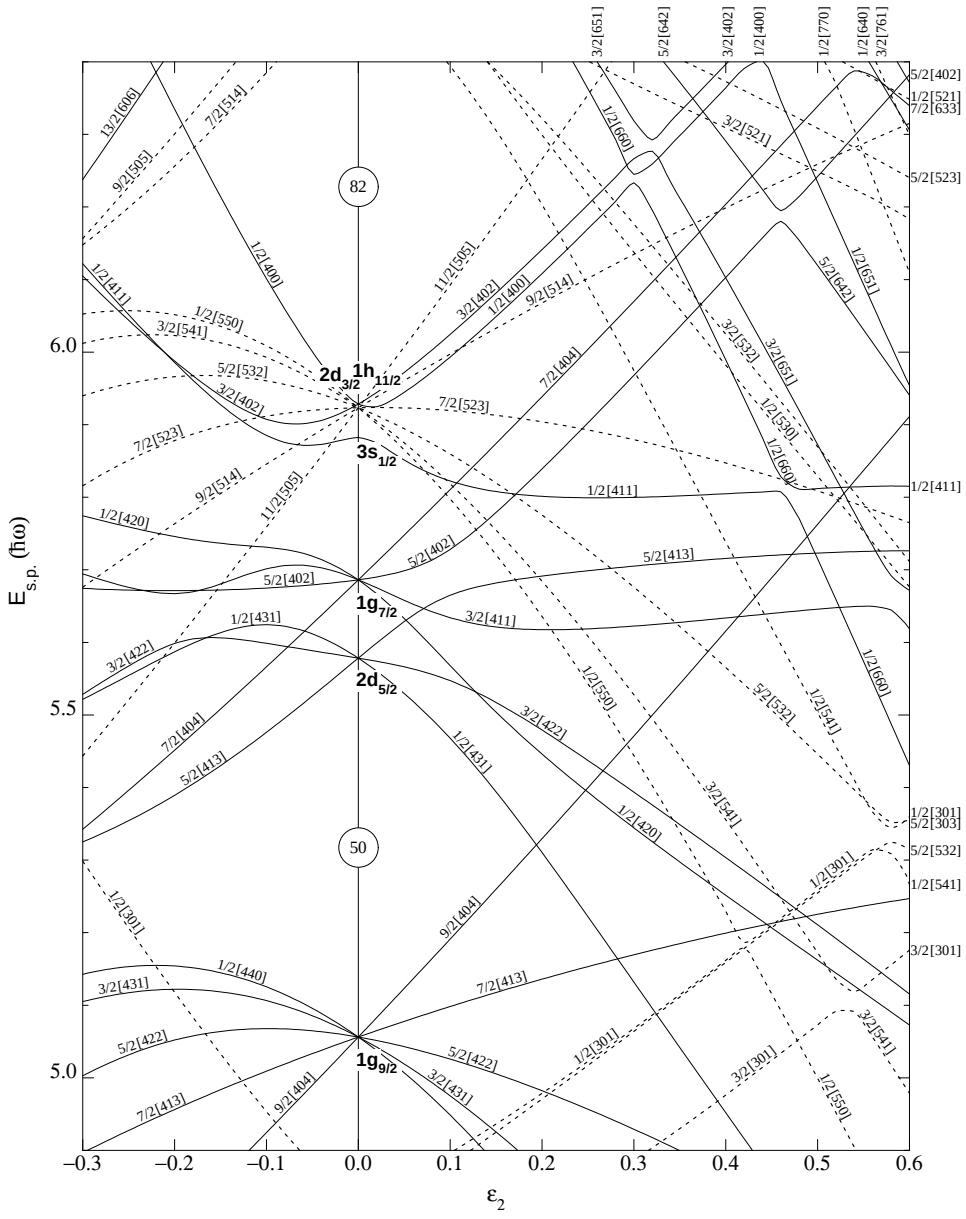

Figure 5. Nilsson diagram for neutrons, 50 ≤ N ≤ 82 ($\varepsilon_4 = \varepsilon_2^2/6$).

Figure 2.12: Nilsson diagram for both protons and neutrons, for $50 \leq N, Z \leq 82$ [41].

Chapter 3

The collinear laser spectroscopy technique

Laser spectroscopic methods are ideal for measuring hyperfine structures and isotope shifts for their inherently high efficiency and resolution – essential given the magnitude range of hyperfine splittings and isotope shifts (typically from a few MHz to many GHz). There are also tunable lasers available whose line widths are smaller than atomic line widths.

The interaction of laser light with an atom or ion results in resonant excitation of an atomic electron at hyperfine transition frequencies within the optical wavelength range – i.e. an atomic electron is excited from a hyperfine component (F-state) of the lower J-state to one belonging to the upper J-state in the selected atomic transition. Photons are emitted from the ions as they de-excite; these are detected by a photomultiplier tube placed across the laser-ion interaction region. A fluorescence spectrum is formed by counting the number of photons as the frequency is scanned.

3.1 Advantages of collinear laser spectroscopy

The collinear laser-ion beam geometry is highly advantageous, as it allows for a longer interaction region between the laser and ion beams than for e.g. a crossed-beam geometry, which in turn leads to a longer interaction time between them – as illustrated in Figure 3.1. The result of this is more statistics obtained during an experimental run

for the collinear geometry than for crossed beams.

Collinear fluorescence spectroscopy is fast; even very short-lived ions can be easily transported from the ion source to the laser spectroscopy station before they decay. The technique also offers very high resolution. From the non-relativistic kinetic energy formula $E = \frac{1}{2}mv^2$, it can be shown that the energy spread of an ion beam is related to the ion velocity, and the velocity spread by the formula $\delta E = mv\delta v$. Therefore, as δE remains constant, if v increases, δv must decrease. Since δv is proportional to the frequency spread, δf – via the Doppler effect – as δv is reduced, so too is δf. In the crossed-beam method, on the other hand, the beam energy is much lower, which not only leads to a greater velocity spread but also poses the problem of the radioactive species reaching the interaction region before decaying.

The collinear fluorescence spectroscopy technique also allows the laser to be "locked" to a reference frequency – e.g. a frequency corresponding to a molecular transition. This allows the frequency scan to be performed by means of applying a secondary voltage, known as a tuning voltage, across the laser-ion interaction region, rather than scanning the laser across the hyperfine structure. Here, it is the ion velocity that is scanned. This velocity is transformed, via the Doppler shift, into the frequency against which the photon counts are plotted. This method of frequency scanning is far more stable than scanning the laser across the hyperfine structure, and is easier to calibrate; the voltages can be measured to a high degree of accuracy using a high-precision voltmeter and a potential divider. By scanning a voltage rather than the laser frequency, the laser can be stabilised to a fixed frequency, which reduces the problems of mode hops and scanning non-linearly or inconsistently between scans.

3.2 The dye laser

The laser used for this work is a SpectraPhysics 380 continuous-wave (CW) dye laser. The crucial element of a laser suitable for radioactive ion spectroscopy is tunability – i.e. the ability to select and maintain a certain wavelength in a controlled manner. Lasers using organic dyes as the gain medium are ideal in situations where tunability is important – not just due to their wide wavelength range, but also because of the

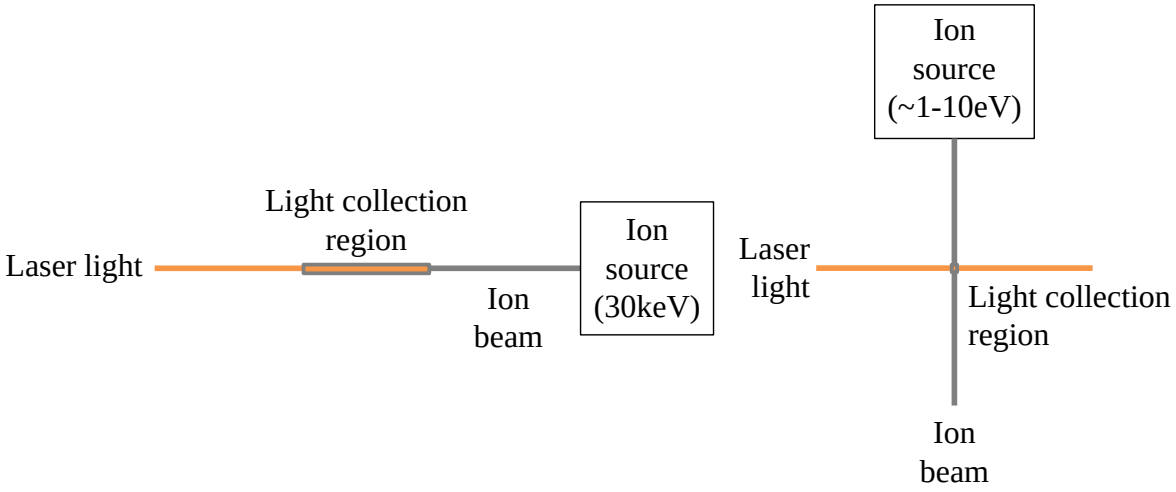

Figure 3.1: Comparison of the collinear and crossed (i.e. perpendicular) laser-ion beam geometries, showing the larger light collection region which leads to better statistics and higher resolution.

ability to switch between dyes to generate different wavelengths using the same laser.

The dye laser works on the principle of optical pumping, in a manner not too dissimilar to that used to excite ions into metastable states for spectroscopy. The dye is pumped up into the cavity area in the form of a fast-moving dye jet, onto which light from another laser, known as a pump laser, is focused. The light from the pump laser "pumps" electrons from the ground state into a metastable state until a population inversion (i.e. a greater number of dye molecules in the excited state than in the ground state) is achieved.

Commonly used dyes include Rhodamine, Pyridine and Coumarin species among others. Such dyes have emission bands lying at longer wavelengths than their absorption bands, and both their absorption and emission spectra cover a wide wavelength range. Such characteristic features arise from the complex molecular structure of these dyes; there are many rotational and vibrational states in such molecules, leading to a continuum due to the overlapping of rovibrational states. A typical laser dye will have an energy level structure consisting of singlet and triplet bands as shown in Figure 3.2. This is the driver behind the use of a fast dye jet, rather than the dye being stationary.

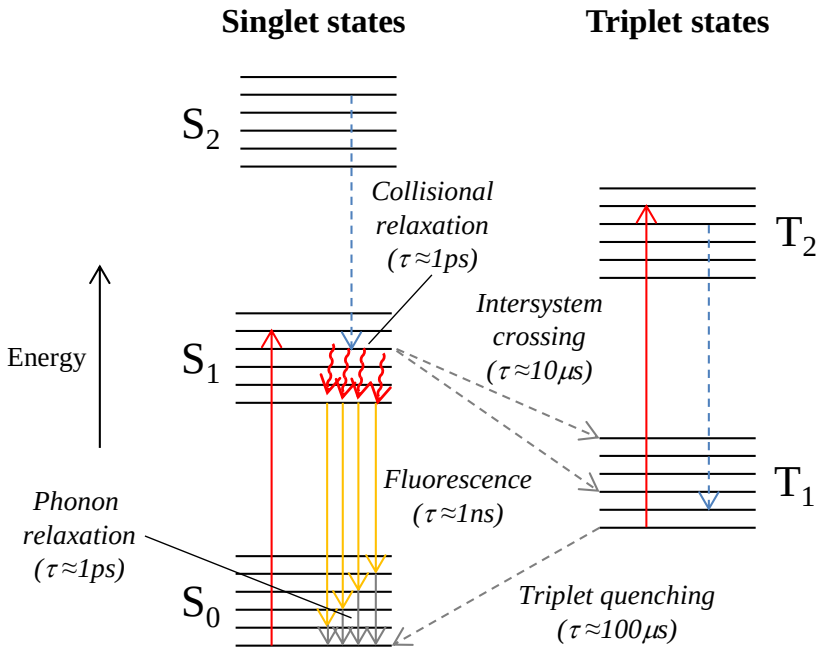

Figure 3.2: Energy level diagram showing typical singlet and triplet states and allowed transitions for a laser dye.

After pumping, collisional relaxation within the S_1 states to the band head occurs on a much shorter timescale than the fluorescence decay to the S_0 band. This allows the required population inversion to build up.

For successful lasing, transitions involving any triplet states need to be suppressed [43]. If a stationary sample of dye were used, or a slow-moving dye jet, this would give sufficient time for intersystem crossing to occur, thus populating the longer-lived triplet states. This would drastically reduce the population inversion and, consequently, the probability of fluorescence.

3.2.1 The pump laser

An external source of energy is required in order to excite the dye molecules into metastable states, thus achieving the population inversion vital for the dye to serve as a laser medium. The pump laser used for the work undertaken here is a solid-state Nd:YVO_4 (Verdi) laser [44], frequency-doubled to a wavelength of 532nm. The Verdi

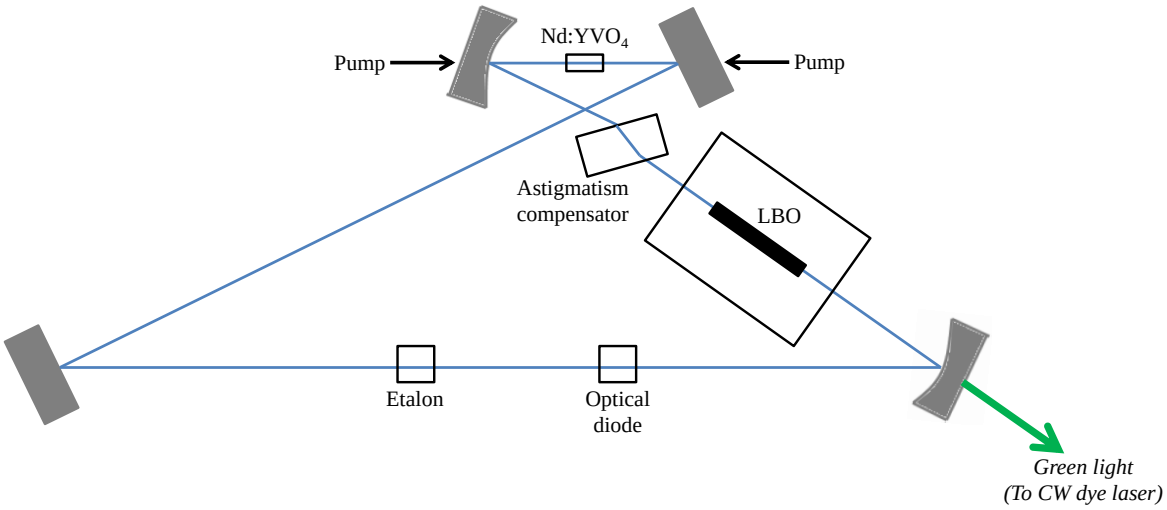

Figure 3.3: Schematic of a typical Verdi laser cavity, akin to that used for pumping the dye laser in this work.

laser cavity is illustrated in Figure 3.3. In the past, an Nd:YAG laser was used for pumping [24].

3.2.2 The cavity

Most dye lasers operate with a standing wave in the cavity. However, such lasers are disadvantageous for radioactive ion spectroscopy due to the regions of unused gain resulting from the standing wave minima. This results in regions of unused gain, causing lasing of other modes corresponding to regions of high gain; this is known as spatial hole burning [4], and renders single-mode operation difficult. Hence, for radioactive ion spectroscopy, a travelling-wave dye laser is preferred. The 380, in common with most other dye lasers, operates in a ring configuration. This allows for light to initially propagate bidirectionally, before being reduced to unidirectional by means of a polarising filter as shown in Figure 3.4. Other components of particular importance shown in Figure 3.4 are the scanning etalon and birefringent filter (transmission profiles shown in Figure 3.5), which work together so as to hinder all cavity modes bar the desired mode (and hence keep the laser on lock), and the dual galvanometer plates, whose

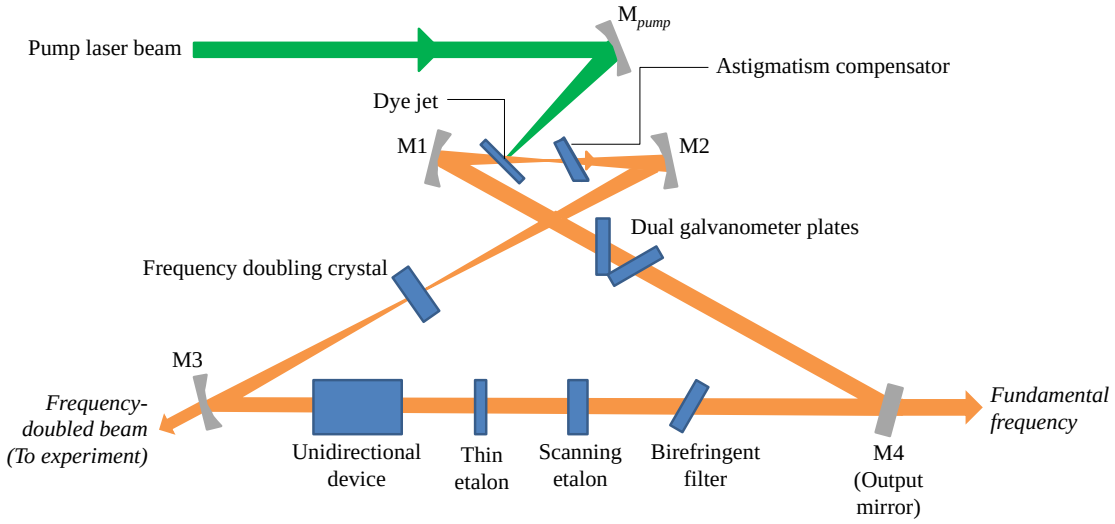

Figure 3.4: Schematic of the SpectraPhysics 380 dye laser, showing the ring configuration, as well as the individual components and the incident pump beam from the pump laser.

purpose is to change the effective cavity length.

3.2.3 Frequency stabilisation

In radioactive-ion spectroscopy experiments, high resolution and, therefore, a very stable laser frequency are essential. Any thermal and/or acoustic vibration will thus be highly undesirable as this will contribute significantly to the spectral line width [4]. The setup at IGISOL uses a SpectraPhysics Stabilok^{TM} system in order to lock the frequency of the laser. The Stabilok consists of two Fabry-Perot etalons. These are the reference etalon, which has a free spectral range (i.e. effective cavity length) of 0.5GHz, and the slave etalon, with a free spectral range of 8GHz [20]. The free spectral ranges of the two etalons are shown in Figure 3.6 as being the distance between peaks, whilst the width of the peak gives the reflectivity of the mirror, known as the finesse. The laser light passes through both these etalons; photodiodes are in place to monitor their transmission intensities [20]. The laser is locked to the reference etalon, which is sealed and temperature-stabilised.

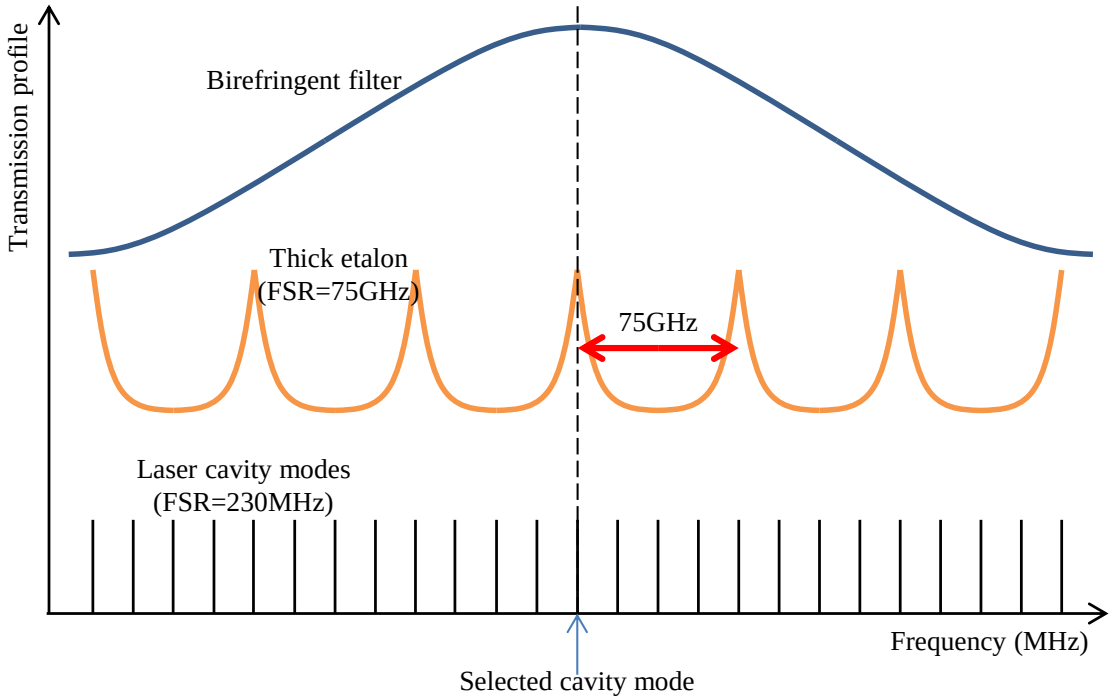

Figure 3.5: Schematic transmission profiles of the different components of the SpectraPhysics^{TM} 380 dye laser.

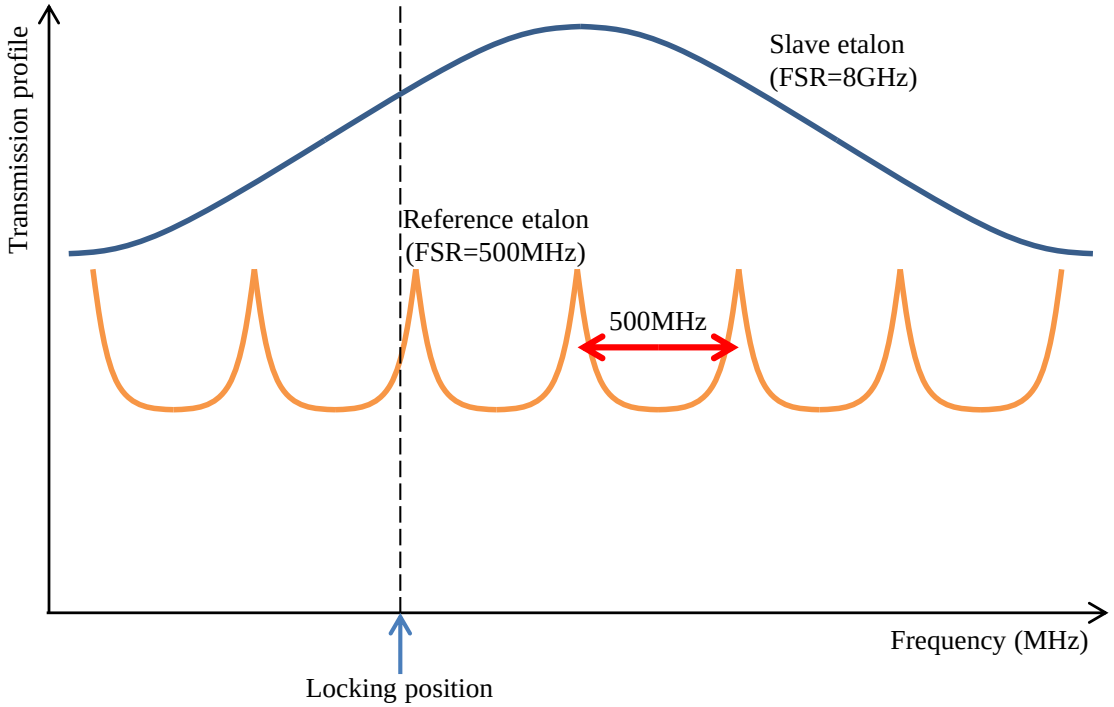

Figure 3.6: Schematic transmission profiles of the Stabilok^{TM} reference and slave etalons.

The slave etalon having a much broader transmission peak than the reference etalon (Figure 3.6) serves an important purpose. In the case of a deviation in frequency so large it no longer lies on the transmission peak of the reference etalon – e.g. if a mode hop occurs – then the system goes "off lock", and drives the frequency back to the correct position on the slave etalon transmission peak. Therefore, the system is back on the correct reference etalon peak and the system is back on lock once again.

The reference etalon is locked to a frequency corresponding to an absorption peak in molecular iodine (I_2). The use of an iodine cell is very useful not only for guarding against long-term drifts of the etalons, but also for the provision of a frequency reference.

3.2.4 Frequency doubling

It is not always the fundamental frequency, but often double that which is required for the experiment, since there are spectral lines present in the ultraviolet region for many ions. Therefore, a non-linear, frequency-doubling crystal is situated at the position of the auxiliary beam waist (see Figure 3.4). The beam incident on this crystal is of the fundamental frequency. Mirror M3 (as it is labelled in Figure 3.4) has a *dichroic* coating, so the beam it reflects is of the fundamental frequency, but the frequency-doubled beam passes straight through to the experiment where it meets the ion beam.

3.3 Spectral line widths

A real spectral line is not infinitely sharp, but has a finite width. There are two main factors contributing to this; the energy levels themselves are not infinitely sharp, and the atoms are moving relative to the laser. Alongside the intrinsic natural line width are other contributions, each of which act to broaden the spectral line – thus having a detrimental effect on the resolution of spectroscopic measurements.

3.3.1 Natural line width

It can be deduced from the Heisenberg uncertainty principle, $\Delta E \cdot \Delta t \approx \hbar$, that a transition between two quantum states cannot be infinitely sharp given that the upper

level has a finite lifetime, τ_f – thus, shorter-lived states have a larger the uncertainty in energy and therefore a broader range of frequencies:

$$\Delta\nu \approx \frac{\Delta E}{h} \approx \frac{1}{2\pi\Delta t}. \tag{3.1}$$

This gives rise to the natural line width of a spectral line. A transition from an arbitrary excited state $|n\rangle$ to any lower state $|n'\rangle$ will have a rate equal to $\gamma = \sum_{n'} A_{nn'}$, where $A_{nn'}$ is the matrix element describing the transition probability. So for instance, a transition from $|2\rangle$ to $|1\rangle$ would have a rate equal to $\gamma = A_{21}$. The total natural line width is obtained by adding together the γ-terms for both the upper and lower states. Thus, for transitions to the ground state, the natural line profile (from which the shape of the natural line width is obtained) will be of the form

$$\phi(\nu) = \frac{\gamma/4\pi^2}{(\nu - \nu_0)^2 + (\gamma/4\pi)^2}, \tag{3.2}$$

where the natural line width is given by

$$\Delta\nu = \gamma/4\pi. \tag{3.3}$$

Natural line width accounts for a very small fraction of the total line width compared to the components from collision, power and Doppler broadening.

3.3.2 Collision and power broadening

There are two further contributions to the Lorentzian component of a total line width; collision broadening and power broadening. Collision broadening, as its name suggests, arises from collisions between atoms. Such collisions mean that the phase of the emitted radiation is randomised, and if collisions are frequent enough (as they are in the IGISOL chamber when performing in-source spectroscopy), these will further broaden the observed spectral lines.

Power broadening arises from saturation of an absorbing transition due to incident radiation of a sufficiently high intensity, resulting in the rate of excitation to the higher state exceeding the rate of decay to the lower state – thus, the atom becomes transparent to the incoming radiation. During laser spectroscopy experiments, reducing the

laser beam intensity will often eliminate the issues presented due to power broadening.

If the frequency of collisions between atoms is ν_{coll}, and the saturation frequency is ν_{power}, the Lorentzian line profile now becomes

$$\phi(\nu) = \frac{\Gamma/4\pi^2}{(\nu - \nu_0)^2 + (\Gamma/4\pi)^2}, \tag{3.4}$$

where $\Gamma = \gamma + 2\nu_{\text{coll}} + 2\nu_{\text{power}}$ and the total Lorentzian line width $= \Gamma/4\pi$.

3.3.3 Doppler broadening

Of course, the atoms are moving relative to the observer, and the speed with which the atoms move is determined by the temperature of the sample. Maxwell's law of velocity distribution gives the number of atoms moving with a specific velocity

$$\mathrm{d}N(v_x) \propto e^{-\frac{mv_x^2}{2kT}} \mathrm{d}v_x. \tag{3.5}$$

This can now be combined with the Doppler effect formula

$$\frac{\nu - \nu_0}{\nu_0} = \frac{v_x}{c}, \tag{3.6}$$

in order to obtain the Doppler profile function

$$\phi(\nu) = \frac{1}{\Delta\nu_{\text{D}}\sqrt{\pi}} e^{-\frac{(\nu-\nu_0)^2}{(\Delta\nu_{\text{D}})^2}}, \tag{3.7}$$

where the Doppler width (FWHM) is given by

$$\Delta\nu_{\text{D}} = \frac{\nu_0}{c}\sqrt{\frac{2kT}{m}}. \tag{3.8}$$

The issue posed by Doppler broadening is one of the main reasons driving the collinear laser spectroscopy technique; it is possible to accelerate a beam of ions to a sufficient velocity to reduce the longitudinal velocity spread of the ions. This in turn reduces the Doppler broadening in the beam – hence, an acceleration voltage of 30kV, as used in this work, will reduce the Doppler broadening to the order of the natural line width.

3.3.4 The Voigt profile

The Doppler profile is a Gaussian function, not a Lorentzian. However, the Doppler profile and Lorentzian profile can be combined, in a convolution, to form a Voigt profile. Although there is no simple analytical form of the Voigt profile, there is a definite shape to it. A Voigt profile typically has a Gaussian "core", with the "wings" of a Lorentzian; this is due to the Lorentzian profile falling off at a lower rate than the Gaussian.

However, due to both the collinear spectroscopy technique itself and the use of the cooler, Doppler broadening is suppressed to such an extent that the spectral line profile is, to a good approximation, Lorentzian – i.e. the Doppler (Gaussian) component is negligible. Hence, only Lorentzian peaks are fitted to the data in the chi-squared minimisation routine used for the analysis of the data taken for this work.

Chapter 4

IGISOL IV: Experimental setup and methodology

The work presented here was carried out at the **I**on **G**uide **I**sotope **S**eparator **O**n **L**ine (**IGISOL**), at the University of Jyväskylä, Finland. Now in its fourth incarnation (hence, IGISOL IV), IGISOL was originally designed to facilitate fast extraction of short-lived radioactive ions. Since its original installation in the 1980's, IGISOL has gone on to play host to a wide range of nuclear structure experiments performed by collaborators from a number of institutions worldwide. The IGISOL is home not just to the isotope separator itself, but also to the collinear laser spectroscopy setup and the JYFLTRAP double Penning trap system used for mass measurements.

4.1 IGISOL

The process begins with the IGISOL isotope separator itself, inside which nuclear reactions are induced by means of a beam of charged particles (typically protons, deuterons or alpha particles, although ^{3}He beams have also been used [45]) from a cyclotron impinging upon the target. The K130 cyclotron, which IGISOL shares with other experiments taking place at JYFL, is now complemented by a new MCC30 cyclotron.

The target chamber, inside which nuclear reactions take place, houses the ion guide itself – central to the IGISOL setup. The ion guide consists of a chamber filled with a helium buffer gas, inside which is a thin foil of target material. The use of thin foil

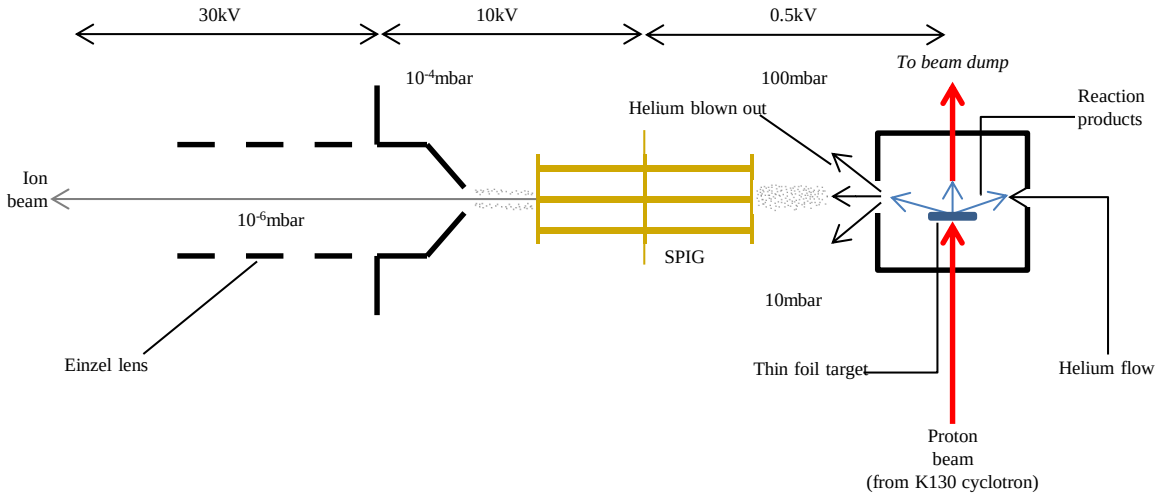

Figure 4.1: Schematic of the IGISOL ion guide chamber.

targets is crucial to the IGISOL technique as it allows the study of very short-lived radionuclides ($t_{1/2} < 10^{-3}$s) and that of refractory elements which would otherwise react chemically with the target material. At other ISOL facilities (e.g. ISOLDE-CERN [46] and TRIUMF [47]), thicker blocks of target material are used with a view to achieving higher radioactive yields; however, these would not be suitable for the radioisotopes studied as part of this work for the reasons (state lifetimes and/or chemistry) mentioned above.

A range of ion guides are available at IGISOL; which one is selected depends upon the desired nuclear reaction. There are ion guides for fission [48], light-ion fusion-evaporation [49] and heavy-ion fusion-evaporation [50] reactions. The ion guide is placed into the target chamber, into which the helium buffer gas is pumped. The primary beam from the cyclotron then enters the target chamber and impinges upon the target; this is how the nuclear reaction is induced. The reaction products recoil out of the target into the He buffer gas, leading to the radioactive species being largely in the singly charged state.

The next step is to form the ions into a beam. Originally, this was done by means of a conical skimmer electrode [51, 52]; more recently, however, this has been replaced with a sextupole ion guide (SPIG) [53].

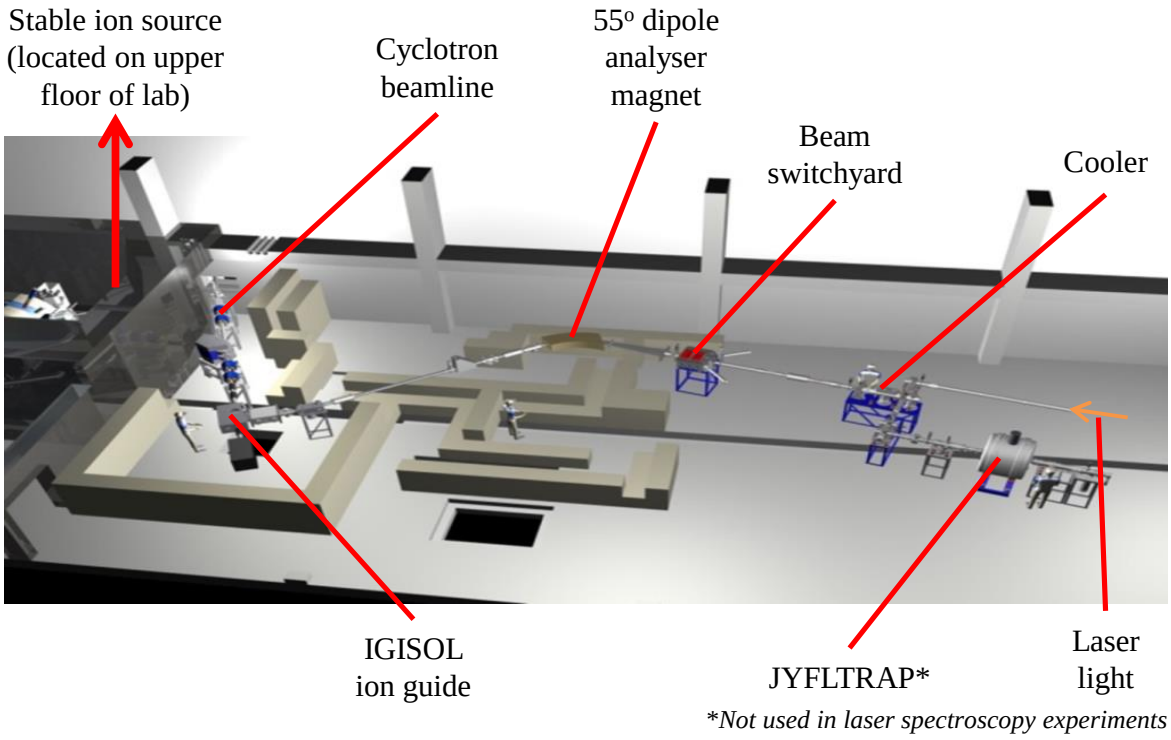

Figure 4.2: Schematic of the IGISOL laboratory, showing the beamline and various apparatus.

4.2 Extraction and mass separation of reaction products

Located at the end of the target chamber is the SPIG, which captures the ions from the emerging gas jet. The SPIG consists of six cylindrical rods, with an oscillating (positive/negative) voltage applied to each. The transverse emittance of the ions is reduced as they travel through the SPIG; this is achieved by applying 500V at a radio frequency of a few MHz to the SPIG. This focuses the ions along the central axis towards a conical extraction electrode. A series of large vacuum pumps are used to pump the helium buffer gas away. As the ions leave the SPIG they are accelerated through a 30kV potential (i.e. to an energy of 30keV for singly charged ions, 60keV for doubly charged ions), and directed towards the beamline via extraction electrodes at around -12kV [24] and focused onto the central axis (i.e. into a beam) using an Einzel lens.

At this point, of course, the beam consists of reaction products of varying mass, and the isotope of interest therefore needs to be separated out. This is achieved using

a dipole analyser magnet (see Figure 4.2) whose magnetic field can be set to the match the corresponding mass-to-charge ratio of the ions of interest. Thus, only the ions of the desired isotope travel beyond the point of separation to the cooler and, ultimately, to meet with the laser light.

4.3 The IGISOL beamline

The beamline is an evacuated tube along which the ion beam, once formed, is transported from the IGISOL target chamber to the laser spectroscopy station. A separate line to the JYFLTRAP double Penning trap system (used for mass measurements and separate from the laser spectroscopy setup), branches off from the laser line after the RFQ cooler-buncher, or *cooler* for short. The "intermediate components" (cooler, Faraday cups, microchannel plates, photomultiplier tube) are all located inside the beamline. The vacuum inside the tube is maintained by means of vacuum turbo pumps, and the beam is directed towards the laser spectroscopy station via a series of electrostatic deflectors [25]. The setup at IGISOL is illustrated in Figure 4.2.

4.4 Tuning and monitoring beam intensities

The ion beam is tuned electronically using *virtual instruments* (VI's), developed at JYFL using LabVIEW^{TM}. The software provides graphical user interfaces (GUI's) for tuning the ion beam at the positions of the SPIG, switchyard, cooler and light collection region; this is achieved by adjusting the voltage parameters on the quadrupole lens, Einzel lens and deflectors – and, where applicable, the radio frequency (i.e. for the SPIG and cooler).

It is necessary, of course, to monitor the radioactive ion yield at different points inside the beamline. In order to do this, there are Faraday cups placed in the vicinity of different components of the line. These metallic cups catch ions, and a measurement of the resulting current gives the number of ions per second. Faraday cups are a very useful tool, and are commonly used for monitoring ion beam intensities due to their simplicity and reliability [54]. On the IGISOL beamline, Faraday cups are situated just before the cooler and on the laser line. They are mounted on stalks and can be

inserted whenever required.

There are limitations on the ion rates measurable with a Faraday cup [55]. For sub-picoampere beam currents, another method of measuring the beam intensity is required. This problem is overcome by means of a *microchannel plate* (MCP) detector. This type of detector consists of an array of parallel miniature electron multipliers fabricated from a lead glass, which is treated so as to make the channel walls semiconducting [56], and therefore allows each channel to act as a continuous dynode photomultiplier [56, 57].

A high-purity germanium (HPGe) detector can also be mounted on the laser line in order to monitor the radioactive content of the beam and activities of each isotope present. Any further optimisation of the beam current, if needed, can be done accordingly. As mentioned previously, the use of a HPGe detector can also be used to assist with the actual nuclear structure study in the case of e.g. assigning and/or characterising isomeric states, as has also been done before at IGISOL [14].

4.5 The RFQ cooler-buncher

Although the IGISOL offers great advantages with regards to the range of half-lives and isotopes available for production and study, there is one major disadvantage – the high energy spread within the ion beam. This is remedied by means of a radio-frequency quadrupole (RFQ) cooler-buncher (referred to from here on as the "cooler"). The cooler is essentially a linear Paul trap – in which ions are decelerated and held within a potential well and subsequently released in discrete "bunches" at a set time interval.

4.5.1 Advantages of cooled ion beams

The use of a cooler further reduces the effect of Doppler broadening within the beam (following on from the reduction due to the collinear fluorescence spectroscopy technique itself); since the frequency spread, δf, is proportional to the velocity spread, δv, reducing δE reduces the Doppler broadening within the beam, leading to improved

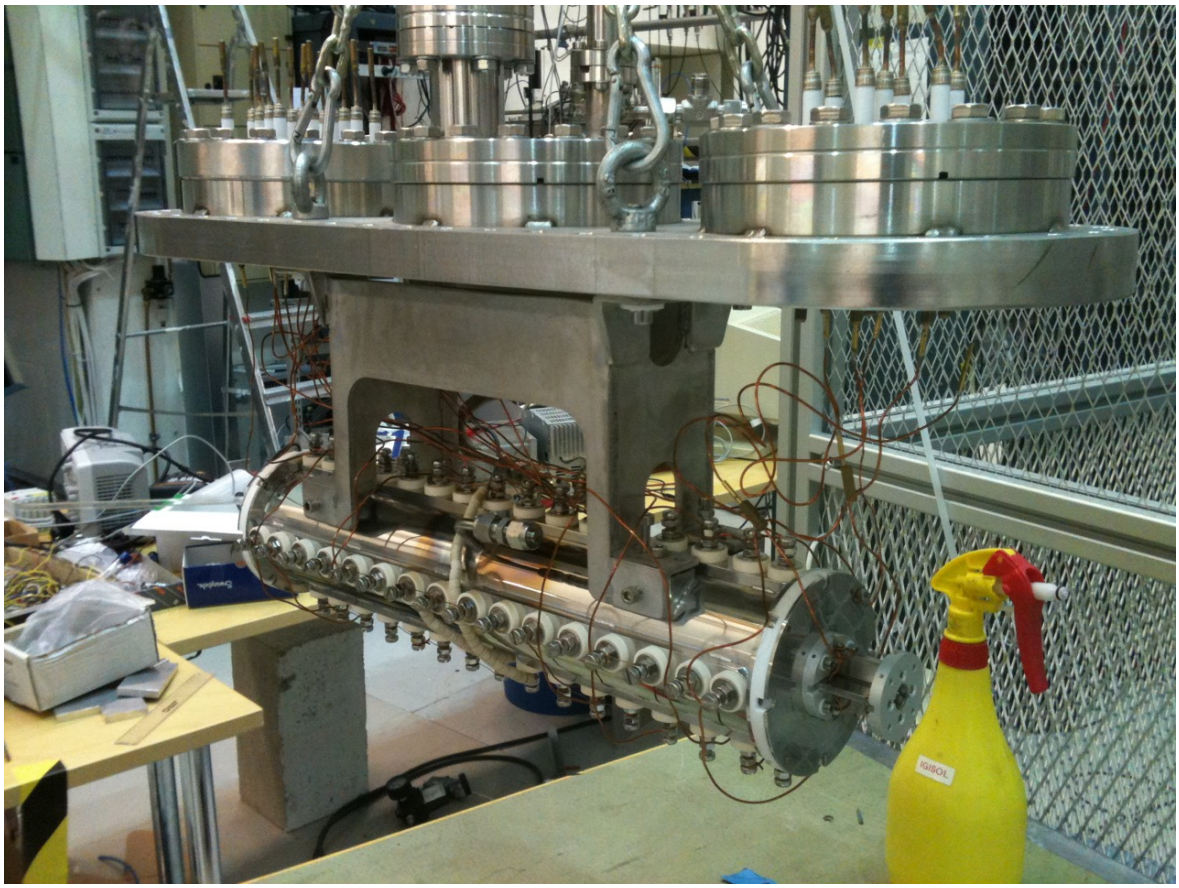

Figure 4.3: The IGISOL RFQ cooler-buncher.

resolution. Another advantage of the cooler is the ability to use a laser beam of narrower width – due to the reduced transverse emittance – which acts to suppress the photon background; i.e. the photon counts occurring due to scattering of laser light inside the photomultiplier tube. A similarly narrow laser beam will require less power to achieve the same power density.

4.5.2 Principle of operation

The cooler consists of four rod electrodes arranged in opposing pairs; applied to each electrode in a pair is a voltage $U \pm V \cos(\omega t)$ [58], where U is the DC potential, V is the RF amplitude (with adjacent rods in anti-phase) and ω is the angular frequency. The cooler itself sits on a high-voltage platform with a potential typically a few hundred volts below that of the ion source. The small potential difference allows the ions to

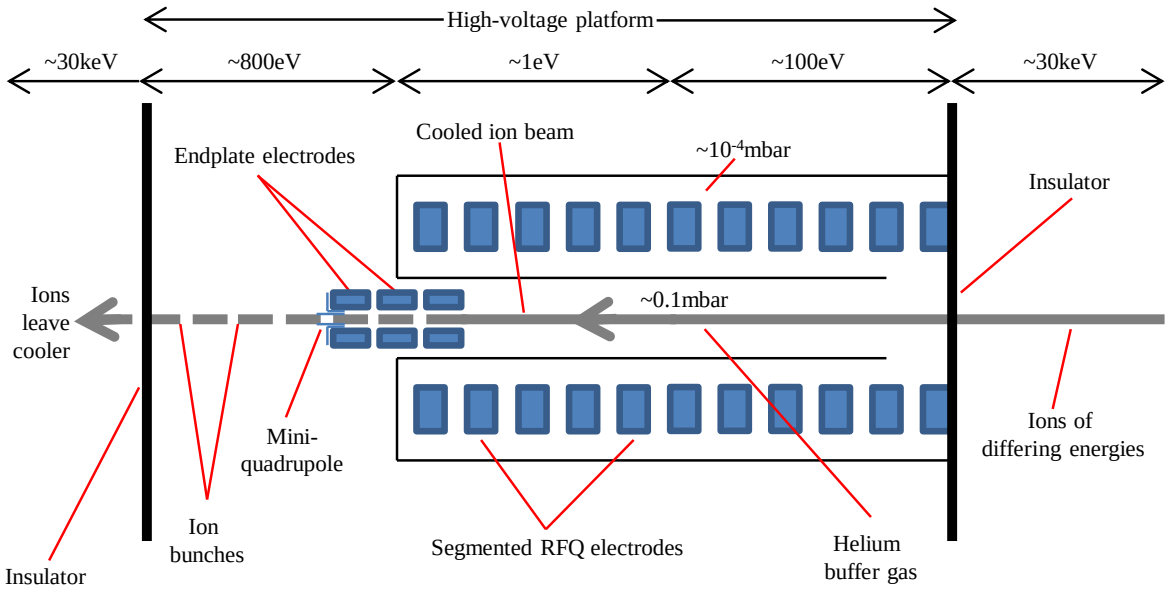

Figure 4.4: Schematic of the RFQ cooler-buncher, showing the segmented rods and the relative ion energies and buffer gas pressures in each region.

pass into a gas cell, filled with helium at a pressure of ∼0.1mbar; at this point, the ions have ∼100eV of energy remaining. The ions collide with the helium molecules, losing a fraction of their kinetic energy as they do so. The applied RF electric field focuses the ions on the central axis. The additional DC electric field is applied via longitudinal segmentation of the rods to provide a gentle field gradient, thus directing the ions to the endplate of the cooler (shown in Figure 4.4). Attached to the endplate is a "mini-quadrupole" through which the ions reaccelerate out of the cooler. The ions exit the cooler with a much smaller energy spread (less than 1eV, compared with between ∼10eV and ∼150eV before entering the cooler) [4, 25]. Figure 4.4 illustrates the cooler-buncher setup and the arrangement of the rod electrodes.

Originally, cooling the ions was intended to be the main factor in reducing the photon background. However, it has since transpired that bunching the cooled ion beam is by far the dominant factor. Ion bunches are formed by applying a potential

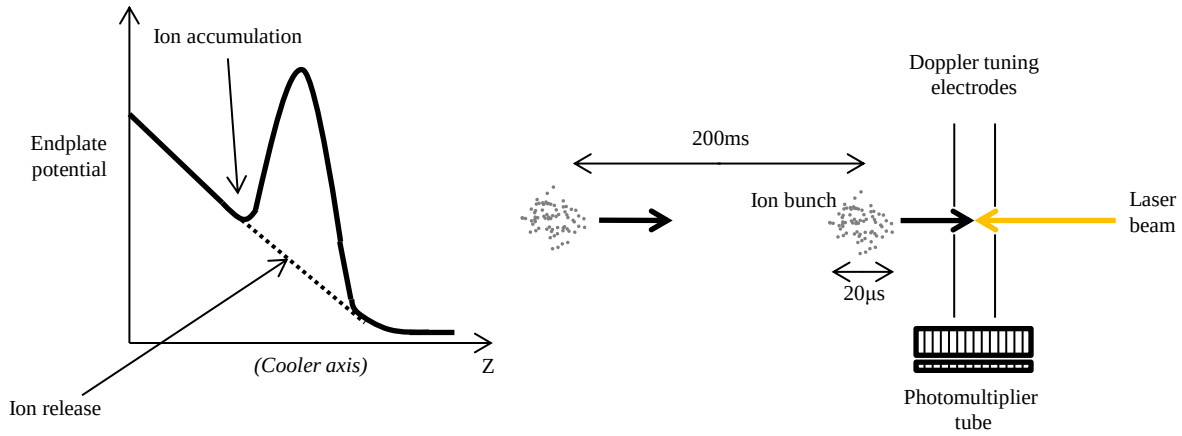

Figure 4.5: Diagram showing how ion beam bunching works. An electronic gate is applied to the detection system so that a photon is only counted if an ion beam is in front of the photomultiplier tube at that time.

to the cooler endplate, so as to accumulate ions inside the cooler, and switching it off at set time intervals to release them. A gate is applied to the detector signal, so that if a photon is detected, it is only accepted if there is an ion bunch in front of the photomultiplier tube at that time. In this way, the photon background from the laser is reduced by the ratio of the bunch accumulation time (∼200ms) to the width of the gate (∼20μs); i.e. background is typically reduced by a factor of ten thousand. Figure 4.5 illustrates how the ions are accumulated and released.

4.5.3 Optical pumping in the cooler-buncher

A more recent development is the use of in-cooler optical pumping, which uses laser light along the axis of the cooler in order to pump electrons into higher excited states, thus increasing the population of the metastable states which, in turn, widens the range of transitions available for spectroscopy. The result is that spectroscopy can now be performed from these metastable states as well as the ground state as shown in Figures 4.6 and 6.2 – as opposed to from the ground state or very low-lying metastable states only, as before. The ability to perform spectroscopy from metastable states is especially advantageous in cases where the transition from the ground state is weak or

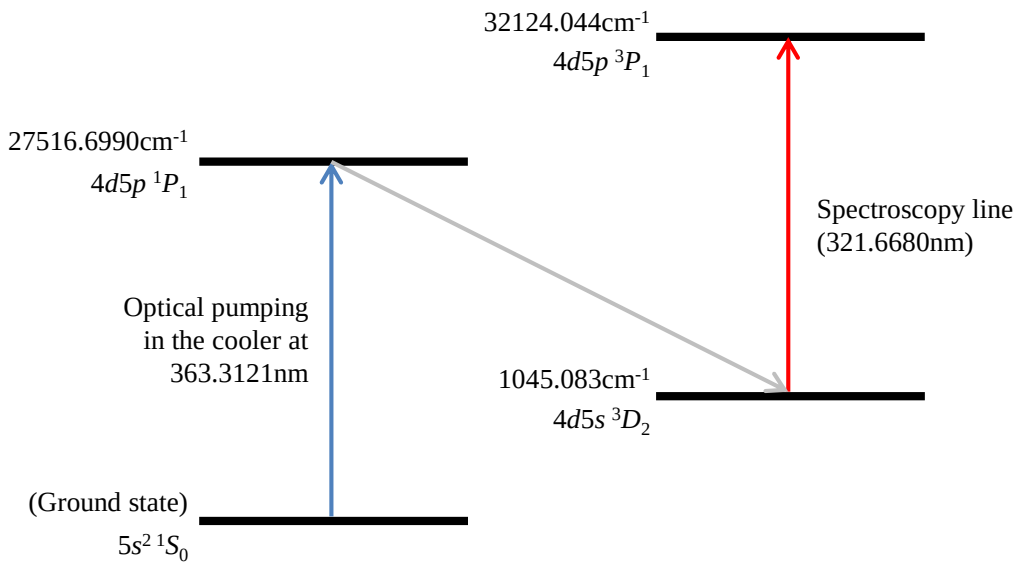

Figure 4.6: Schematic diagram of the optical pumping scheme used for Y^+ in 2007 and 2010 [5, 59], showing how spectroscopy can now be performed from the metastable state in the Y^+ ion, rather than solely from the ground state as without optical pumping.

is a $J = 0 \rightarrow J = 1$ transition. In the latter case, the optical spectrum contains no more than three peaks – meaning that it is not possible to determine the nuclear spin, since fitting three peaks will yield three unknown parameters [7]. One way of solving this problem is to use a transition such as the $J = 2 \rightarrow J = 1$ transition used by Baczynska *et al.* in the determination of the nuclear spin of ^{100m}Y. However, the lower state in this transition is a metastable state with a very low population – and therefore needs to be optically pumped if spectroscopy on this line is to be a viable option.

Since it is only the optical pumping being performed inside the cooler, high-powered pulsed lasers can be used. A titanium-sapphire (TiSa) laser was used for the optical pumping of the Y^{2+} ions. This allows for study on transitions from metastable states – preferable in many cases due to e.g. the strength of the transition, the transition wavelength or the width (in frequency) of the hyperfine structure itself.

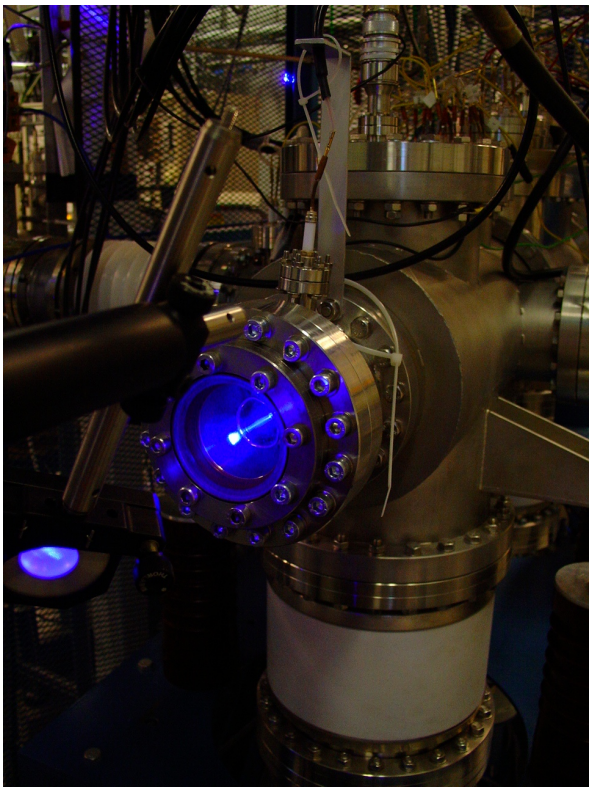

Figure 4.7: The RFQ cooler-buncher whilst optical pumping is taking place.

In-cooler optical pumping was first successfully demonstrated as part of a study of Nb fission fragments at IGISOL [60]. Since then, the technique has become well-established in laser spectroscopic studies, not just at IGISOL but also at ISOLDE [61]. Figure 4.7 shows light from the TiSa laser being shone into the cooler at IGISOL, pumping the ions as they pass through.

4.6 Data acquisition

The data acqusition system (DAQ) at JYFL records and plots photon counts as a function of DAC channel. This is done by applying the tuning voltage across the light collection region, and increasing this tuning voltage in fixed steps per unit dwell time. The voltage is provided by a Cooknell voltage supply [25], and the dwell time is typically of the order of tens or hundreds of milliseconds. Each bin, or "channel" of the histogram therefore contains the number of photon counts within an elapsed dwell time for each voltage "step" – the voltage is scanned across. After the final

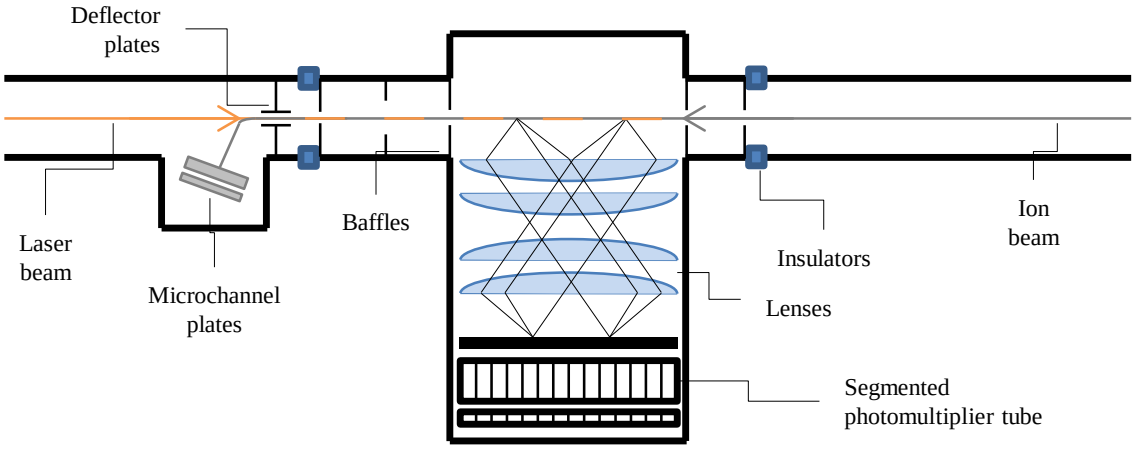

Figure 4.8: Schematic of the light collection region.

bin in the histogram is filled, the tuning voltage is automatically reset to the channel zero voltage ready for the next scan to start. After the scans have been completed, a voltage calibration is performed on the DAC, converting channel number into tuning volts, and the cooler potential is recorded. A digital voltmeter displays the voltages to within ± 0.1V.

4.6.1 The optical detection system

The optical detection setup consists of a photomultiplier tube placed across the laser-ion beam interaction region. A lens system is in place between the interaction region and the photomultiplier tube, so as to focus the emitted photons onto the photomultiplier tube.

Light from the dye laser passes into the light collection region via a Brewster window before interacting head-on with the ions, resulting in their resonant excitation. Photons are emitted from the ions as they de-excite, and focused through a series of lenses onto the photomultiplier tube. Scattering of laser light into the detector is critically suppressed by means of a series of upstream baffles. This therefore helps to reduce the photon background. Figure 4.8 illustrates the layout of the optical detection system, showing how the emitted photons are focused and detected.

4.6.2 Operating the DAQ in bunching mode

When bunching mode is activated on the cooler, the DAQ can also be used in order to "trigger" the release of an ion bunch from the cooler. A time window of $\sim$100μs is set, and sent to the cooler in order to switch off the endplate potential; after this time is up, the potential is reapplied and ions are trapped and re-accumulated again, ready for the next cycle. An additional time gate is applied to the photomultiplier tube; the DAQ sends a start signal to the gate-and-delay generator (GDG) at the start of each dwell time. The delay time is equal to the time-of-flight (TOF) of the ions from the cooler to the light collection region, and the width of the gates is set to approximately the temporal length of the ion bunch [20]. Using the MCP detectors at the end of the laser line, TOF spectra can be recorded and used in order to set the delay times and gate widths. This ensures that a photon will only be counted when an ion bunch is in front of the photomultiplier tube, thus reducing photon background (arising mainly from scattering of laser light into the PMT).

4.6.3 Obtaining hyperfine parameters and isotope shifts

As mentioned previously, the raw plots are of photon counts vs. channel number, with channel-to-volt conversion achieved from the DAC calibration. However, in order to obtain the relevant parameters, it is necessary to plot photon counts against frequency. This is done using a voltage-to-frequency conversion routine, which converts tuning voltages into photon frequencies. Voltages and frequencies are related by

$$\nu = \nu_{\mathrm{L}}(1 + \alpha + \sqrt{2\alpha + \alpha^2}), \tag{4.1}$$

where ν is the *absolute* frequency laser light as seen in the reference frame of the ion, and ν_{L} is the laser frequency in the laboratory frame – both of the order of terahertz – and $\alpha = \frac{QeV}{mc^2}$, where Q is the charge state of the ion, V is the total accelerating voltage (i.e. cooler voltage minus tuning voltage). Thus, the spectrum is now in the format of photon counts vs. frequency, with peaks occurring at hyperfine transition frequencies. However, the frequency differences between each transition are of the order of megahertz – i.e. variations in absolute values of ν are typically only of the order of 0.0001-0.001%. In order to obtain smaller, more meaningful numbers to work with, a

constant reference frequency is subtracted from all values.

Each spectrum is then fitted using a χ^2-minimisation routine, which fits a Lorentzian profile to the data. This allows extraction of individual peak intensities, resolution (in terms of full-width at half maximum, or FWHM, of the peak), hyperfine parameters and centroid of the structure, thus allowing extraction of nuclear moments (directly), and charge radii (indirectly through isotope shifts). The appropriate runfile is loaded in, and starting estimates are set for background, intensities, FWHM, hyperfine parameters and centroid.

The fitting program performs two distinct fits to the data; one with Racah (relative) intensities, the other with free intensities. Often, a scan will only be performed over a section of the structure, leaving some peaks outside the scan region. For the free intensity fit, fitting parameters are assigned to each peak within the scan region, and set to zero (rather than a parameter) for any peak outside.

4.7 Offline testing with stable beams

Before the online experiment begins, it is necessary to test the equipment prior to receiving the beam. To do this, offline tests are performed in which the stable isotopes of the elements under investigation are studied. The ion guide is replaced with an electrical discharge source, also referred to as a spark source, consisting of a sample of the stable isotope of interest. A positive potential is applied to the spark source, triggering a shower of electrons with sufficient energy to ionise the helium atoms. Interactions between the resulting plasma and the spark source lead to the production of stable ions, which are formed into a beam and transported to the laser spectroscopy setup in the same manner as for radioactive ions.

Chapter 5

Proton-neutron pairing correlations in ^{42}Sc

The importance of nuclear mass in both nuclear structure and nuclear astrophysics has led to major developments in nuclear mass measurements – in particular investigations of the relationship between nuclear mass and nuclear size. One remarkable feature which has been consistently verified in experimental data over the past few decades, but is poorly understood from a theoretical perspective, is the odd-even staggering (OES) of nuclear charge radii – across any chain of isotopes, those with odd N are almost always found to have smaller charge radii than their even-N neighbours. A study performed by Bissell *et al.* [62] in 2007, attempted to gain an understanding of the origins of OES by looking at the trends in nuclear moments and charge radii of three multi quasi-particle isomers (i.e. isomers with many unpaired nucleons), namely ^{97m2}Y, ^{176m}Yb and ^{178m1}Hf; this built upon an earlier study by Boos *et al.* [63] in 1994, looking at the same properties of ^{178m2}Hf. The findings of these studies was a decrease in charge radius from the ground state to the isomer; this is despite the isomers seemingly having the higher intrinsic quadrupole moment.

Another pairing case of particular interest is that of proton-neutron pairing. Originally, the pairing term in the Bethe-Weizsäcker SEMF only accounted for like nucleon pairs (i.e. $\pi\pi$ or $\nu\nu$ pairs) [35] – as previously mentioned, the pairing term in equation (2.66) is only non-zero in nuclei with even A. Subsequent to this, however, nucleon-nucleon scattering experiments yielded a surprising result; the nucleon-nucleon interac-

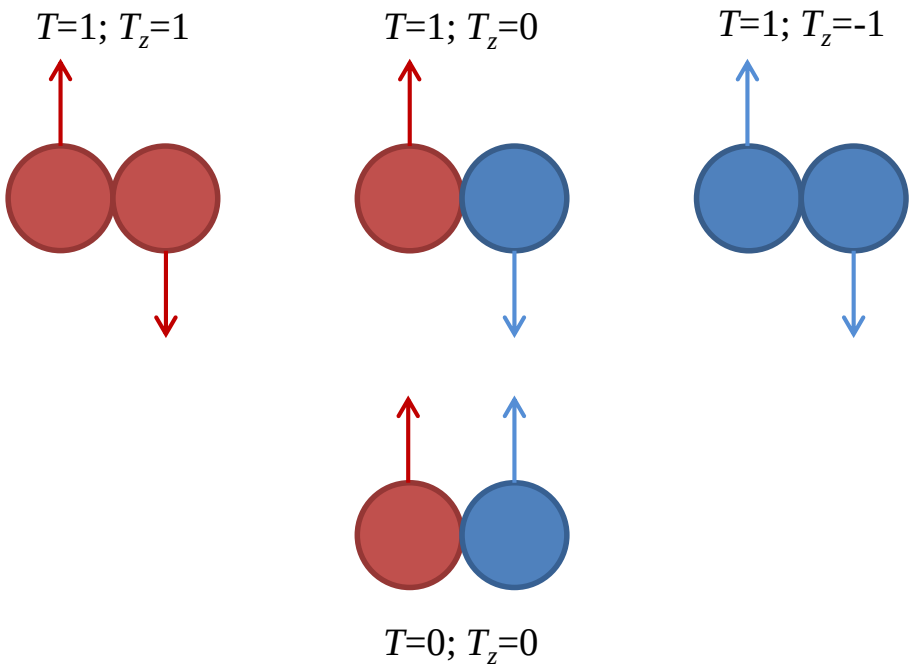

Figure 5.1: Possible pairing arrangements of nucleons – protons are shown in red, neutrons in blue – showing how the different possible two-nucleon systems lead to the $T = 0$ isosinglet and $T = 1$ isotriplet.

tion is found to be, to a good approximation, independent of nuclear charge, meaning that the $\pi\nu$ interaction is equal to the $\pi\pi$ and $\nu\nu$ interactions [64]. Thus, if one assumes independence of nuclear charge and neglects any electromagnetic interaction between nucleons, then the proton and neutron can be considered to be two states of the same particle – the nucleon. This finding is what paved the way for Heisenberg's formulation of isotopic spin, or isospin for short. The coupling of proton and neutron isospins is analogous to the coupling of angular momenta in fine and hyperfine structure, and is therefore given by

$$\vec{T} = \vec{T}_\pi + \vec{T}_\nu; T = |T_\pi - T_\nu|, |T_\pi - T_\nu| + 1, ..., T_\pi + T_\nu - 1, T_\pi + T_\nu. \tag{5.1}$$

Protons and neutrons are both assigned isospins $T = 1/2$, but differ in their third isospin component, $T_3 = \frac{1}{2}(Z - N)$, which, by convention, is taken to be $+1/2$ for protons and $-1/2$ for neutrons. One can see from this that isospin should indeed be *symmetric*.

In the 1950's, Bohr, Mottelson and Pines suggested a "nuclear BCS" pairing mechanism for nucleons – analogous to that of Cooper pairs in superconductors [65]. Pairing correlations between like nucleons – i.e. $\pi\pi$ and $\nu\nu$ pairs – have been instrumental in explaining OES in charge radii and excitation energies [66]. From both this and the aformentioned symmetry in isospin, one would expect the cases for a $\pi\nu$ pair coupled to $T = 0$ (isoscalar) and $T = 1$ (isovector) to be equally important in the case of $\pi\nu$ pairing. Whilst a definite conclusion of the properties of $\pi\nu$ pairs has yet to be reached [66], many studies in this area have yielded results which strongly support the idea of considering $\pi\pi$, $\nu\nu$ and $\pi\nu$ pairs as being equivalent.

5.1 Previous studies of proton-neutron pairing and motivation for studying ^{42}Sc

Not only has the line of $N = Z$ been the subject of much study over the past two decades – especially with regards to validation of the nuclear shell model – but odd-odd self-conjugate ($N = Z$) nuclei also provide an ideal testbed for verifying the $\pi\nu$ pairing correlations described above. In odd-odd self-conjugate nuclei, protons and neutrons occupy the same orbitals. This results in optimal spatial overlap of the proton and neutron orbitals, leading to enhancement in $\pi\nu$ pairing correlations. Two notable $N = Z$ line studies (performed via techniques other than laser spectroscopy) include the decay spectroscopy of ^{82}Nb and ^{86}Tc by Garnsworthy *et al.* [67], and Coulomb excitation of ^{68}Se performed by Obertelli *et al.* [68].

A recent laser spectroscopic study by Bissell *et al.* looked into the $\pi\nu$ pairing correlations in ^{38}K – a neighbour of doubly magic ^{40}Ca ($N = Z = 20$) along the $N = Z$ line, consisting of a ^{40}Ca core coupled to one valence proton hole and one valence neutron hole – by means of collinear laser spectroscopy [69]. It is expected in any odd-odd self-conjugate nucleus that a state with $I = 0$ will have a greater charge radius than a state with $I \neq 0$. This arises due to orbital blocking; an $I = 0$ $\pi\nu$ pair, arising from antiparallel coupling of the proton and neutron spins, can scatter into a range of orbitals; many of these orbitals are excited and therefore less bound, which leads to

a greater spatial extent. Whereas, for a state with $I \neq 0$, there are fewer states a $\pi\nu$ pair can mix with. It is therefore statistically unlikely that such scattering will occur. Present in ^{38}K is a 3^+ ($I = 3$, $T = 0$) ground state and a 0^+ ($I = 0$, $T = 1$) isomer. For ^{38}K, the isomer was found to have a greater charge radius than the ground state – as expected. The investigation of Bissell *et al.* [69] yielded an experimental value of $\delta\langle r^2\rangle^{38g,38m} = +0.100(6)\text{fm}^2$, which was in good agreement with the shell model prediction using the $\pi\nu$ pairing picture. Not only was the 0^+ isomer found to have a greater charge radius than the 3^+ ground state, but this charge radius change was also reproduced well by the shell model, which calculated a value of $\delta\langle r^2\rangle^{38g,38m} = +0.085\text{fm}^2$ [69]. This finding, together with the work of Charlwood *et al.* [70], looking into the properties of the ground and isomeric states in ^{50}Mn, are both consistent with the intuitive $\pi\nu$ pairing picture and point towards the existence of such nucleon-nucleon pairs. In fact, looking at the results for these together with the MQP studies, one should note the apparent proportionality between the magnitude of the reduction in the charge radius and the number of quasi-particles present. Indeed, normal OES can be thought of, in this way, as a single-quasi-particle effect with the same origin.

The motivation for studying ^{42}Sc follows on directly from the work of Bissell *et al.* [69] described above; i.e. further strengthening the case for considering $\pi\pi$, $\nu\nu$ and $\pi\nu$ pairs all on an equal footing along and near the $N = Z$ line. A similar system exists in ^{42}Sc. Clearly, it is of great interest to see if the shell model is able to reproduce the ^{42g,42m}Sc isomer shift as accurately as it appears to have done for those of ^{38g,38m}K [69] and ^{50g,50m}Mn [69, 70]. In contrast to ^{38}K, ^{42}Sc – the other $N = Z$ neighbour of ^{40}Ca – consists of a ^{40}Ca core coupled to one valence proton and one valence neutron [71]. Being the other side of the ^{40}Ca ($N = Z = 20$) shell closures with respect to ^{38}K, an inversion of the isoscalar and isovector states is observed; it is now the ground state ($t_{1/2}$=680.67ms [72]) which has $I = 0$, $T = 1$, whilst there is a long-lived isomer ($t_{1/2}$=61.7s [73]) with $I \neq 0$, $T = 0$ [71]. This isomer beta-decays via a Gamow-Teller transition to the 6^+ (3191keV) state in ^{42}Ca [74]; therefore the allowed spin-parities are 5^+, 6^+ and 7^+ [75]. Both Chiara *et al.* [76] and Scholl *et al.* [75] have reported confident assignments of $I^\pi = 7^+$ for ^{42m}Sc; the ratios of the A and B parameters extracted from this work are in support of this. The contrasting proton and neutron configurations in ^{42}Sc and ^{38}K are illustrated in Figure 5.2. Due to the inversion of the

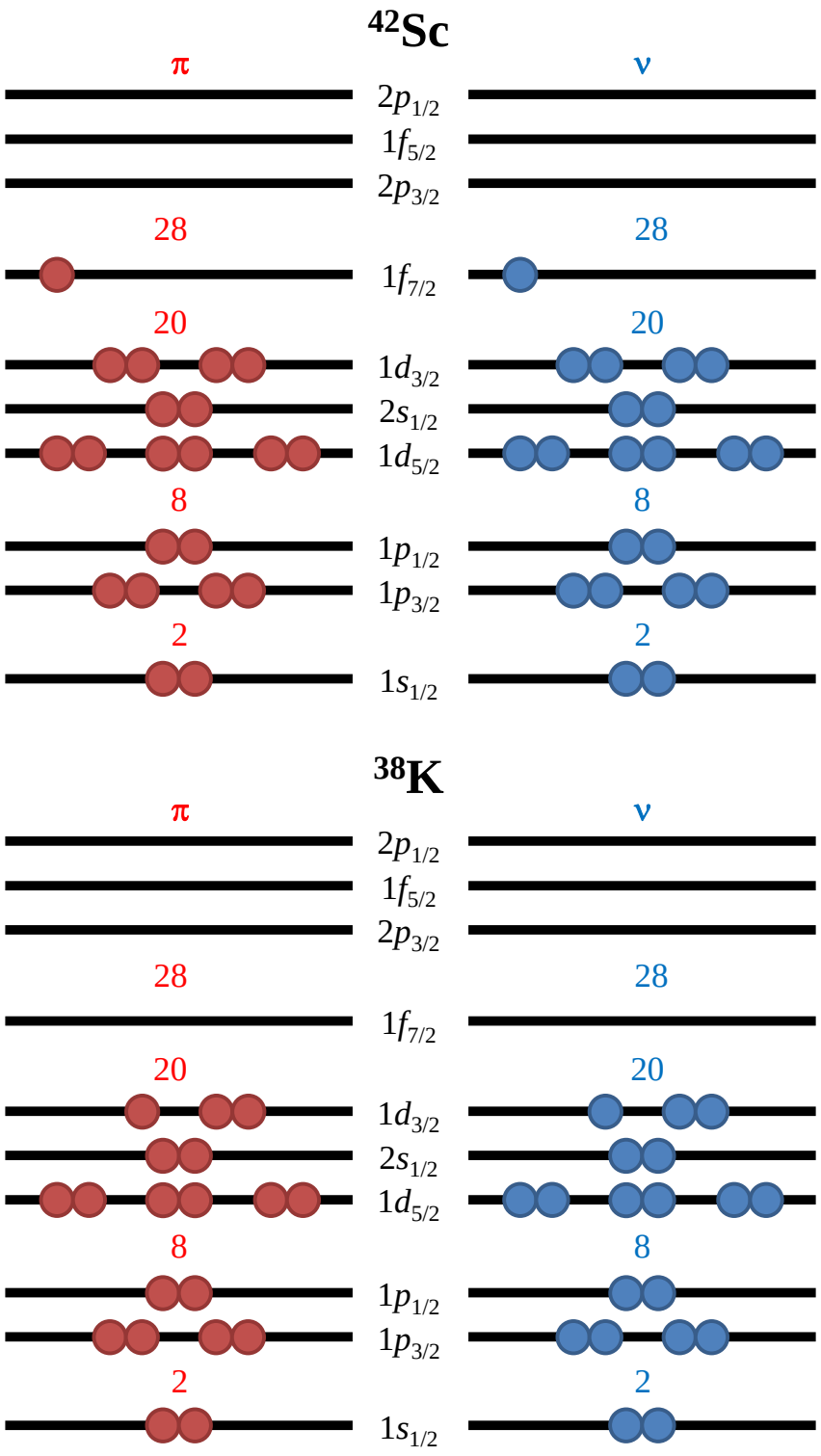

Figure 5.2: Energy level diagrams showing the proton and neutron configurations in ^{42}Sc and ^{38}K.

isoscalar and isovector states as the $N, Z = 20$ shell closures are crossed, it is expected that the ground state in ^{42}Sc will have the larger charge radius – i.e. the opposite to the case for ^{38}K.

Production of ^{42}Sc at IGISOL has taken place twice before. The first time was as part of a Penning trap study of the superallowed beta-decay Q_{EC} value for ^{42}Sc$\rightarrow^{42}$Ca was performed by Eronen *et al.* [45]. In this study, ^{42}Sc ions were produced by impinging a 20MeV ^{3}He beam on a ^{40}Ca target (mostly ^{40}Ca). Incidentally, an analogous Penning trap study was also been performed, again at IGISOL, for ^{38}K [77]. For the first laser spectroscopic measurement of ^{42g}Sc, performed by Avgoulea *et al.* [78] as part of a wider study of the trends in nuclear moments and charge radii along the Sc isotope chain, ^{42}Sc ions were produced via the ^{45}Sc(p, p3n)^{42}Sc reaction, impinging a proton beam of energy between 25MeV and 48MeV on a 2.1mg cm^{-2} ^{45}Sc target [78]. For this work, a ^{40}Ca$(\alpha, pn)^{42}$Sc fusion-evaporation reaction, utilising a 30MeV alpha particle beam, was used for the production of ^{42}Sc ions.

5.2 Offline work and selection of optical transition

For the offline tests, a ^{45}Sc spark discharge source was placed in the IGISOL chamber, in front of the SPIG, and a helium buffer gas pressure of 10mbar was maintained inside the ion guide. The scandium sample was connected to the copper cathode and a spark voltage of ∼500V applied to it. Ions of ^{45}Sc were created from interactions between the resulting plasma and the spark source. The ions were then blown out of the ion guide along with the gas jet, captured by the SPIG and accelerated as an ion beam.

It was decided to use the same 363.1nm $3d4s\ ^3D_2 \rightarrow 3d4p\ ^3F_3$ transition as selected for use in [78], due to its higher spectroscopic efficiency and narrower hyperfine structure – thus requiring less time to scan across it. This transition is from the 67.72cm^{-1} low-lying excited state; being a low-lying state meant a naturally high population. Optical pumping of this state was attempted, but no discernible population enhancement was observed.

In order to determine values for the hyperfine A and B parameters for ^{45g}Sc (cal-

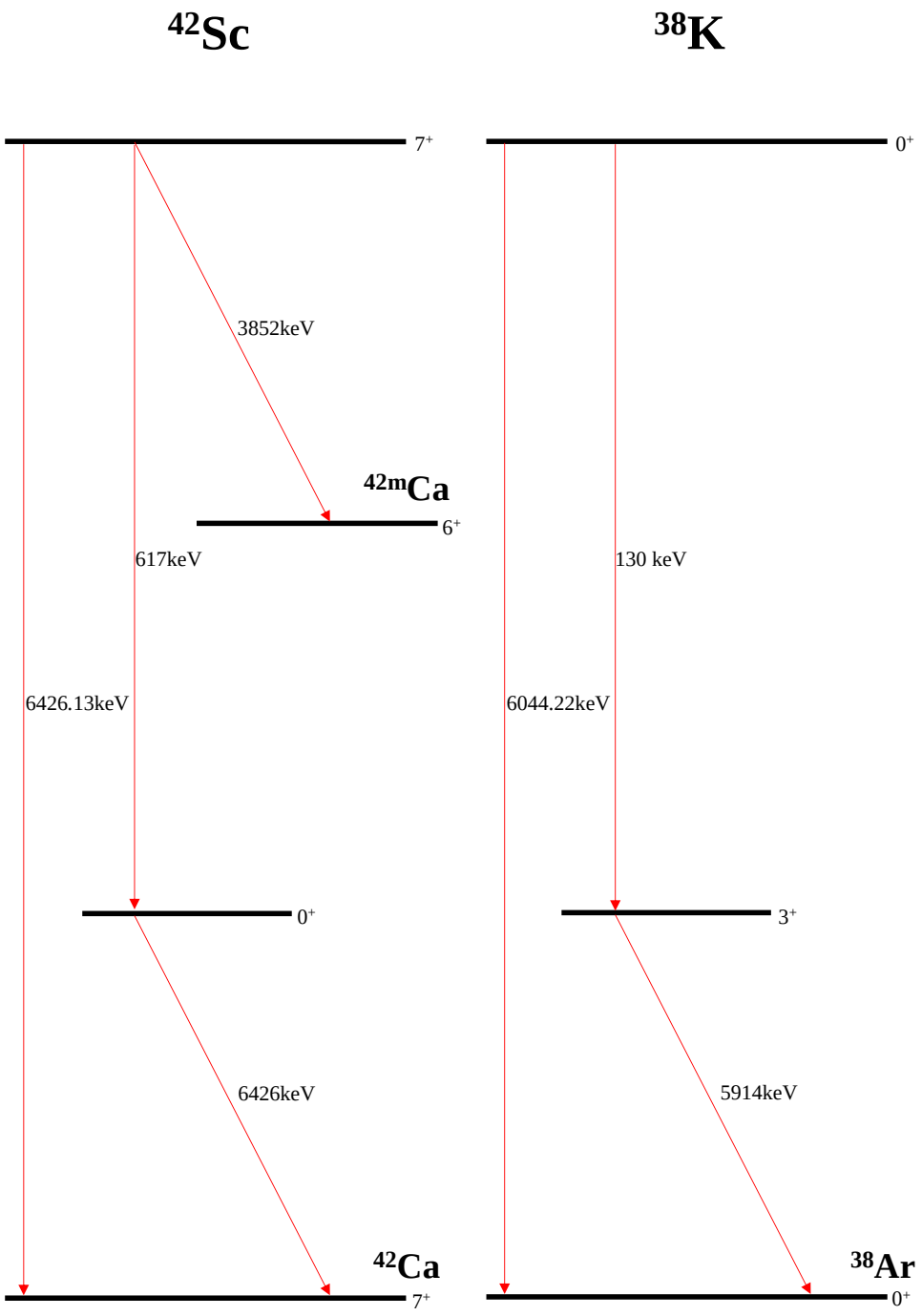

Figure 5.3: Level scheme showing the decays of ^{42g,42m}Sc and ^{38g,38m}K. The spin-parity assignment and excitation energy for ^{42m}Sc are taken from [76], whilst the excitation energy for ^{38m}K is from [77].

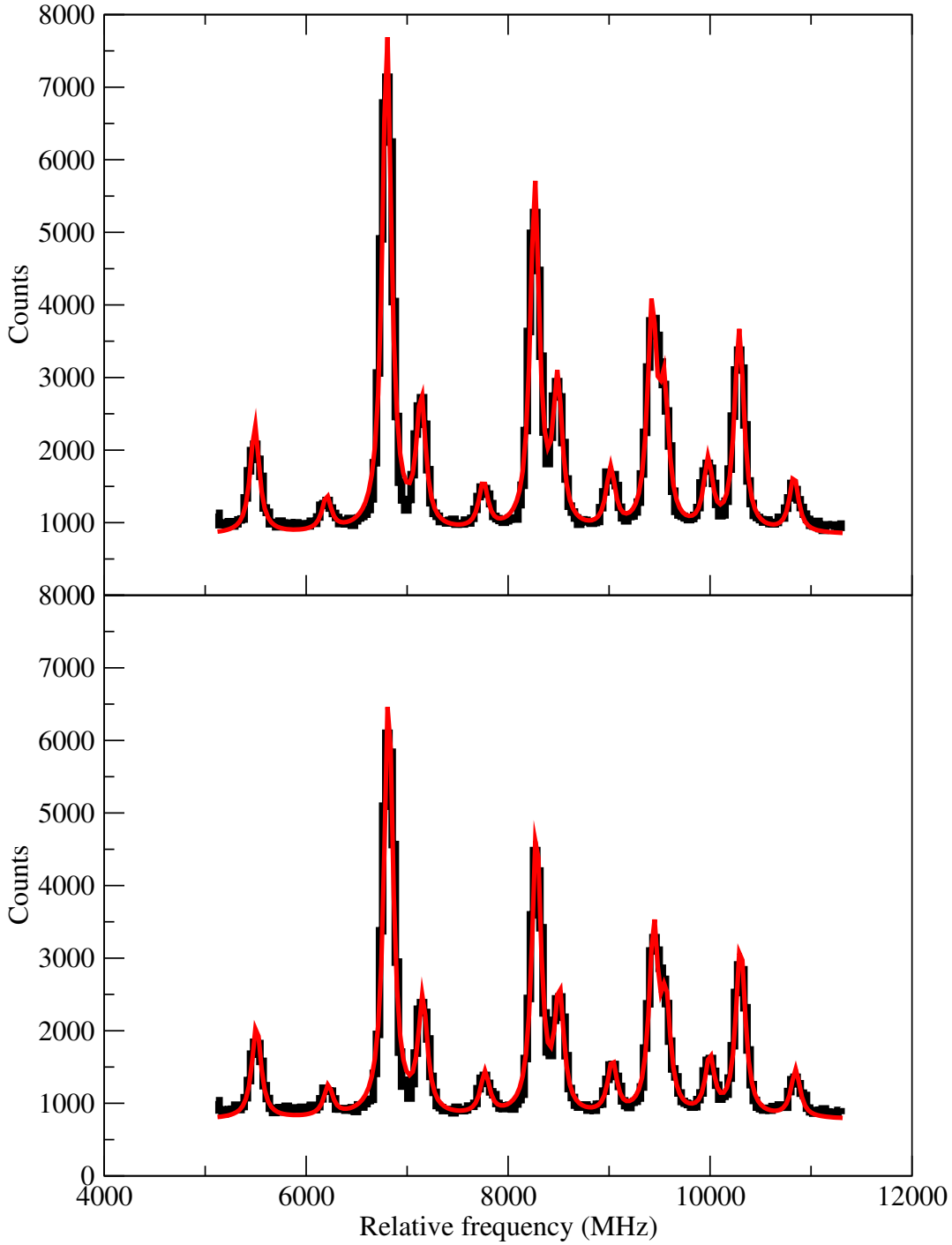

Figure 5.4: Optical spectra of the stable ^{45}Sc isotope, taken during offline testing.

A	A_{u} [MHz]	B_{u} [MHz]	A_{l} [MHz]	B_{l} [MHz]	Reference
45g	+205.8(3)	−67.6(60)	+507.9(5)	−34.7(53)	This work
45g	+205.7(1)	−62.3(19)	+507.9(1)	−34.4(15)	[78]
42m	+82.94(26)	−46(31)	+204.78(64)	−25(17)	This work

Table 5.1: Values of the hyperfine A and B parameters for ^{45g}Sc and ^{42m}Sc from this work, calculated by constraining the lower-to-upper A and B ratios to $A_l/A_u = 2.469$ and $B_l/B_u = 0.552$ (from [78], whose values for the upper and lower A and B parameters are included for comparison).

culated as a consistency check against the values reported by Avgoulea *et al.* [78]), optical spectra were taken for ^{45}Sc, and Lorentzian line profiles were fitted to the data using a χ^2-minimisation routine and a model hyperfine structure in which each peak had a free parameter for the intensity. Centroids were given by equation (2.31). Figure 5.4 shows the fitted ^{45}Sc optical spectra taken as part of the offline tests. Values for the hyperfine A and B parameters obtained from these spectra are shown in Table 5.1, all of which are in agreement (within errors) with those reported by Avgoulea *et al.* [78]. The recalculated B parameters have a lower precision due to the number of scans taken and the absence of a small peak from the hyperfine structure, which lay outside the scan region – a peak exhibiting strong sensitivity to the quadrupole interaction.

5.3 Online experiment and production of ^{42}Sc ions

The ^{42}Sc ions were produced by way of the ^{40}Ca$(\alpha, \mathrm{pn})^{42}$Sc fusion-evaporation reaction, using a 30MeV alpha particle beam and a natural calcium target. The helium pressure in the ion guide was set to 150mbar. The ion guide used for this reaction is shown in Figures 5.5 and 5.6. In order for ^{45}Sc to be produced for frequency reference purposes, a piece of scandium metal was placed at the front end of the SPIG. This has been shown to produce a beam of stable ions for this purpose, in addition to enabling monitoring of the experimental conditions – useful if, for example, the experimental efficiency is seen to deteriorate. The laser was locked to a fundamental frequency of 13750.4482cm^{-1}, and ions were accumulated in the cooler-buncher, being released every 100ms with a period of 20μs.

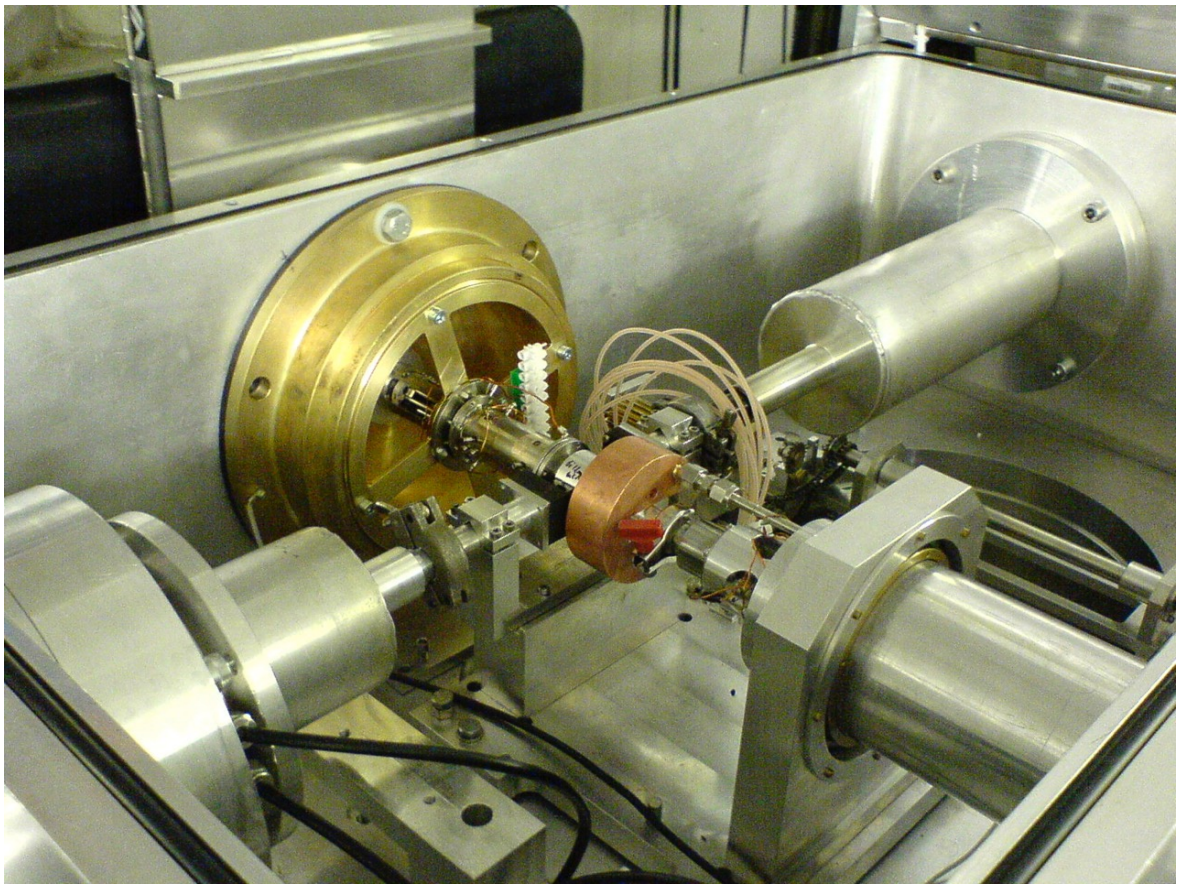

Figure 5.5: Photo showing the IGISOL fusion ion guide – used for the production of ^{42}Sc – in place.

5.4 Analysis of the online Sc data

The first step in the analysis of the data from the online experiment was to find the A and B parameters for ^{42m}Sc (Table 5.1) and the ^{42g,42m}Sc isomer shift (Table 5.2). This was achieved by summing the ^{42}Sc data sets, and fitting a model structure to the summation using a χ^2-minimisation routine in which a free intensity parameter was assigned to each hyperfine resonance peak. The hyperfine parameter ratios A_l/A_u and B_l/B_u were constrained to those of the parameters published by Avgoulea *et al.* [78]; the A and B parameters for ^{42}Sc are shown in Table 5.1. A parallel analysis was also conducted with no constraints on A_l/A_u and B_l/B_u as a comparison. Values obtained for A, B and $\delta\nu$ with free A and B ratios were found not to differ significantly from those using the constrained ratios.

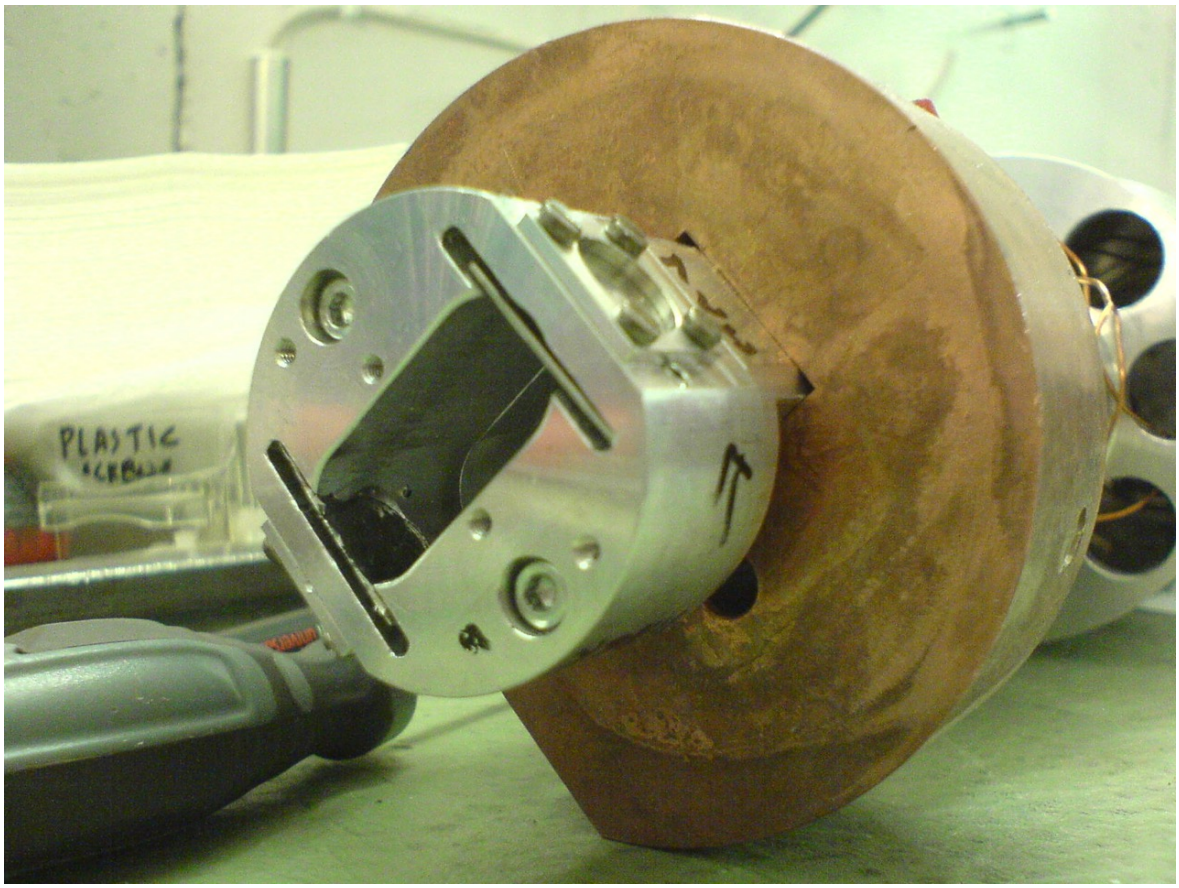

Figure 5.6: Photo showing the IGISOL fusion ion guide whilst out of the chamber. An example of the thin foils of target material used at IGISOL can just be seen mounted in the left-hand slot.

Naturally, the experimental conditions will fluctuate during the course of the experiment; this can lead to drifts in the frequency of the resonances – i.e. the positions of the resonance peaks will be uniformly shifted, typically by a channel or two, and so spectra taken at different times during the experiment will often not be aligned. Thus, drift corrections were required; a drift correction is performed by simply translating the spectrum by however many channels it has drifted by, so that all peaks are correctly aligned ready for summations to take place. The ground-state peaks in two sets of summed ^{42}Sc spectra are illustrated in Figure 5.7, showing how the ground-state peak is shifted by one channel. During the experiment, the intensity of the single ground-state peak was found to be sufficient to provide a frequency reference. This eased the

experimental procedure, as it meant that further scans of ^{45}Sc were not needed – and therefore there was no need to change between masses.

Resonance peaks from both the ground and isomeric states were present in the same scan region over which the ^{42}Sc data sets were taken. Therefore, two separate hyperfine structures had to be added together in the fitting routine – a single peak for ^{42g}Sc, and a hyperfine structure for ^{42m}Sc. Figure 5.8 shows how one of the isomer peaks is directly underneath the ground state peak – this proved problematic for fitting the structure of the isomer, as the fitting routine cannot resolve this isomer peak, leading to instability in the fit. This was rectified by constraining the intensity ratio with respect to the most intense peak of the ^{42m}Sc hyperfine structure using Racah estimates.

In order to find the ^{42g,42m}Sc isomer shift, the frequency conversion was performed twice, so as to account for the 617keV excitation of the isomer – i.e. in the second conversion, a different mass in the kinematic (Doppler) shift was used. This was found to yield a correction of ∼8MHz to the value of the isomer shift. The value of $\delta\nu^{42g,42m}$ was therefore calculated as the difference of the centroids of the single ground state peak and the isomer structure, with the respective masses used; this is shown in Table 5.2.

With the two sets of ^{45}Sc hyperfine parameters – those calculated as part of this work and those of Avgoulea *et al.* [78] – verified to be consistent, and with the hyperfine parameters for ^{42}Sc and the ^{42g,42m}Sc isomer shift determined, a value for the ^{45g,42g}Sc isotope shift was calculated. This was done as a further consistency check against the value reported by Avgoulea *et al.* [78]. This was done using pairs of ^{42}Sc and ^{45}Sc scans which were taken alternately at the start of the run. The difference in centroid between each ^{45g}Sc and ^{42g}Sc spectrum – so as to minimise systematic drifts in the frequency of the resonance peaks – and a weighted mean value was calculated. For this purpose, the individual ^{42}Sc scans were fitted using Racah intensities and A and B parameters constrained to values shown in Table 5.1. In order to obtain a better estimate of the single ^{42g}Sc peak centroid, a ^{42g,42m}Sc "isomer shift", appropriate for the frequency-converted spectrum using the *ground state* mass, was used to put the isomer peaks in their correct *relative* positions. Unlike the spectra taken as part of the

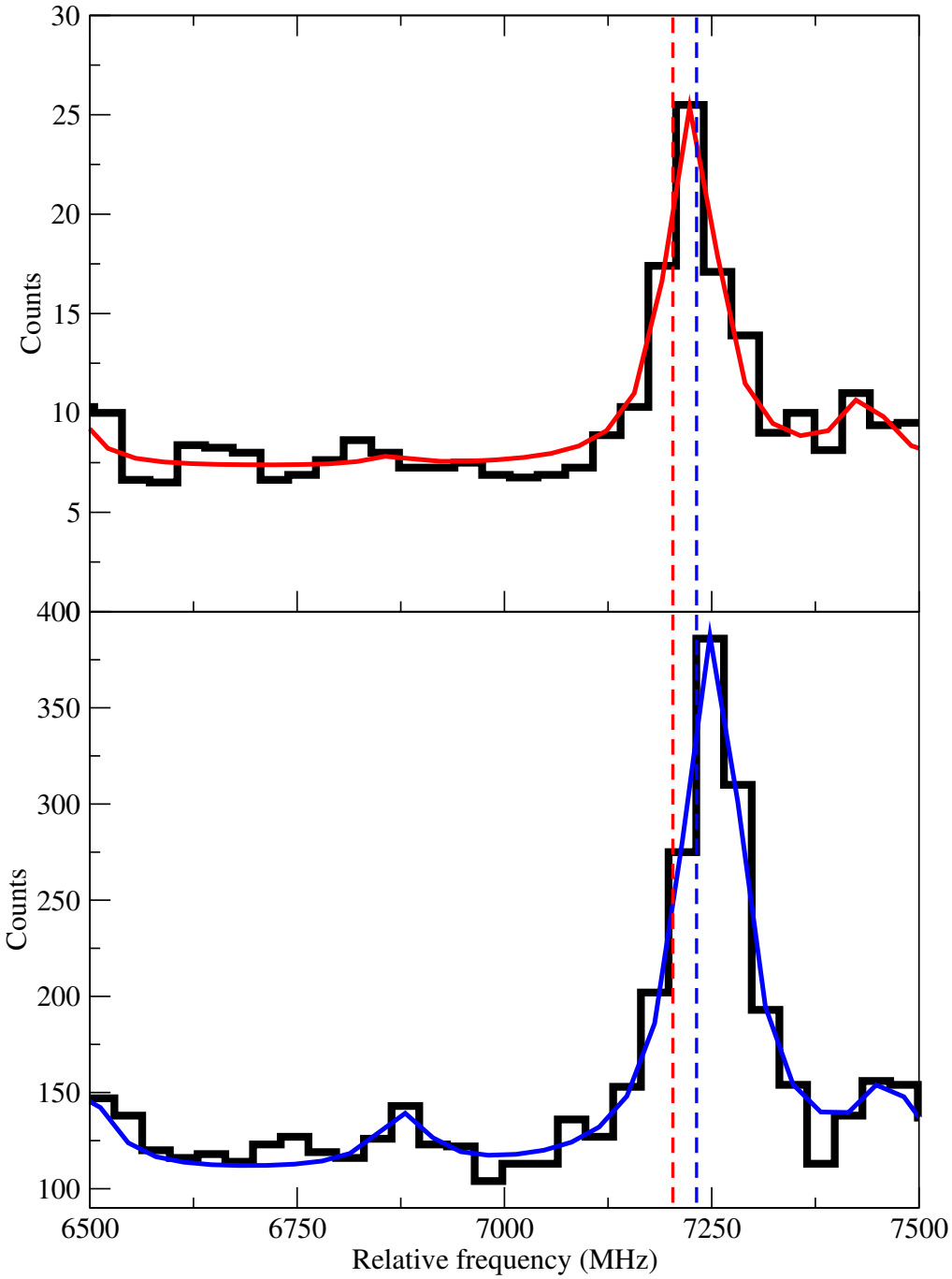

Figure 5.7: The single ground-state peak in two separate ^{42}Sc scans, showing how the peak centroids in each occur in adjacent channels.

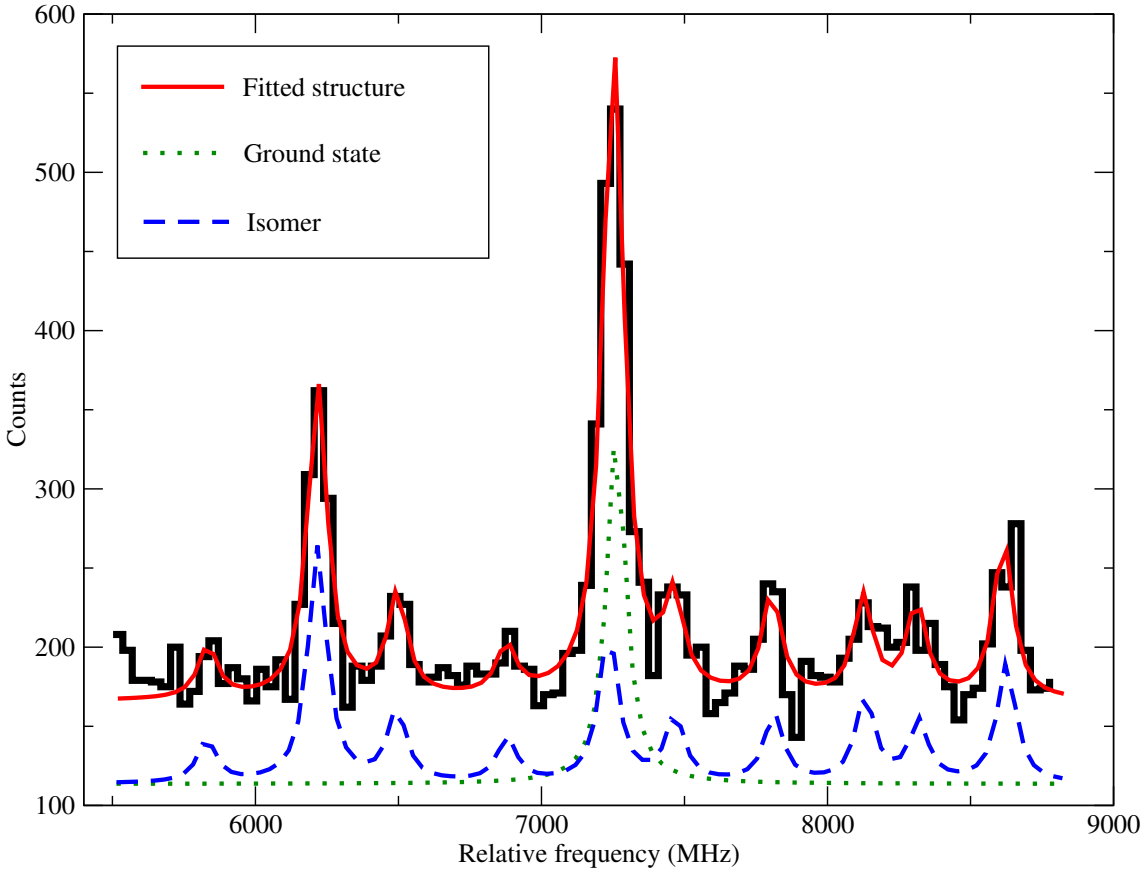

Figure 5.8: Summed optical spectrum of ^{42}Sc. The model structure is shown overlaid, together with the separate contributions from the 0^+ ground and 7^+ isomer, which have been offset for clarity.

offline testing, the ^{45}Sc scans obtained for this purpose were taken over a short scan region, containing only three of the ^{45g}Sc hyperfine peaks. These were fitted using a free intensity fit and the ^{45}Sc hyperfine A and B parameters from Avgoulea *et al.* [78]. In order to find the ^{45g,42m}Sc isotope shift, four ^{45,42}Sc measurement pairs were taken. However, only two of these were used in the calculation of a weighted mean value. This was because optimisation was done in between the ^{42}Sc and ^{45}Sc runs for one pair, and another pair was excluded on the grounds of poor statistics on the ^{42}Sc run. The final value of $\delta\nu^{45g,42g}$ is reported in Table 5.2.

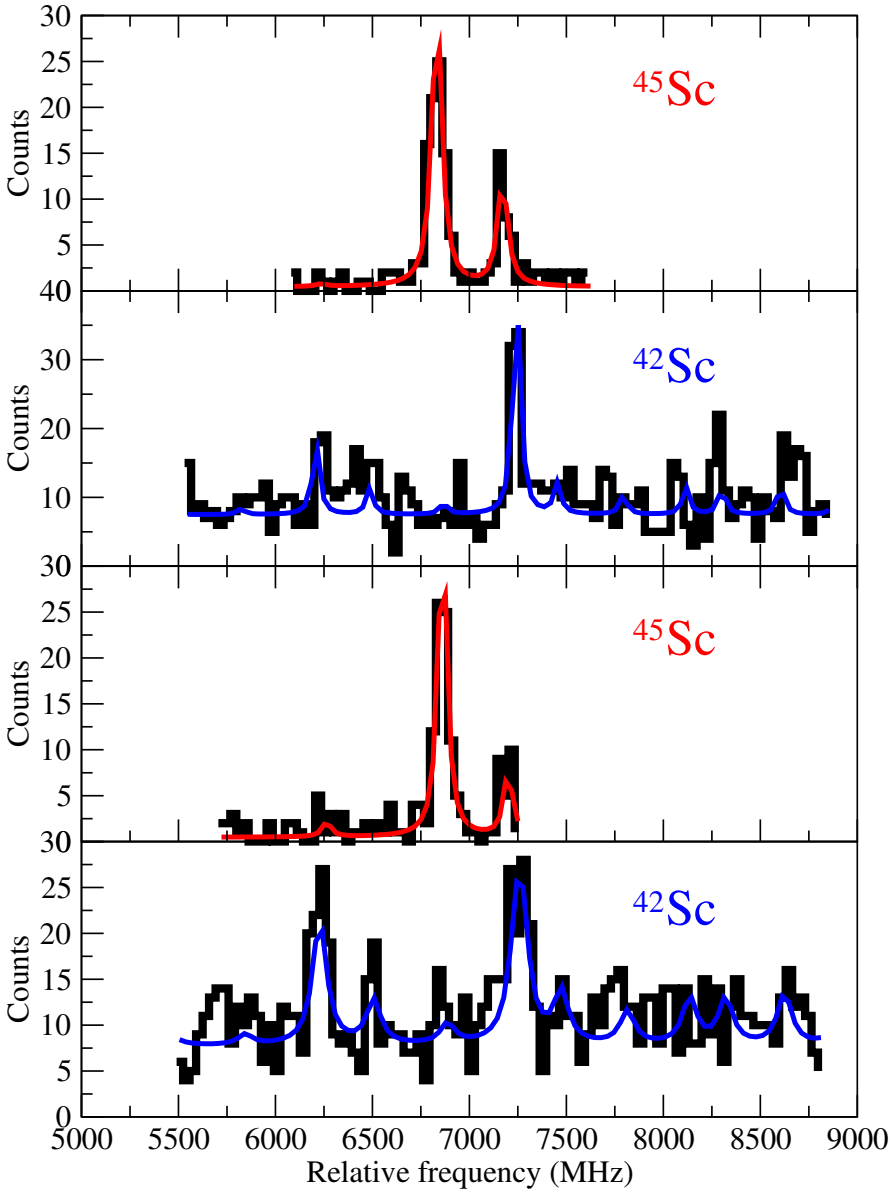

Figure 5.9: Optical spectra of alternating ^{42,45}Sc runs, which were used in order to obtain a value of $\delta\nu^{42g,45g}$ for comparison with results from [78].

A	A'	$\delta\nu^{A,A'}$ [MHz]	Reference
45g	42g	−988(5)	This work
45g	42g	−985(11)	[78]
42g	42m	+76.2(52)	This work

Table 5.2: Values of the ^{45g,42g}Sc isotope shift and the ^{42g,42m}Sc isomer shift obtained from the fitted hyperfine structure centroids.

5.5 Extracting the nuclear moments of ^{42m}Sc

The nuclear moments of ^{42m}Sc were calculated using the very accurate moments for ^{45}Sc from the Table of Moments [79] and equations (2.22) and (2.28). The assignment of $I = 7$ was from the work of Chiara *et al.* [76]; in order to confirm that the 7^+ isomer arises from the parallel coupling of the valence proton and neutron in the $f_{7/2}$ orbital, an empirical estimate of the ^{42m}Sc magnetic moment was calculated using equation (2.23). All nuclear moment calculations are presented in Table 5.3.

Note that ^{42g}Sc is a spin-0 nucleus and therefore has a magnetic moment of zero, whilst there is no sensitivity of the hyperfine structure to the quadrupole deformation (as the aforementioned criterion $I \geq 1$ is not fulfilled). The results reported here are consistent with the spin assignments from Chiara *et al.* [76] and Scholl *et al.* [75]; this can be seen from the ratios of the A and B parameters.

A	I	μ_I [μ_N]	Q_s [b]	Reference
45g	7/2	+4.76(0)	−0.220(1)	This work
42m	7	+3.83(2)	−0.292(200)	This work
		+3.80		Empirical estimate

Table 5.3: Nuclear spins, magnetic dipole moments and spectroscopic electric quadrupole moments for ^{45g}Sc and ^{42m}Sc.

A	A'	$\delta\langle r^2\rangle^{A,A'}$ (fm^2)
45	42	−0.007(16)[1]
42	42m	−0.218(15)[]
45	43	−0.042(14)[4]
45	44	−0.081(11)[8]
44	44m	−0.072(11)[]
45	45	0
45	45m	+0.189(6)[]
45	46	−0.097(9)[10]

Table 5.4: Values of the changes in mean square charge radius of the Sc isotopes recalibrated using new F and M values calculated as part of this work. Random errors are quoted in round parentheses; systematic errors arising from the atomic factor calculations are quoted in square brackets.

5.6 Extraction of the Sc charge radii

The value of $\delta\langle r^2\rangle^{42g,42m}$ was extracted from the value obtained for the ^{42g,42m}Sc isomer shift. Previous calculations of F and M for this transition yielded values of $F = -355(50)$MHz·fm^{-2} and $M = 583(30)$GHz·u [78]. Revised MCDF calculations were performed as part of this work, this time applying the full relativistic recoil Hamiltonian for the mass shift [80]. These gave new values for the atomic factors of $F = -349(15)$MHz·fm^{-2} and $M = 625(60)$GHz·u [81]. For ^{42g,42m}Sc, the mass shift was calculated to be +0.235MHz and is indeed therefore negligible. In addition to determining the charge radii for ^{42g,42m}Sc, the new values of F and M permitted a recalibration of the Sc charge radii previously reported by Avgoulea *et al.* [78]. All new values of $\delta\langle r^2\rangle$ for the Sc isotope chain are compiled in Table 5.4.

The *absolute* radii for the Ar, K, Ca, Sc and Ti isotope chains, complete with the isomeric states in ^{38}K and ^{42}Sc, are illustrated in Figure 5.10. For both ^{38}K and ^{42}Sc, the 0^+ nuclear state does indeed have the greater charge radius, thus strengthening the case for considering $\pi\nu$ pairs on an equal footing to $\pi\pi$ and $\nu\nu$ pairs. The trend in charge radii of the ground states in odd-odd $N = Z$ nuclei between ^{36}Ar and ^{44}Ti, together with the isomer radii for ^{38}K and ^{42}Sc is shown in 5.11. It can be seen that it

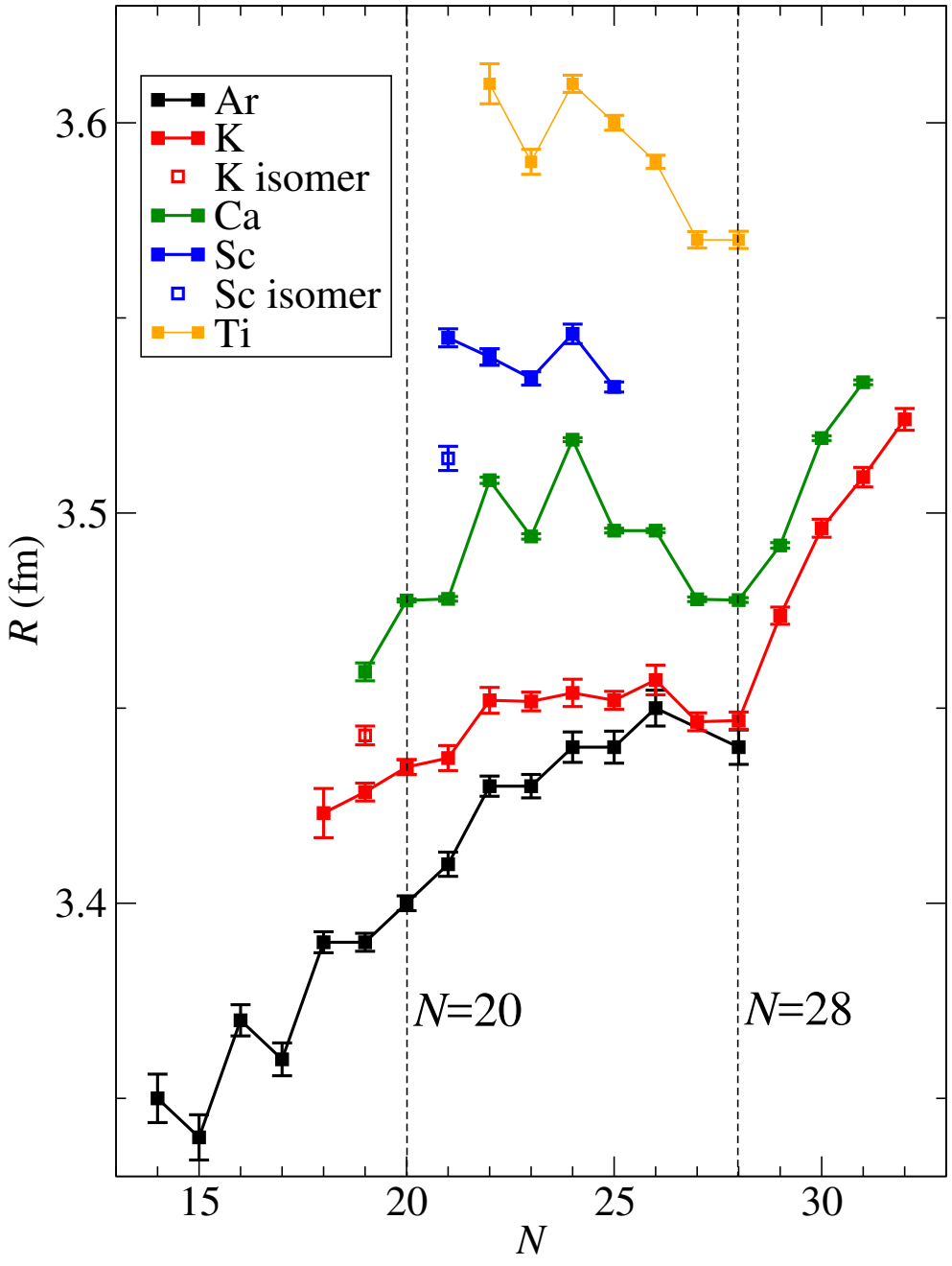

Figure 5.10: Plot of absolute nuclear radii, R, for the Ar, K, Ca, Sc and Ti isotope chains against neutron number, N. All radii for the Sc isotopes other than ^{42}Sc are the values recalibrated as part of this work.

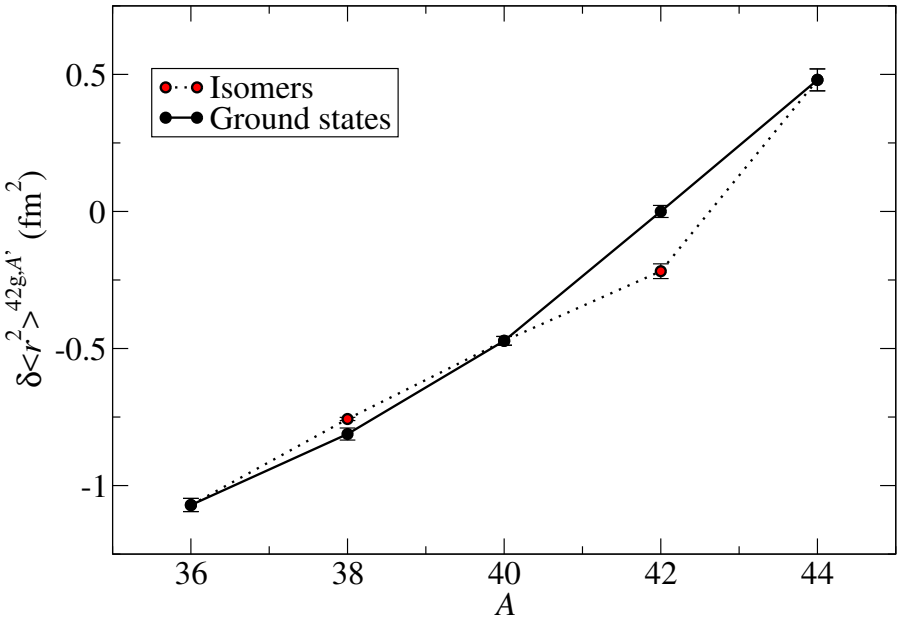

Figure 5.11: Changes in mean-square charge radius of self-conjugate nuclei from ^{36}Ar to ^{44}Ti with respect to ^{42g}Sc, showing clearly the isomeric states in ^{38}K and ^{42}Sc and how the $I = 0$ states in both cases have the greater charge radius. Values for ^{36}Ar, ^{40}Ca and ^{44}Ti are taken from reference [69].

is the $I = 0$ states, of ^{38m}K and ^{42g}Sc, that lie between the even-even neighbours.

5.7 Shell model calculations of ^{42g,m}Sc nuclear moments and charge radii

For comparison with the results determined experimentally, shell model calculations were performed using the shell model code ANTOINE [82] – an m-scheme code whose development stemmed from the earlier efforts of the Glasgow group [83]. Theoretical values of the nuclear moments and charge radii (via the fp proton shell occupancies) of ^{42g,42m}Sc were performed using the ZBM2 effective interaction [84]. Two sets of calculations were performed; one using the original ZBM2 interaction, and one using the version with modified $V^{0,1}_{d_{3/2}d_{3/2}}$ centroids, as per the calculations performed for ^{38}K

(the interaction was modified so as to correctly reproduce the order of the ground and isomeric states in ^{38}K [69]). The ZBM2 interaction, which uses a ^{28}Si ($N, Z = 14$) core, is suitable for calculations of nuclear properties of ^{38}K and ^{42}Sc as it allows for excitations across the $N, Z = 20$ shell closures.

5.7.1 Nuclear moments of ^{42m}Sc

Calculations of the nuclear moments of ^{42m}Sc were also performed, directly from the nuclear wavefunctions generated. These were performed again using both the original and modified versions of the ZBM2 interaction. For the magnetic dipole moment, the g-factors were assumed to be those of free nucleons – i.e. $g_{s(\pi)} = 5.586$, $g_\pi = 1.0$, and $g_{s(\nu)} = -3.826$, $g_\nu = 0.0$. For the electric quadrupole moment, the quadrupole effective charges for the proton (e_π=1.35) and the neutron (e_ν=0.35) were used. The results of these calculations are shown in Table 5.5; it should be noted that the values of the ^{42m}Sc magnetic moment given by the original and modified ZBM2 interactions only differ in the 5$^{\text{th}}$ decimal place. While the experimental error on the quadrupole moment is large, the more precisely determined magnetic moment is reasonably well reproduced by the shell model calculation. This perhaps gives confidence in the calculated wavefunctions.

	μ_I [μ_N]	Q_s [b]
ZBM2	+3.878	−0.165
Modified ZBM2	+3.878	−0.178
Experiment	+3.83(2)	−0.292(200)

Table 5.5: Nuclear magnetic dipole and electric quadrupole moments of ^{42m}Sc calculated in the shell model, together with the experimentally determined values. It can be seen that there is a close match between the theoretical and experimental values of the magnetic moment, which perhaps suggests that the nuclear wavefunctions are correctly understood.

5.7.2 Changes in mean-square charge radii for ^{42g,42m}Sc

The aforementioned general case of the relation between the occupancy of nucleon shells and charge radii needs to be tailored to suit the particular case (nucleon, shell,

	n^{π}_{fp}(42m)	n^{π}_{fp}(42g)	$\delta\langle\ r^2\rangle^{42g,42m}$ [fm^2]
ZBM2	2.76	2.17	−0.114
Modified ZBM2	2.37	1.85	−0.099
Experiment			−0.218(15)

Table 5.6: Occupancies of the ground and isomeric states in ^{42g,42m}Sc, together with charge radius values calculated from these and from the experimental data.

isotope etc.). The change in nuclear charge radius can be related to the change in occupancy of the π fp shell, Δ n^{π}_{fp}, via equation (5.2) [69]

$$\delta\langle r^2_{\pi}\rangle^{A,A'} = \frac{1}{Z}\Delta n^{\pi}_{fp}(A,A')b^2, \tag{5.2}$$

where $b = \sqrt{\frac{\hbar}{m\omega}}$ [85] is the oscillator parameter. This parameter is commonly expressed according to equation (5.3) [86]

$$b^2 = 1.07A^{1/3}\left(1 - \left(\frac{2T}{A}\right)^2\right)e^{3.5/A}, \tag{5.3}$$

where b^2 is in units of fm^2. Use of this equation yields $b^2 = 4.043$fm^2 for ^{42}Sc.

Calculations of the πfp shell occupancies were performed using the ZBM2 interaction (in both its original and modified form), in order to test the validity of this conclusion; the results are shown in Table 5.6. Additionally, previous shell model calculations performed for other Sc isotopes, again using ANTOINE and the ZBM2 interaction [78], could now be checked against the newly recalibrated Sc charge radii. The comparison between experimental and theoretical Sc charge radii is illustrated in Figure 5.12; agreement between experiment and theory is now improved with the new atomic factors. For the specific case of interest, i.e. ^{42g,42m}Sc, although the shell model calculation has the correct sign, in this case it significantly underestimates the reduction in charge radius; the experimental reduction is twice the predicted value.

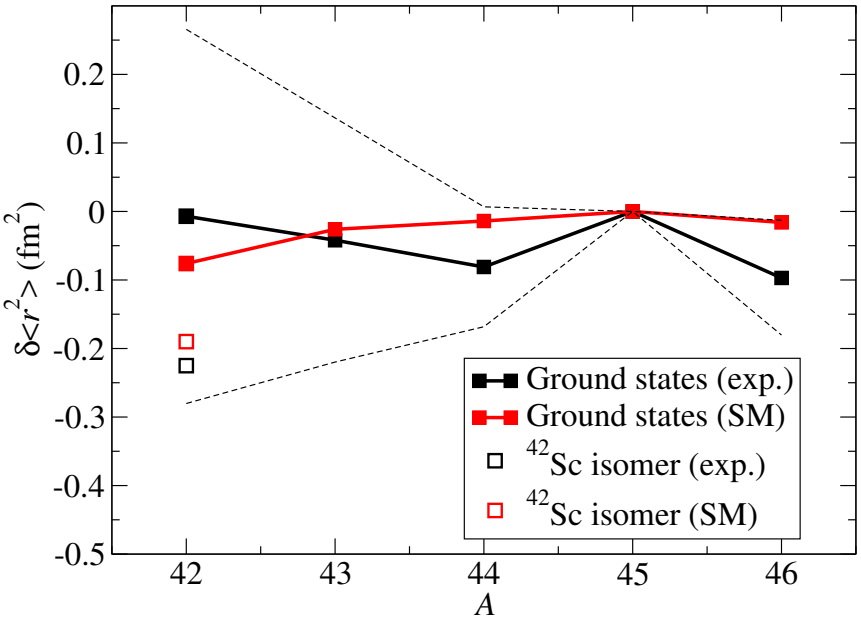

Figure 5.12: Comparison between the new experimental values of $\delta\langle r^2\rangle^{45,A'}$ (calculated using the updated values for F and M), and the theoretical values calculated in the shell model (all from [78], with the exception of that for ^{42g,42m}Sc which is from this work). Systematic errors arising from the atomic factor calculations are included in the form of tolerance bands (black dashed lines). The experimental value of $\delta\langle r^2\rangle^{42g,42m}$ is twice as large as the theoretical value; see text for more information.

5.8 Conclusions and future work

Although a definite conclusion has yet to be reached on whether or not $\pi\nu$ pairing correlations exist, the result for ^{42}Sc obtained in this work, together with the results of previous studies, does *qualitatively* point towards the existence of such behaviour along the $N = Z$ line. As mentioned earlier, there is good agreement between experiment and theory for the charge radii changes calculated for ^{38g,38m}K and ^{50g,50m}Mn. The values calculated for both of these charge radii changes are also strikingly similar, and the shell model also predicts a similar charge radius change for ^{42g,42m}Sc. However, the experimental value of $\delta\langle r^2\rangle^{42g,42m}$ is significantly different from the theoretical value – in fact, the experimental isomer shift is larger by a factor of ∼2. Theoretical efforts

to explain this discrepancy have so far failed, but are ongoing. However, there are a number of factors that have been suggested; it is thought that this discrepancy could be down to one or more of a halo effect, $sd - pf$ mixing and/or breaking of isospin symmetry at the single-particle level [87].

It is hoped that a future study of the ground and isomeric states in ^{26}Al [88] – itself part of a larger study of the charge radius trends across the Al isotope chain – will shed some light on the reasons behind this discrepancy between theoretical and experimental isomer shifts and, perhaps, provide some further insight into whether or not $\pi\nu$ pairings are treated correctly by the shell model. Being the same side of the $N, Z = 20$ shell closures as ^{38}K, one would expect the isomer to have the greater charge radius (there is a 5^+ ground state and a 0^+ isomer present in ^{26}Al). Another possible candidate for such a study would be ^{46}V, which lies on the same side of the $N = 20$, $Z = 20$ as ^{42}Sc; thus, it would be the ground state for which the charge radius is expected to be greater (as in ^{42}Sc, ^{46}V has a 0^+ ground state and a 7^+ isomer). Incidentally, ^{46}V formed part of the previous study involving ^{42}Sc at IGISOL, investigating their superallowed $0^+ \rightarrow\ 0^+$ beta decays [45]. From Figure 5.10, it can be seen that the known Sc charge radii are currently all in the region between the $N = 20$ and $N = 28$ shell closures; another suggestion for future work could be to investigate how the Sc charge radii vary either side of these neutron shell closures.

Chapter 6

Spectroscopy of doubly charged yttrium ions

The sudden onset of nuclear deformation occurring in the $N \approx 60$, $Z \approx 40$ region of the nuclear chart is a well-established but poorly-understood phenomenon. Between $N = 50$ and $N = 59$, nuclei in this region not only become increasingly oblate, but the softness of the deformation also appears to increase linearly. At $N = 60$, however, the picture completely changes, with the nuclear shape suddenly changing from the increasingly soft oblate shape observed in the region $50 \leq N \leq 59$ to a strongly rigid prolate shape. Whilst this is traditionally studied via the electric quadrupole moment, the effect also shows itself up as a sharp increase in nuclear charge radius between $N = 59$ and $N = 60$. Experimental charge radii can be compared with estimates calculated assuming only rigid (i.e. static) deformation in order to study the nature of the nuclear deformation.

6.1 Previous studies in the $N \approx 60$, $Z \approx 40$ region

The first experimental evidence for this onset of nuclear deformation was reported by Cheifetz *et al.* [89], whose decay-spectroscopic study of neutron-rich even-even isotopes of Zr, Mo, Ru and Pd shed light on the rotational-like behaviour for all of these isotope chains in the $A \sim 100$ region. Such results supported the theoretical prediction of Arseniev, Sobiczewski and Soloviev [90]; i.e. that weakly oblate shapes were preferred for $50 \leq N \leq 59$, but a region of more "stable" deformation was to exist aft of

$N \geq\sim 60$. However, the striking feature of the results presented in [89] was how sudden the deformation appeared to change from soft-oblate to rigid-prolate at this point. Further theoretical work, courtesy of Khosa, Tripathi and Sharma [91], investigated the roles of the polarisation of the $Z = 40$ and $N = 50, 56$ cores, and the $0h_{11/2}$ orbital, in the abrupt nature of the shape change in the region around $A = 100$.

Laser spectroscopic measurements of nuclear moments and charge radii in this region were first performed on neutron-rich Rb isotopes by Thibault *et al.* [92], showing how the sudden increase in nuclear charge radius is concurrent with the shape change. The results for neutron-rich Sr reported by Buchinger *et al.* [93] yielded a trend in charge radii strikingly similar to that for Rb. Both of these studies were performed at ISOLDE-CERN, allowing for high radioactive ion yields; however, the higher-A elements in the region are inaccessible at ISOLDE due to their refractory nature. It was for this reason that the study of neutron-rich Zr isotopes by Thayer *et al.* [94] was instead carried out at IGISOL, where production of refractory element beams is possible (see Chapter 4 for details). It was for these same reasons that the original Y study, performed by Cheal *et al.* [5], the subsequent experiments on Nb [60] and Mo [95], and the work on Y reported here, were carried out at IGISOL.

The yttrium isotope chain ($Z = 39$) is of particular interest as it falls in the centre of this region ($37 \leq A \leq 41$; i.e. from Rb to Nb), and is also where the effect is thought to be most prominent, based upon the aforementioned previous studies in the region. Figure 6.1 shows the charge radii for $^{86-102}$Y extracted from optical data taken at IGISOL in 2007 by Cheal *et al.* [5], in which spectroscopy was performed on singly charged yttrium (Y^+) ions on the 363.3nm $5s^2\ ^1S_0 \rightarrow 4d5p\ ^1P_1$ transition, selected for its high spectroscopic efficiency [5]. However, being a $J = 0 \rightarrow J = 1$ transition meant no determination of nuclear spin was possible. However, the nuclear spin of ^{100m}Y was determined by Baczynska *et al.* [59] in a separate study, in which the 321.7nm $4d5s\ ^3D_2 \rightarrow 4d5p\ ^3P_1$ transition was used. This transition, from a metastable state in the Y^+ ion, required optical pumping; the pumping scheme used here is shown in Figure 4.6. Measurements taken on this line also covered ^{89,96,98,99}Y, which had previously been measured on the 363.3nm line; these alone were sufficient to form a King plot. Therefore, the atomic factors – see equation (2.34) – for either

line can be calculated from those of the others, if available.

Since there is only one stable isotope in the Y isotope chain, there have been no existing charge radii data which could have otherwise been used in order to calibrate the atomic factors for the 363.3nm line. It was therefore necessary to form an empirical estimate of the Y charge radii, using data for the charge radii of neighbouring isotones. Information regarding the β-softness of the nuclei under study here is given by how well the experimental charge radii agree with the rigid-body estimates (calculated assuming only static deformation is non-zero). The larger the discrepancy, the softer the deformation. Therefore, any conclusions drawn from the data taken with regards to the softness of the deformation depend on an accurate calibration of the charge radii – i.e. the F and M factors need to be reliably calculated – as this will have a direct effect on the magnitude of any discrepancy between experimental charge radii and rigid-body estimates.

6.2 Motivation for Y^{2+} study

MCDF calculations of F and M were performed for both the 363.3nm and 321.7nm transitions, for comparison with the empirical estimate [30]. This meant that the charge radii for all isotopes could be extracted by converting the MCDF values of $F_{321.7\text{nm}},\ M_{321.7\text{nm}}$ via a King plot. However, it was found that the original values of $F_{363.3\text{nm}},\ M_{363.3\text{nm}}$ [5] and those recalibrated via the King plot of Baczynska *et al.* [59] in fact scattered either side of the empirical estimate, as can be seen from the charge radii shown in Figure 6.1. Therefore, if any reliable recalibration of the charge radii (necessary for quantitative study of the magnitude and nature of the onset of deformation) was to be obtained, further remeasurements of Y isotope shifts are required – preferably using a simple $s \rightarrow p$ atomic transition, for which reliable calculation of F and M is easier to achieve.

However, no $s \rightarrow p$ transitions were found in the Y^+ ion (in which both previously studied transitions occurred). One such transition does, however, occur in the Y^{2+} ion; namely, the 294.6nm $5s\ ^2S_{1/2} \rightarrow 5p\ ^2P_{1/2}$ transition. To date, all collinear laser spectroscopy studies have been performed using either singly charged ions or neutral

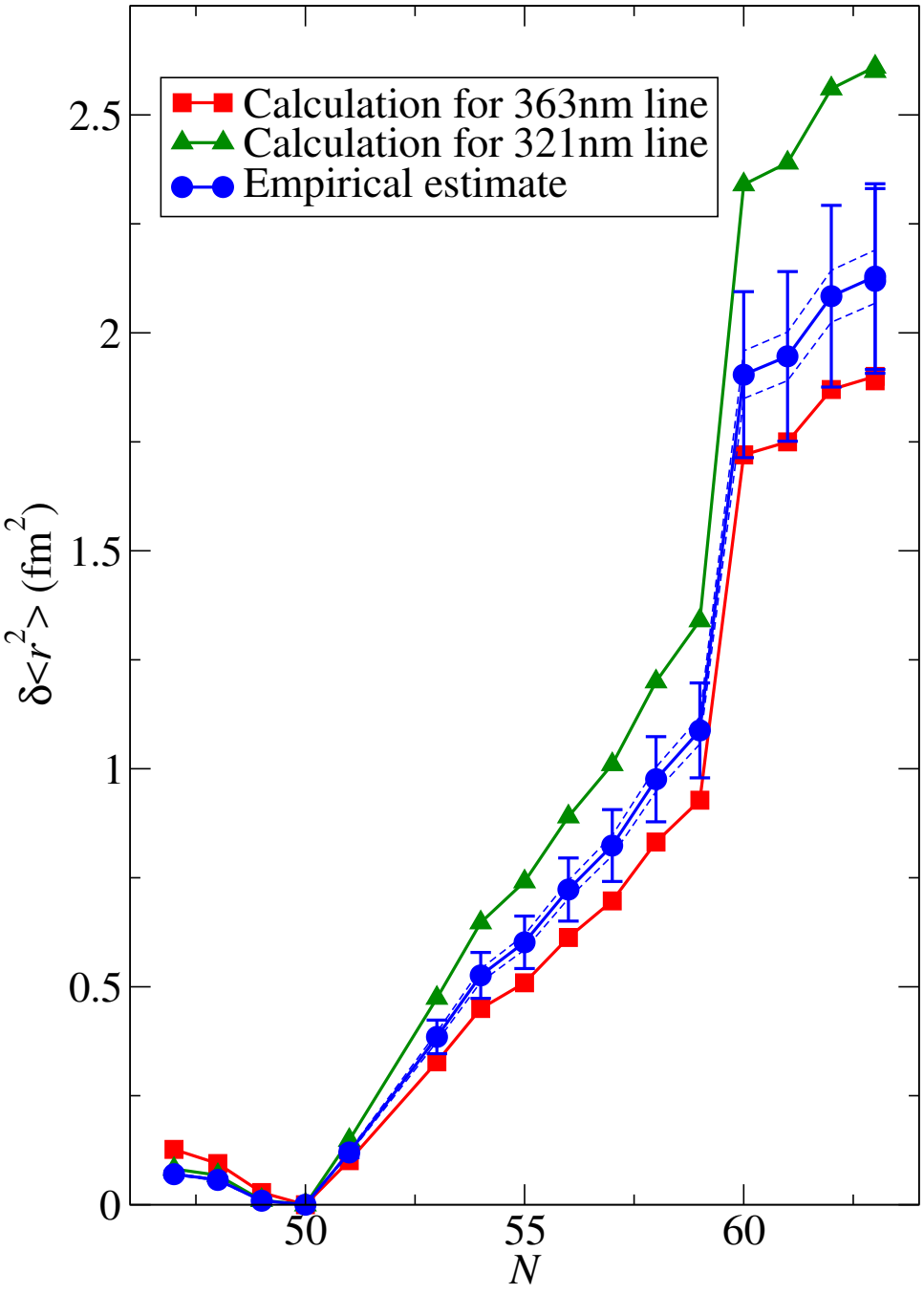

Figure 6.1: Changes in mean-square charge radii for $^{86-102}$Y, estimated empirically and extracted using both the 363nm and 321nm lines. The disagreement between the atomic factors for the 363nm and 321nm lines is clear to see.

	F (MHz fm^{-2})	M (GHz u)
Empirical estimate	−3181(57)	+1789(40)
363.3nm (MCDF)	−3212	+1318
321.7nm (King plot)	−2608	+1812

Table 6.1: Values of F and M for the 363.3nm transition used for the work reported in reference [5]. There are three sets of values; those from the empirical estimate, those calculated via the MCDF method for the 363.3nm line and a third set of values extracted via the King plot technique using isotope shifts measured on the 321.7nm line.

atoms. This was the first ever attempt at collinear laser spectroscopy of doubly charged radioactive ions. Although most radioactive species emerging from IGISOL are singly charged ions, approximately one tenth emerge in the doubly charged state. The major challenge is therefore generating and maintaining sufficient beam currents in order to obtain sufficient statistics, but cases for remeasurement must still be chosen carefully.

The 294.6nm transition is from a metastable state in the Y^{2+} ion, the natural population of which is low. Hence, optical pumping was required; the pumping scheme used here is illustrated in Figure 6.2. As mentioned previously, remeasurement of as few as three or four isotopes (giving, respectively, either two or three isotope shifts) would be required in order to form a King plot with the previous, long chain, data. With more reliable MCDF calculations hopefully possible with this new transition, new values for the charge radii of all Y isotopes measured on the 363.3nm line could then be extracted via the King plot technique.

6.3 Offline testing using stable $^{89}Y^{2+}$ ions

Offline testing was performed using a stable beam of $^{89}Y^{2+}$ ions, produced using an yttrium spark source placed inside the IGISOL chamber. The methodology applied for the production of ^{89}Y ions and the formation of the stable beam was essentially the same as that for ^{45}Sc. A mixture of $^{89}Y^{+}$ and $^{89}Y^{2+}$ ions (∼10% in the doubly-charged state), was produced; the doubly-charged ions were selected by setting the magnetic field of the dipole analyser magnet to that corresponding to $A/Q = 89/2$.

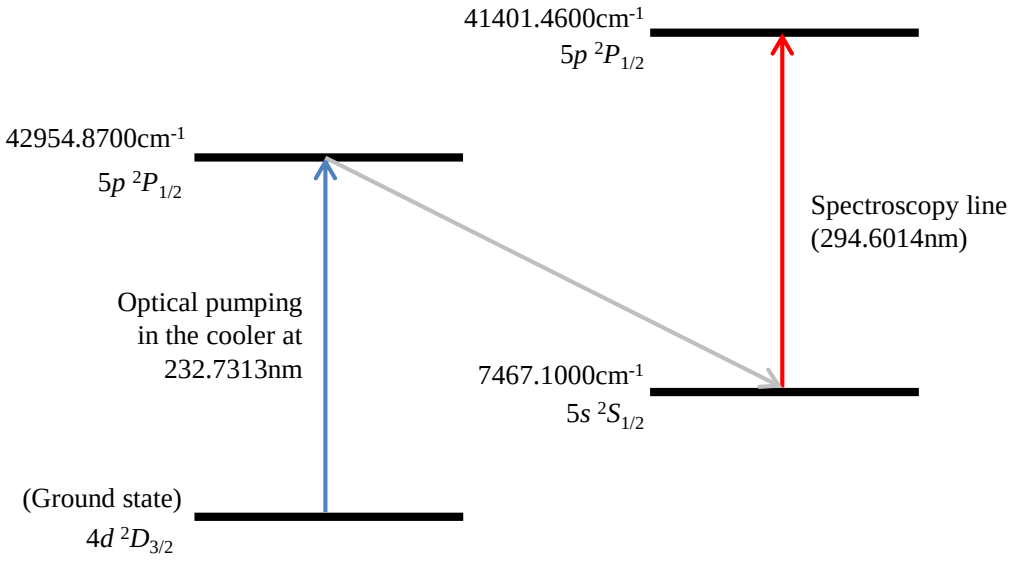

Figure 6.2: Schematic diagram of the optical pumping scheme used for Y^{2+}. The ionic ground state configuration and spin is that reported by Biemont *et al.* [96].

Ion rate (pA)	Efficiency (photon/ion)	A_u	A_l
7.5	$1/8,900$	$-382(6)$	$-1803(6)$

Table 6.2: Results of the fit performed for the offline ^{89}Y data, together with the ion rate and efficiency.

It is worth noting at this point that doubly-charged ions also have a different TOF to singly-charged ions. Once formed into a beam, the ions were cooled and bunched before being overlapped with 1mW of 294.6nm laser light. Optical spectra were taken on the aforementioned 294.6nm transition; the resulting scans were summed and fitted (using Racah intensities) to give the spectrum shown in Figure 6.3. The fit gave values of the hyperfine A parameter and the centroid of the structure for ^{89}Y; these are summarised in Table 6.2. It should be noted that there is no sensitivity to the quadrupole interaction, since the 294.6nm transition is $J = 1/2 \rightarrow J = 1/2$. Therefore, only the hyperfine A parameters will be considered for the work reported on yttrium (all B parameters are undefined).

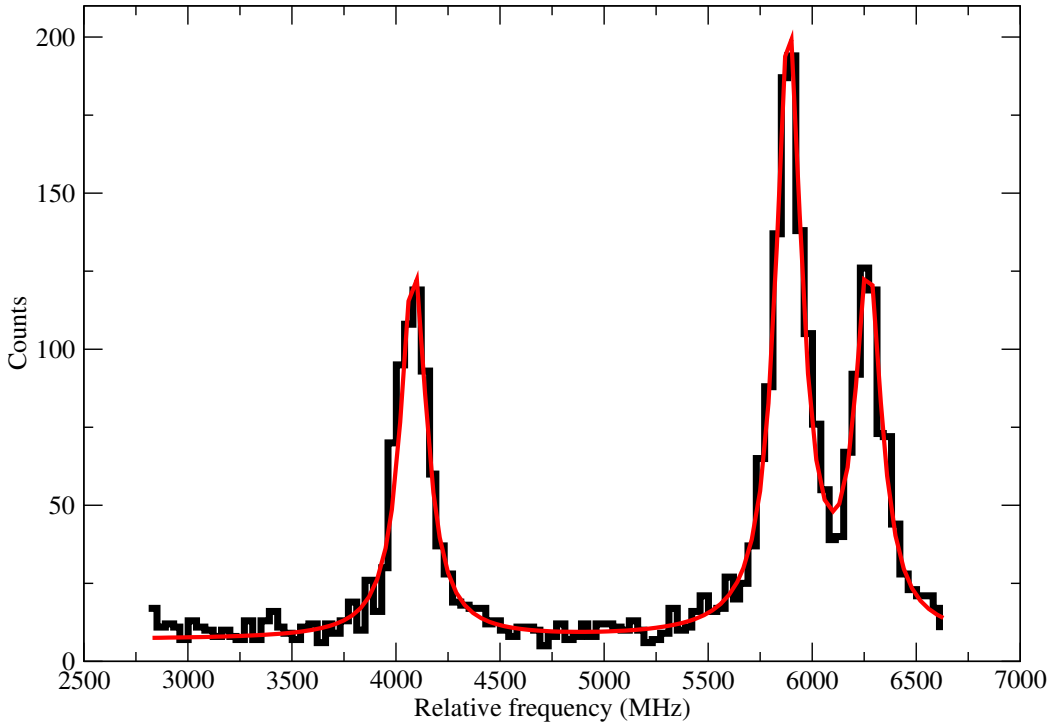

Figure 6.3: Optical spectrum of the stable isotope ^{89}Y, taken during offline testing.

6.4 Estimates of hyperfine splittings and isotope shifts

In an earlier test using the Ge detector, the production of Y^{2+} ions during experiments using fission reactions was also found to be 10% of the Y^{+} yield. Radioisotopes for remeasurement were therefore selected to be those near the peak of production; these were ^{96,97,98,99}Y. It was immediately clear that remeasurement of ^{96,98}Y would be an advantageous choice, as their optical spectra have only a single peak due to having $I = 0$, thus greatly simplifying isotope shift measurements. Hyperfine splittings and peak frequencies were calculated for all previously measured Y isotopes and isomers, using equation (2.22), and the published value of the magnetic moment [79] and fitted A coefficients for ^{89}Y obtained from the offline tests, together with the constrained

ratio of A_l to A_u of $A_l/A_u = 4.83$. Preliminary MCDF calculations were performed for the 294.6nm line; for the atomic factors, these gave $F_{294.6nm} = -1933$MHz·fm^{-2} and $M_{294.6nm} = 853$GHz·u [97]. Theoretical isotope shift values were calculated using these values, working backwards from the empirical charge radii [5], using equation (2.34). All calculations of the hyperfine A_u coefficients and isotope/isomer shifts are reported in Table 6.3.

Two further candidates for remeasurement were ^{97}Y and ^{99}Y. Measurement of ^{97}Y looked like a logical choice, being in between ^{96,98}Y, whereas ^{99}Y occurs after the shape change and is therefore more difficult to locate (in frequency space). Also, as can be seen from Figure 6.4, the hyperfine structure of the 294.6nm line for ^{99}Y is very wide, and would therefore require a large region to scan over – unlike that for ^{97}Y, whose hyperfine structure of the same line is far narrower and would therefore require much less time to study.

6.5 First online experiment and production of radioactive Y^{2+} ions

For the first attempt at spectroscopy of radioactive Y^{2+} ions, it was decided to measure $^{96,97,98}Y^{2+}$. However, it was not possible to produce $^{89}Y^{2+}$ during this run at the time; this meant that there was no frequency reference available. Radioactive Y isotopes were produced via proton-induced fission of uranium at 30MeV (the ion guide used for this reaction is shown in Figure 6.5). Ions were extracted, mass separated, cooled and bunched in exactly the same way as the ^{42}Sc ions, and overlapped with 1mW light from the dye laser. The dye laser was running with Rhodamine-6G dye and locked to a fundamental frequency of 16946.567cm^{-1}. A bunching time of 200ms was used.

6.6 Analysis of the first online Y^{2+} data

For each spectrum taken, the total accelerating voltage was calibrated over the range of channels, and the voltages of each channel converted to relative frequencies. Lorentzian peaks were then fitted to each spectrum using a χ^2-minimisation routine (as per the

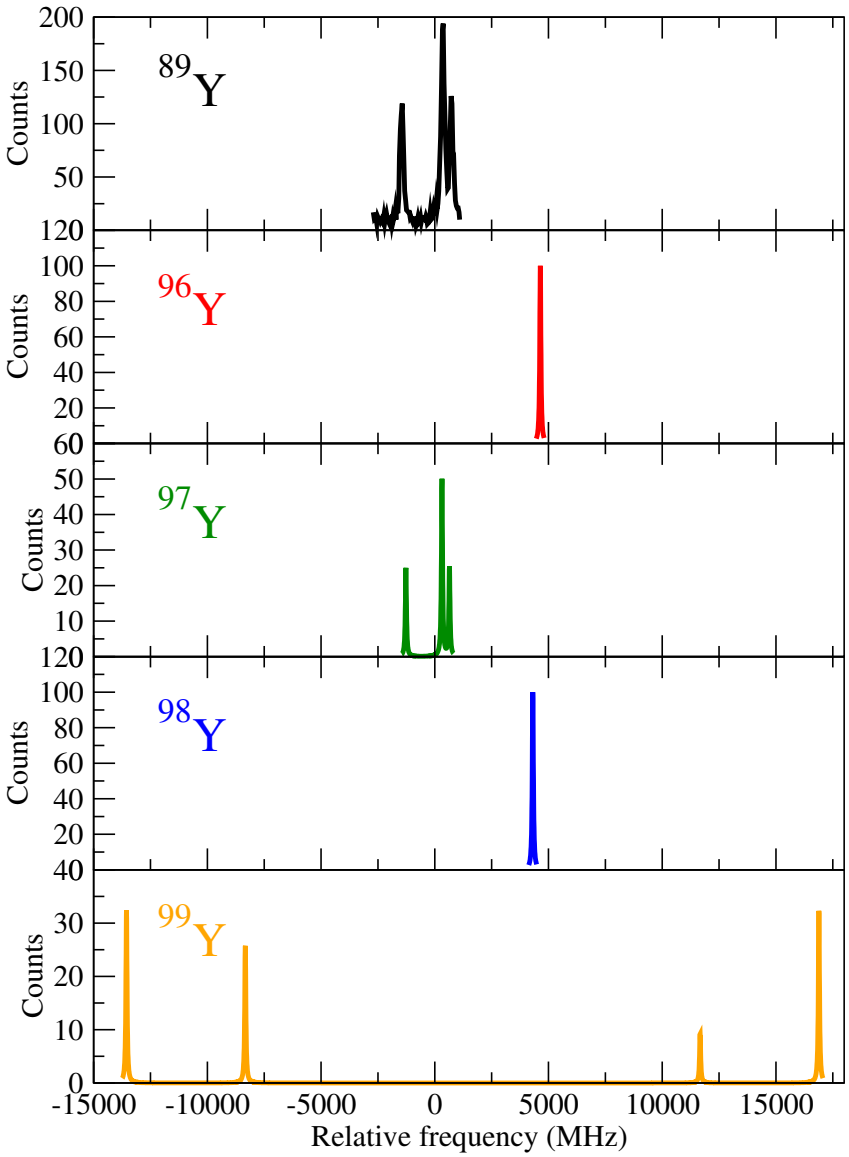

Figure 6.4: Hyperfine structures for ^{96,97,98,99}Y (together with the experimental data for ^{89}Y obtained during offline testing), calculated using the ^{89}Y magnetic moment [79] and fitted A parameters from the offline tests (see Table 6.3).

A	A'	I^{π} (A')	A_{u} (A') (MHz)	$\delta\nu^{A,A'}$ (MHz)
89	89	$1/2^-$	-376.25	0
89	90	2^-	-1122.60	-125.11
90	90m	7^+	$+1032.64$	-79.25
89	92	2^-	-458.62	-430.71
89	93	$1/2^-$	-328.57	-603.31
93	93m	$9/2^+$	$+1837.54$	-123.71
89	94	2^-	-164.28	-652.26
89	95	$1/2^-$	-438.09	-790.33
89	96	0^-	N/A	-891.58
96	96m	8^+	$+1124.31$	-197.17
89	97	$1/2^-$	-328.57	-1093.43
97	97m	$9/2^+$	$+1788.86$	-235.83
97	97m2	$(27/2^-)$	$+571.95$	-46.39
89	98	0^-	N/A	-1219.68
89	99	$5/2^+$	$+1741.40$	-2708.74
89	100	(1)	$+1793.42$	-2675.22
89	100	(2)	$+1492.24$	-2720.76

Table 6.3: Theoretical estimates of the hyperfine (A_{u}) parameters and isotope/isomer shifts for the neutron-rich Y isotopes and isomers, calculated using the estimates of F and M for the 294.6nm transition given in the text and the original charge radii changes from [5]. Unconfirmed spin-parities are quoted in parentheses.

scandium spectra), using Racah intensities throughout. Figure 6.6 shows the fitted ^{96,97,98}Y spectra from the first run. These experimental data yielded a value for the ^{96,98}Y isotope shift of $\delta\nu^{96,98}$=$-$514(10)MHz. Comparing this with the estimate calculated using the preliminary calculations of $F_{294.6\mathrm{nm}}$ and $M_{294.6\mathrm{nm}}$ (see Table 6.4) and the empirical estimate of $\delta\langle r^2\rangle^{96,98}$, a significant discrepancy between the theoretical and experimental isotope shifts is observed. There are two possible suggestions for the occurrence of this; either this reflects that the values previously reported for the Y charge radii are inaccurate, or that the calculations of the atomic factors for the 294.6nm transition (probably M in particular) need to be refined further.

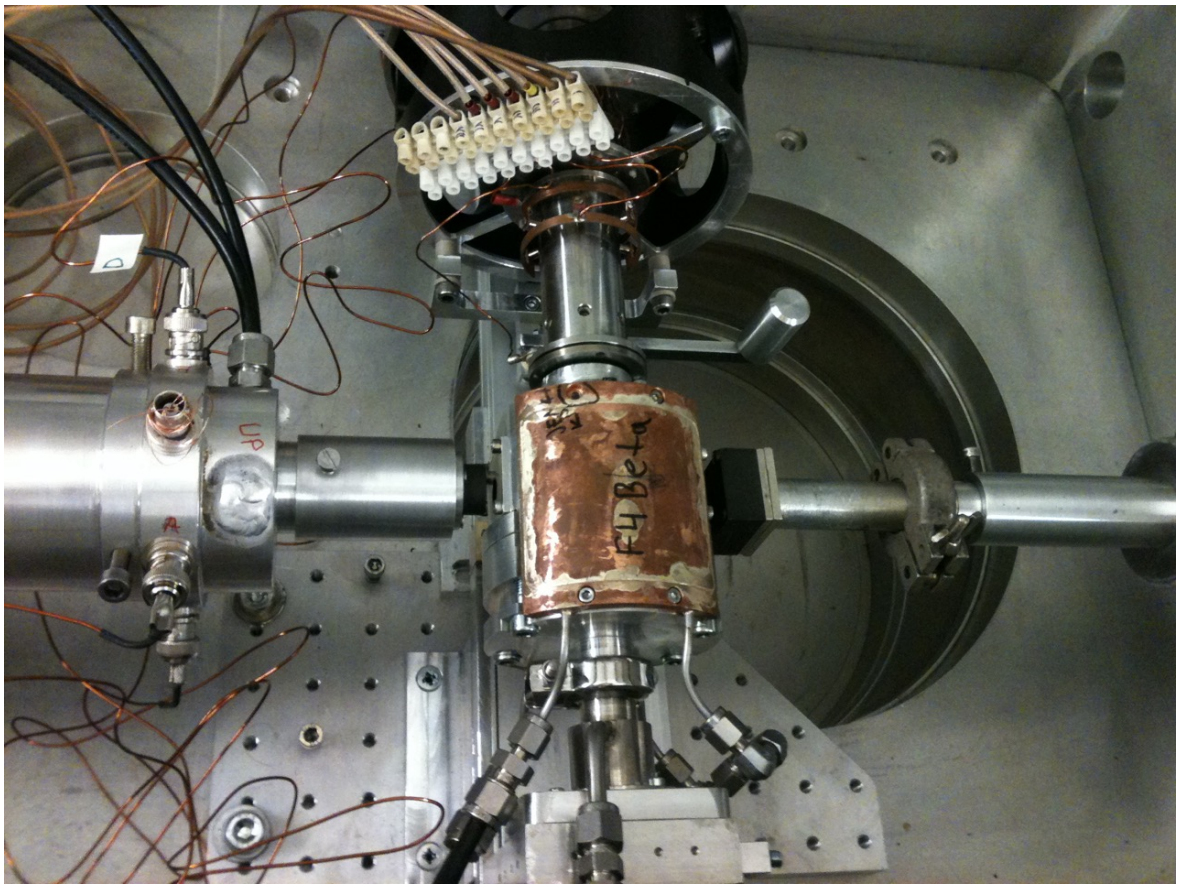

Figure 6.5: Photo showing the IGISOL fission ion guide in place. The exit nozzle (the hole at the top, just after the ion guide) is next to the SPIG.

As for ^{97}Y, poor statistics meant that only the central hyperfine peak was observed, although the fitting routine was still able to return a value for the centroid of the structure since the relative positions of the other peaks (i.e. where they should appear) were constrained. A King plot of the modified isotope shifts for ^{96,97}Y and ^{96,98}Y was constructed (see Figure 6.7); however, the poor statistics for ^{97}Y led to very large errors om the ^{96,97}Y data point. Such large errors, together with the close proximity of the two data points, precluded the construction of a meaningful King plot.

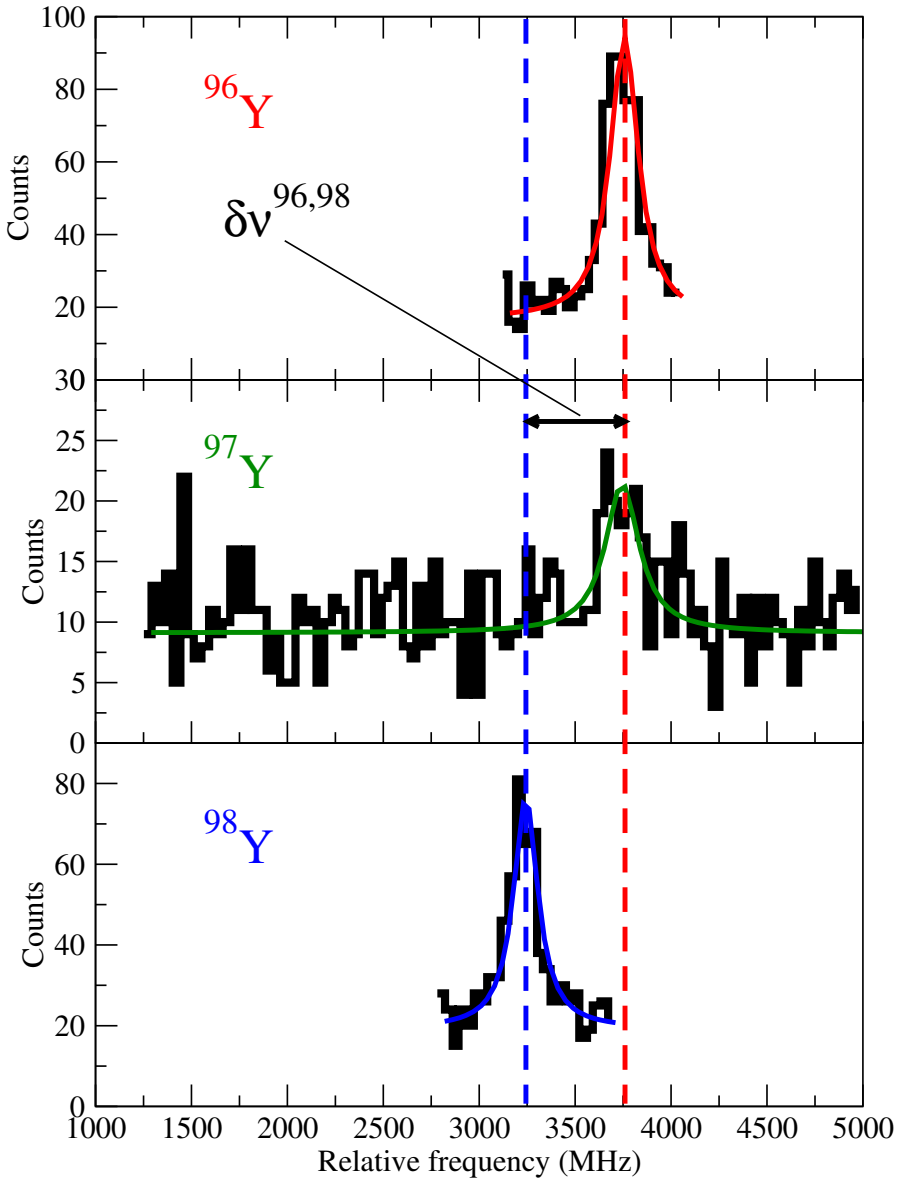

Figure 6.6: Optical spectra of ^{96,97,98}Y taken during the first online run, showing clearly the ^{96,98}Y isotope shift.

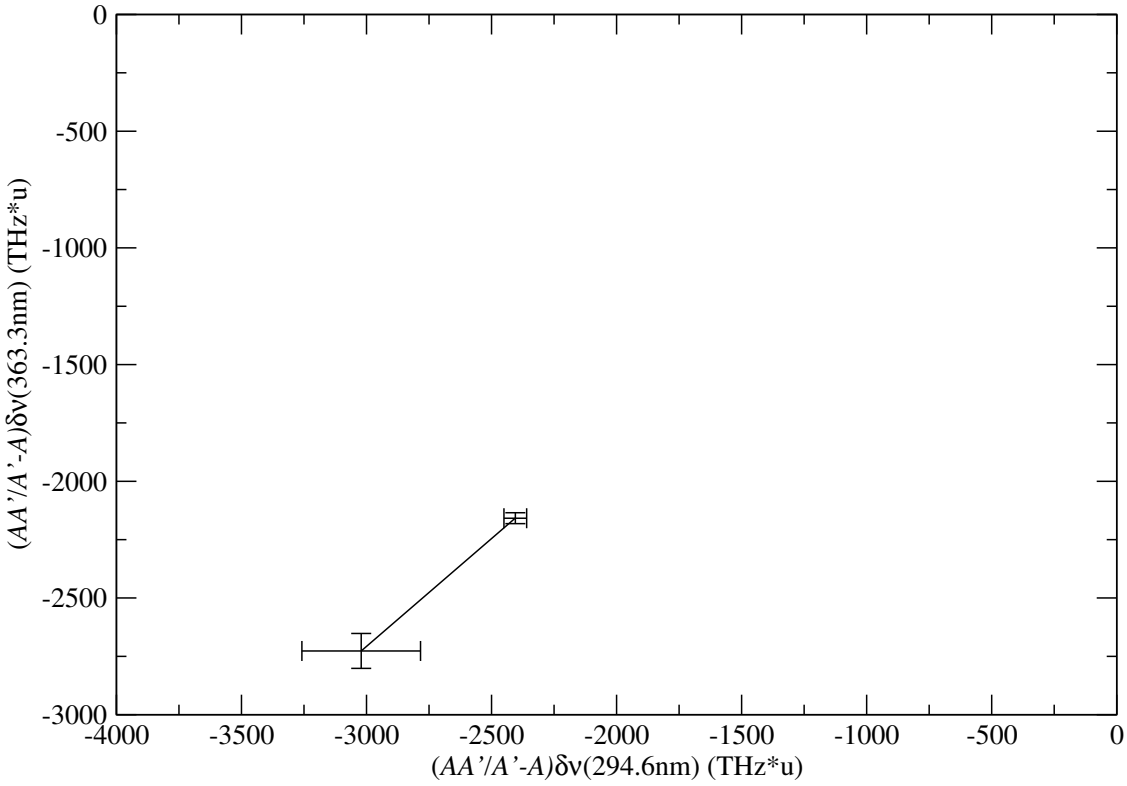

Figure 6.7: King plot of the modified ^{96,97}Y and ^{96,98}Y isotope shifts for the 363.3nm and 294.6nm transitions, constructed using the data from the first online experiment. The large errors precluded a reliable calibration of the Y charge radii solely from these data; hence the need for another online run.

	Theoretical	Experimental
$\delta\nu^{96,98}$ (MHz)	-328	$-514(10)$

Table 6.4: The theoretical estimate of the ^{96,98}Y isotope shift (calculated using the preliminary values of F and M for the 294.6nm transition [97]), together with the value obtained from the first online measurement.

6.7 Second online experiment and future outlook

The issues described in the previous section with regards to ^{97}Y mean that any subsequent experiments would require another data point; one such for ^{89}Y would not only again yield two isotope shifts, but would also give the necessary frequency reference which was unavailable during the first online run. A second step in such an experiment could be to measure the ^{89,99}Y isotope shift. The fact that ^{99}Y occurs after the shape change and has a wide hyperfine structure on the 294.6nm line would mean that the modified ^{89,99}Y isotope shift would produce a calibration point on the King plot lying further out than those for ^{89,96}Y and ^{89,98}Y, which would further reduce the errors on the new values extracted for $F_{363.3\text{nm}}$ and $M_{363.3\text{nm}}$. For the second online experiment, it was decided to measure the hyperfine structures of $^{89,96,98,99}Y^{2+}$ all on the same laser lock (for the reasons described previously). Unfortunately, however, this experiment was unsuccessful due to a multitude of issues. Various apparatus issues coupled with generally low ion yields throughout precluded any data taking using radioactive Y^{2+}. For the production of stable $^{89}Y^{2+}$, two different methods were attempted. The first method tried out was with the yttrium foil placed inside the ion guide. However, low overall ion yields (both for Y^+ and Y^{2+}) suggest that the foil may have had the effect of attenuating the radioactive ions. In an attempt to overcome this, a sample of yttrium was instead on the end of the SPIG (as per the production of ^{45}Sc). However, although this was found to produce an abundance of Y^+ ions ($\sim$30,000 ions per second), no $^{89}Y^{2+}$ ions were produced using this method.

Therefore, a third online experiment is required in order to obtain a reliable recalibration of the Y charge radii. Once again, the plan will be to measure the hyperfine structures of $^{89,96,98,99}Y^{2+}$ all on the same laser lock. Production of stable $^{89}Y^{2+}$ ions will be by means of a new, dedicated, offline ion source for the production of stable isotopes during an online run. This "mini-IGISOL" will be housed on the upper floor of the laboratory (above the main IGISOL ion source; see Figure 4.2), and electrostatic deflectors will be used to accept beam either from the main IGISOL or this new offline ion source. By doing this, it will be possible to produce and study both stable and radioactive isotopes concurrently during an online experiment. Hence, it will be possible to produce $^{89}Y^{2+}$, giving the frequency reference that the first online experiment

lacked. The estimates for the hyperfine structures of the 294.6nm line for ^{96,98,99}Y, together with the offline data already taken for ^{89}Y, will define the size of the scan region to be used and the location of each hyperfine resonance, thus easing the setup process before data can be taken.

Chapter 7

Discussion

This thesis presents the current status of studies into the phenomena observed in two distinct regions of the nuclear chart; the effects of proton-neutron pairing along the line of $N = Z$, and the onset of nuclear deformation in the $N \approx 60$, $Z \approx 40$ region.

The work presented on ^{42g,42m}Sc reported a change in mean-square charge radius $\langle r_c^2 \rangle (^{42m}\text{Sc}) - \langle r_c^2 \rangle (^{42g}\text{Sc}) = -0.218(18)\text{fm}^2$. This result is consistent with the intuitive picture of proton-neutron pairing, in which the $I = 0$, $T = 1$ $\pi\nu$ pair should have a greater spatial extent than the pair making up the $I \neq 0$, $T = 0$ state, and supports the idea of considering $\pi\nu$ pairs on an equal footing to $\pi\pi$ and $\nu\nu$ pairs in nuclei. Additionally, new values of the atomic mass and field shift factors, $F = -349(15)\text{MHz}\cdot\text{fm}^{-2}$ and $M = 625(60)\text{GHz}\cdot\text{u}$, allowed for a recalibration of the charge radii for the other Sc isotopes previously measured on the same atomic transition. All new Sc charge radii have been reported here. The future outlook not just for $\pi\nu$ pairing studies, but also for charge radii of other Sc isotopes, is considered.

This work on Y was the first ever attempt at spectroscopy of radioactive Y^{2+} ions. The motivation for this was a recalibration of the charge radii of $^{86-90,92-102}$Y and isomeric states in $^{87-90,93,96,98}$Y, which were previously measured using Y^+ ions on the 363.3nm $5s^2\ ^1S_0 \rightarrow 4d5p\ ^1P_1$ atomic transition. This was in order to obtain a better measure of the β-softness of the nuclear deformation by comparing the experimental charge radii with droplet-model estimates calculated assuming static-only deformation. The complexity of this transition meant that the charge radii lacked a reliable

calibration due to the difficulty in calculating F and M. Remeasurement on a simpler transition was therefore required in order to recalibrate the values of F and M for the 363.3nm transition, and therefore extract more reliable values for the charge radii. The 294.6nm $5s\ ^2S_{1/2} \rightarrow 5p\ ^2P_{1/2}$ line in the Y^{2+} ion is a simple, alkali-like ($s \rightarrow p$) transition for which the difficulty in calculating F and M was eased. However, the yield of doubly-charged ions from reactions at IGISOL is low ($\sim$10%) and the 294.6nm transition is from a metastable state, thus requiring optical pumping in order to improve spectroscopic efficiency. The advantage was that not all isotopes needed to be remeasured. Calculations of the hyperfine splittings and peak frequencies for all Y isotopes and isomers whose charge radii were previously reported by Cheal *et al.* [5] were performed for the 294.6nm line. This eased the selection of isotopes to remeasure.

For the first online experiment, three isotopes (^{96,97,98}Y) were remeasured. These isotopes were chosen due to being at the peak of production and ^{96,98}Y being spin-0 (and hence their optical spectra having only one peak). The data taken during this experiment gave a value for the ^{96,98}Y isotope shift but no stable ^{89}Y was available; therefore, no frequency reference or third data point for the King plot. Although ^{97}Y was measured, poor statistics (leading to large errors), plus close proximity between the data points for the modified isotope shifts for ^{96,97}Y and ^{96,98}Y, meant a meaningful King plot could not be constructed. A future experiment will see ^{89,96,98}Y all being measured on the same laser lock. This will produce a third calibration point on the King plot. It is hoped that this will yield a reliable calibration of the charge radii for the neutron-rich Y isotopes and isomers. Furthermore, this would allow the spectrum of ^{99}Y to be easily located. As this isotope lies after the shape change, the modified isotope shift would lie far away from the other points on the King plot, reducing the errors still further.

Bibliography

[1] A. A. Michelson, *Light Waves and Their Uses*. Chicago, United States: The University of Chicago Press, 1903.

[2] M. G. Mayer *Phys. Rev.*, vol. 78, pp. 16–21, 1950.

[3] L. J. Curtis, *Atomic Structure and Lifetimes*. Cambridge, United Kingdom: Cambridge University Press, 2003.

[4] H. L. Thayer, *Collinear Laser Spectroscopy of Radioactive Zirconium Isotopes*. PhD thesis, University of Birmingham, 2003.

[5] B. Cheal *et al. Phys. Lett. B*, vol. 645, pp. 133–137, 2007.

[6] P. T. Gallagher, "Magnetic dipole moments." University lecture, 2014.

[7] B. Cheal and K. T. Flanagan *J. Phys. G: Nucl. Part. Phys.*, vol. 37, p. 113101, 2010.

[8] R. Neugart and G. Neyens, *The Euroschool Lectures on Physics with Exotic Beams, Vol. II*. Berlin, Germany: Springer Science and Business Media, 2006.

[9] E. H. Rhoderick *Nature*, vol. 160, pp. 255–256, 1947.

[10] I. I. Rabi *et al. Phys. Rev.*, vol. 55, pp. 526–535, 1939.

[11] R. R. Edelman and S. Warach *N. Engl. J. Med.*, vol. 328, pp. 708–716, 1993.

[12] J. N. Shoolery *Anal. Chem.*, vol. 26, pp. 1400–1403, 1954.

[13] K. Siegbahn, *Alpha-, Beta- and Gamma- Spectroscopy: Volume 1*. Amsterdam, Holland: North-Holland Publishing Company, 1968.

[14] R. Moore *et al. Nucl. Phys. A*, vol. 547, pp. 200–204, 2002.

[15] K. M. Lynch, *Laser Assisted Nuclear Decay Spectroscopy: A New Method for Studying Neutron-Deficient Francium Isotopes*. PhD thesis, University of Manchester, 2014.

[16] T. E. Cocolios *et al. Nucl. Phys. A*, vol. 317, pp. 565–569, 2013.

[17] M. M. Rajabali *et al. Nucl. Instrum. Methods Phys. Res., Sect. A*, vol. 707, pp. 35–39, 2013.

[18] K. Alder and A. Winther *Phys. Rev.*, vol. 96, pp. 237–238, 1954.

[19] L. P. Gaffney *et al. Nature Phys.*, vol. 497, pp. 199–204, 2013.

[20] K. Baczynska, *Extending Collinear Laser Spectroscopy by Optical Pumping*. PhD thesis, University of Birmingham, 2009.

[21] P. Jönsson and C. F. Fischer *Comput. Phys. Commun.*, vol. 100, pp. 81–92, 1997.

[22] W. H. King, *Isotope Shifts in Atomic Spectra*. New York, New York: Springer Science and Business Media, 1984.

[23] G. W. F. Drake, *Springer Handbook of Atomic, Molecular, and Optical Physics*. New York, United States: Springer Science and Business Media, 2006.

[24] M. D. Gardner, *Laser Spectroscopy of Neutron-Rich Yttrium*. PhD thesis, University of Birmingham, 2006.

[25] F. C. Charlwood, *Ground state properties of Mn and Mo using laser spectroscopic methods*. PhD thesis, University of Manchester, 2010.

[26] R. Weiner *Il Nuovo Cimento*, vol. 4, pp. 1587–1589, 1956.

[27] A. C. Melissinos and S. P. Davis *Phys. Rev.*, vol. 115, pp. 130–137, 1959.

[28] P. Campbell, I. D. Moore, and M. R. Pearson *Prog. Part. Nucl. Phys.*, vol. 86, pp. 127–180, 2016.

[29] C. F. Fischer *et al. Comput. Phys. Commun.*, vol. 74, pp. 415–431, 1993.

[30] B. Cheal, T. E. Cocolios, and S. Fritzche *Phys. Rev. A*, vol. 86, p. 024501, 2012.

[31] S. Fritzsche *J. Electron. Spectrosc. Relat. Phenom.*, vol. 114–116, pp. 1155–1164, 2001.

[32] H. D. Vries, C. W. D. Jager, and C. D. Vries *At. Data. Nucl. Data Tables*, vol. 36, pp. 495–536, 1987.

[33] S. Kopecky *et al. Phys. Rev. Lett.*, vol. 74, pp. 2427–2430, 1995.

[34] R. F. Frosch *et al. Phys. Rev.*, vol. 160, pp. 874–879, 1967.

[35] C. Weizsäcker *Z. Phys.*, vol. 96, pp. 431–458, 1935.

[36] G. Royer *et al. Phys. Rev. C*, vol. 73, p. 067302, 2006.

[37] R. Woods and D. Saxon *Phys. Rev.*, vol. 95, pp. 577–578, 1954.

[38] J. Maruani, R. Lefebvre, and E. Brändas, *Advanced Topics in Theoretical Chemical Physics*. Dordrecht, Netherlands: Springer Science and Business Media, 2003.

[39] K. S. Krane, *Introductory Nuclear Physics*. Hoboken, New Jersey: John Wiley and Sons, 1988.

[40] R. Bengtsson *et al. Phys. Scr.*, vol. 39, pp. 196–220, 1989.

[41] R. Firestone *et al.*, *Table of Isotopes*. New York, New York: John Wiley and Sons, 1996.

[42] F. Iachello *Hyp. Int.*, vol. 15, pp. 11–24, 1983.

[43] L. Hollberg, "Cw dye lasers," in *Dye Lasers Principles: With Applications* (F. J. Duarte, L. W. Hillman, P. F. Liao, and P. Kelley, eds.), ch. 5, pp. 185–238, Boston, Massaschusetts: Academic Press Inc., 1990.

[44] D. J. S. Johnson, *An electrostatic ion trap for laser and nuclear spectroscopy at the IGISOL*. PhD thesis, University of Manchester, 2013.

[45] T. Eronen *et al. Phys. Rev. Lett.*, vol. 97, p. 232501, 2006.

[46] X. F. Yang *et al. Phys. Rev. Lett.*, vol. 116, p. 182502, 2016.

[47] A. Voss *et al. Phys. Rev. Lett.*, vol. 111, p. 122501, 2013.

[48] J. Äystö *et al. Nucl. Instrum. Methods Phys. Res., Sect. B*, vol. 26, pp. 394–398, 1987.

[49] J. Huikari *et al. Nucl. Instrum. Methods Phys. Res., Sect. B*, vol. 222, pp. 632–652, 2004.

[50] P. Dendooven *et al. Nucl. Instrum. Methods Phys. Res., Sect. A*, vol. 408, pp. 530–534, 1998.

[51] J. Äystö *et al. Phys. Lett. B*, vol. 138, pp. 369–372, 1984.

[52] P. Dendooven *Nucl. Instrum. Methods Phys. Res., Sect. B*, vol. 126, pp. 182–189, 1997.

[53] P. Karvonen *et al. Nucl. Instrum. Methods Phys. Res., Sect. B*, vol. 266, pp. 4794–4807, 2008.

[54] *Faraday cup for low-energy, low-intensity beam measurements at the USR*, 2010 Beam Instrumentation Workshop, (Geneva, Switzerland), Joint Accelerator Conferences Website, 2010.

[55] J. Äystö *et al.*, *Three decades of research using IGISOL technique at the University of Jyväskylä*. Cham, Switzerland: Springer International Publishing, 2014.

[56] J. L. Wiza *Nucl. Instrum. Methods*, vol. 162, pp. 587–601, 1979.

[57] S. Leoni, "Microchannel plates." University lecture notes.

[58] A. Nieminen, *Manipulation of low-energy radioactive ion beams with an RFQ cooler: Application to laser spectroscopy*. PhD thesis, University of Jyvaskyla, 2002.

[59] K. Baczynska *et al. J. Phys. G: Nucl. Part. Phys.*, vol. 37, pp. 1–11, 2010.

[60] B. Cheal *et al. Phys. Rev. Lett.*, vol. 102, p. 222501, 2009.

[61] C. Babcock *et al. Phys. Lett. B*, vol. 760, pp. 387–392, 2016.

[62] M. L. Bissell *et al. Phys. Lett. B*, vol. 645, pp. 330–334, 2007.

[63] N. Boos *et al. Phys. Rev. Lett.*, vol. 72, pp. 2689–2692, 1994.

[64] R. F. Casten, *Nuclear Structure from a Simple Perspective.* Oxford, United Kingdom: Oxford University Press, 1990.

[65] A. Bohr, B. R. Mottelson, and D. Pines *Phys. Rev.*, vol. 110, pp. 936–938, 1958.

[66] C. Qi and R. Wyss *Phys. Scr.*, vol. 91, pp. 1–18, 2015.

[67] A. B. Garnsworthy *Phys. Lett. B*, vol. 660, pp. 326–330, 2008.

[68] A. Obertelli *et al. Phys. Rev. C*, vol. 80, p. 031304, 2009.

[69] M. L. Bissell *et al. Phys. Rev. Lett.*, vol. 113, p. 052502, 2014.

[70] F. C. Charlwood *et al. Phys. Lett. B*, vol. 690, pp. 346–351, 2010.

[71] S. Geldhof, "Development of a saturated absorption spectroscopy setup at igisol," Master's thesis, KU Leuven, 2015.

[72] V. T. Koslowsky *et al. Nucl. Instrum. Methods Phys. Res., Sect. A*, vol. 401, pp. 289–298, 1997.

[73] B. Singh and J. A. Cameron *Nucl. Data Sheets*, vol. 92, pp. 1–146, 2001.

[74] I. P. Johnstone and B. Castel *Phys. Lett.*, vol. 37B, pp. 329–330, 1971.

[75] C. Scholl *et al. Phys. Rev. C*, vol. 75, p. 064321, 2007.

[76] C. J. Chiara *et al. Phys. Rev. C*, vol. 75, p. 054305, 2007.

[77] T. Eronen *et al. Phys. Rev. Lett.*, vol. 103, p. 252501, 2009.

[78] M. Avgoulea *et al. J. Phys. G: Nucl. Part. Phys.*, vol. 38, pp. 1–17, 2011.

[79] N. J. Stone, *Table of Nuclear Magnetic Dipole and Electric Quadrupole Moments.* Vienna, Austria: International Atomic Energy Agency, 2011.

[80] C. Nazé *et al. Comput. Phys. Commun.*, vol. 184, pp. 2187–2196, 2013.

[81] R. Beerwerth and S. Fritzsche. Private communication, 2016.

[82] E. Caurier *et al. Rev. Mod. Phys.*, vol. 77, pp. 427–488, 2005.

[83] R. R. Whitehead *et al. Adv. Nucl. Phys.*, vol. 9, pp. 123–176, 1977.

[84] A. Poves *et al. Eur. Phys. J. A*, vol. 20, pp. 119–122, 2004.

[85] M. W. Kirson *Nucl. Phys. A*, vol. 781, pp. 350–362, 2006.

[86] E. Caurier *et al. Phys. Lett. B*, vol. 522, pp. 240–244, 2001.

[87] F. Nowacki. Private communication, 2016.

[88] S. Malbrunot-Ettanauer, H. Heylen, *et al.*, "*CERN-INTC-P-464: Laser spectroscopic studies along the Al isotopic chain and the isomer-shift of the self-conjugate nucleus* ^{26}*Al.*" Research proposal, 2016.

[89] E. Cheifetz *et al. Phys. Rev. Lett.*, vol. 25, pp. 38–43, 1970.

[90] D. A. Arseniev, A. Sobiczewski, and V. Soloviev *Nucl. Phys. A*, vol. 139, pp. 269–276, 1969.

[91] S. K. Khosa, P. N. Tripathi, and S. K. Sharma *Phys. Lett. B*, vol. 119, pp. 257–262, 1982.

[92] C. Thibault *et al. Phys. Rev. C*, vol. 23, pp. 2720–2729, 1981.

[93] F. Buchinger *et al. Phys. Rev. C*, vol. 41, pp. 2883–2897, 1990.

[94] H. L. Thayer *et al. J. Phys. G: Nucl. Part. Phys.*, vol. 29, pp. 2247–2262, 2003.

[95] F. C. Charlwood *et al. Phys. Lett. B*, vol. 674, pp. 23–27, 2009.

[96] E. Biemont *et al. Oxford J. Math. Sci.*, vol. 414, pp. 3350–3359, 2011.

[97] S. Fritzche. Private communication, 2014.